



**HAL**  
open science

# Development of wireless energy harvesters based on magnetoelectric transducers for biomedical applications

Ali Koteiche

► **To cite this version:**

Ali Koteiche. Development of wireless energy harvesters based on magnetoelectric transducers for biomedical applications. Electromagnetism. Sorbonne Université, 2022. English. NNT : 2022SORUS036 . tel-03640429

**HAL Id: tel-03640429**

**<https://theses.hal.science/tel-03640429>**

Submitted on 13 Apr 2022

**HAL** is a multi-disciplinary open access archive for the deposit and dissemination of scientific research documents, whether they are published or not. The documents may come from teaching and research institutions in France or abroad, or from public or private research centers.

L'archive ouverte pluridisciplinaire **HAL**, est destinée au dépôt et à la diffusion de documents scientifiques de niveau recherche, publiés ou non, émanant des établissements d'enseignement et de recherche français ou étrangers, des laboratoires publics ou privés.

# Thèse de doctorat de Sorbonne Université

Ecole doctorale n°130

Ecole Doctorale Informatique, Télécommunications et Electronique (EDITE)

Spécialité de doctorat: Electronique

Préparée à:

1) Institut Supérieur d'Electronique de Paris, Laboratoire d'Informatique, Signal et Image, Électronique et Télécommunications (LISITE), 28, rue Notre-Dame-des-Champs, 75006 Paris

2) Sorbonne Université, CNRS, Laboratoire de Génie Electrique et Electronique de Paris (GEEPS), Paris 75252, France

par

**Ali KOTEICHE**

## Développement de récupérateurs d'énergie sans fil à base de transducteurs magnétoélectriques pour des applications biomédicales

Thèse soutenue le 15 Mars 2022

Composition du Jury:

**Rapporteurs :**

Mickaël Lallart, PU, INSA de Lyon - LGEF,  
Hélène Debeda, MCF HDR, Université de Bordeaux - IMS

**Examineurs :**

Adrien Badel, PU, Université Savoie Mont Blanc - SYMME  
Guylaine Poulin-Vittrant, directrice de recherche, Université de Tours - CNRS-GREMAN  
Dimitri Galayko, MCF HDR, Sorbonne Université - LIP6  
Elie Lefeuvre, PU, Université Paris-Saclay - C2N

**Encadrants :**

Gérard Sou, MCF HDR, Sorbonne Université - GeePS, directeur de thèse  
Alexis Brenes, MCF, Université Paris-Saclay - C2N, co-encadrant



# Contents

<b>Résumé en français</b>	<b>7</b>
<b>Acknowledgments</b>	<b>17</b>
<b>Abbreviation</b>	<b>19</b>
<b>I Wireless power transmission: a review</b>	<b>21</b>
1 Introduction . . . . .	21
2 Evaluation criteria for wireless power transmission . . . . .	22
3 Wireless power transmission techniques . . . . .	26
3.1 Electromagnetic field sources . . . . .	26
3.1.1 Inductive power transfer . . . . .	27
3.1.2 Capacitive power transfer . . . . .	32
3.2 Light sources . . . . .	36
3.3 Acoustic sources . . . . .	38
3.3.1 Piezoelectric material . . . . .	38
3.3.2 Acoustic power transfer based on piezoelectric transducer . . . . .	42
3.4 Comparison between the WPT techniques . . . . .	45
4 Study case: wireless charging of implants . . . . .	47
4.1 Implantable medical devices . . . . .	47
4.2 Magnetolectric transducers for wireless charging . . . . .	49
5 Conclusion . . . . .	54
<b>II Characterization of magnetolectric transducers</b>	<b>55</b>

1	Introduction . . . . .	55
2	Overview on magnetoelectric transducer modeling . . . . .	55
3	Experimental setup . . . . .	58
3.1	Magnetoelectric transducer samples . . . . .	59
3.2	Characterization procedures . . . . .	61
3.2.1	Introduction . . . . .	61
3.2.2	Characterization in the absence of AC magnetic fields	61
3.2.2.i	Introduction . . . . .	61
3.2.2.ii	System-level model . . . . .	61
3.2.2.iii	Admittance measurements . . . . .	62
3.2.2.iv	Parameter identification . . . . .	63
3.2.2.v	Results and Discussion . . . . .	65
3.2.2.vi	Conclusion . . . . .	65
3.2.3	Characterization in the presence of AC magnetic fields	67
3.2.3.i	Introduction . . . . .	67
3.2.3.ii	Characterization setup . . . . .	67
3.2.3.iii	First assumption: predominant magnetic losses	67
a	Introduction . . . . .	67
b	The magnetoelectric transducer model	69
c	Measurement acquisition . . . . .	70
d	Experimental results . . . . .	72
e	Discussion and observations . . . . .	73
f	Conclusion: failure of the first assumption . . . . .	75
3.2.3.iv	Second assumption: predominant mechanical losses . . . . .	76
a	Introduction . . . . .	76
b	Characterization setup . . . . .	76
c	Presumption based on admittance measurements . . . . .	77

	d	Linear model with variable parameters	77
	e	Experimental results . . . . .	80
	f	Further analysis and validation . . .	81
	g	Discussion about the physical origin of power losses . . . . .	87
4		Conclusion . . . . .	88
<b>III Power management of magnetoelectric transducer</b>			<b>91</b>
1		Introduction . . . . .	91
2		Output power of magnetoelectric transducer . . . . .	94
	2.1	Power limit of the magnetoelectric transducer . . . . .	94
		2.1.1 Definition of the power limit . . . . .	94
		2.1.2 Conditions to reach the power limit . . . . .	94
		2.1.3 Figure-of-merit of the magnetoelectric transducer . .	96
		2.1.4 The power limit formula . . . . .	96
		2.1.5 Impact of parameter variations on circuit design . . .	98
	2.2	Power management circuits for magnetoelectric transducer . .	98
		2.2.1 Introduction . . . . .	98
		2.2.2 Power terms in the system . . . . .	100
		2.2.3 Selection criteria of the power management circuits .	101
		2.2.4 Power management circuit simulation . . . . .	103
		2.2.4.i Standard energy harvesting circuit . . . . .	104
		a State-of-the-art : Description of the SEH circuit topology and impedance matching condition . . . . .	104
		b Implementation proposed for the SEH circuit . . . . .	105
		2.2.4.ii Unipolar synchronized electric charge extrac- tion circuit . . . . .	107

a	State-of-the-art : Description of the USECE circuit topology and impedance matching condition . . . . .	107
b	USECE implementation with RS latch	109
2.2.4.iii	LTSpice Simulation . . . . .	109
a	Operating points of the simulations .	109
b	Extracted power with respect to the power limit . . . . .	112
c	Efficiency of the circuit . . . . .	112
d	Autonomous circuit for implants . . .	114
2.2.4.iv	Conclusion . . . . .	118
3	Conclusion . . . . .	120
<b>Appendices</b>		<b>127</b>
<b>List of Figures</b>		<b>134</b>
<b>List of Tables</b>		<b>141</b>
<b>Bibliography</b>		<b>142</b>

## Abstract

E-Health and the Internet of Things (IoT) are two growing markets, related to each other by the interconnection of nomadic objects for the “quantified self”, where each patient can perform his own physiological tests. To that purpose, one of the technological challenges lies in the power autonomy, since energy must be supplied to the system with a minimum interaction from the outside (the device can for instance be directly implanted inside the body of the patient and thus unreachable). Hence, the development of a wireless energy harvester has a very wide range of applications. In this context, magnetoelectric (ME) materials arouse a significant scientific interest as energy transducers to transform electromagnetic energy provided from the outside into electrical energy available to power the system. ME materials are laminar composites based on piezoelectric and magnetostrictive layers, generally glued together. The device is usually connected to an electrical interface via deposited electrodes. When the ME material is driven by an external magnetic field, magnetostrictive elements are subject to mechanical constraints and motion. This motion is then transferred to the piezoelectric element which generates a voltage between its electrodes. Then, the energy must be shaped (conditioned) and managed at the system level (power management). For piezoelectric energy harvesters, many optimization strategies already exist to maximize the power flow from the transducer to the energy storage unit. This optimization takes into account the impact of the energy harvesting circuit on the overall performances of the system. Yet, to this day, no optimal solution has been identified to fit the specific constraints imposed by magnetoelectric resonators. Taking into account the specificity of magnetoelectric resonators at the system level will be a key point of this thesis. The thesis will thus aim at studying and designing the architecture of energy harvesting and conditioning systems for magnetoelectric transducers.

# Résumé en français

Le chargement sans fil de dispositifs électroniques est une technologie de plus en plus présente dans notre vie quotidienne, en particulier grâce au confort qu'elle apporte aux utilisateurs (par exemple pour la recharge de véhicules électriques en l'absence de câblages classique ou celui des smartphones). Pour les dispositifs médicaux implantables, cette technologie peut aussi sauver des vies, comme dans le cas des pacemakers qui sont des dispositifs conçus pour détecter et régler l'anomalie du rythme cardiaque. Ce type d'implant peut être implanté dans le corps humain après une opération à coeur ouvert potentiellement dangereuse pour la vie des patients. Une fois installé dans le corps, ce dispositif doit fonctionner en toute autonomie pendant des années, généralement grâce à une batterie. Après quelques années (10 à 20 ans), cette batterie doit être chargée de nouveau (et/ou remplacée). Si l'on pouvait recharger cette batterie sans fil (dans les cas les plus courants où elle est encore fonctionnelle), il serait possible d'éviter une deuxième opération chirurgicale.

Dans la littérature, on trouve principalement deux catégories de dispositifs à chargement sans fil : les systèmes à récupération d'énergie sans fil, et ceux à transfert d'énergie sans fil. Ces termes désignent deux approches différentes. La première approche consiste à récupérer l'énergie ambiante (pouvant provenir de l'environnement du corps humain ou du corps humain lui-même). Cette énergie peut être sous forme thermique (différence de température entre le corps et l'extérieur par exemple), sous forme mécanique (battements du coeur) ou aussi sous forme électromagnétique (stations radio AM/FM, stations cellulaires et stations de diffusion visuelle, émetteurs divers...).

L'autre approche consiste à envoyer de l'énergie aux implants à l'aide d'une source extérieure. L'exemple le plus connu de cette approche est le transfert d'énergie par couplage inductif. Cette technique utilise le phénomène d'induction entre plusieurs bobines afin de convertir l'énergie électromagnétique en une énergie électrique qui peut alimenter les batteries des implants. Mais on trouve aussi dans la littérature une autre technique de transfert d'énergie à partir de sources ultrasons. Dans ce cas l'énergie est envoyée sous forme acoustique. Le récepteur est fabriqué en général de matériaux piézoélectriques capables de transformer l'énergie acoustique en une énergie électrique. On peut trouver aussi que d'autres méthodes comme celles qui fonctionnent sur le principe du couplage capacitif ou sur le transfert de l'énergie en utilisant des cellules photovoltaïques ont été développées pour des applications dans le domaine biomédical.

Cette thèse étudie une autre méthode innovante de transfert d'énergie sans fil à partir de transducteurs magnétoélectriques (ME). Il s'agit d'une solution hybride mêlant plusieurs principes de conversion présentés précédemment. Les transducteurs ME peuvent soit être fabriqués à partir de matériaux intrinsèquement magnétoélectriques (transforment l'énergie magnétique en une énergie électrique et inversement) soit fabriqués par collage de couches de matériaux piézoélectriques et magnétostrictifs ensemble. Dans ce cas le transfert d'énergie se fait en deux étapes : d'abord, la partie magnétostrictive du transducteur reçoit l'énergie magnétique et la transforme en une déformation mécanique. Ensuite, puisque les deux parties magnétostrictive et piézoélectrique sont solidaires, la partie piézoélectrique est entraînée dans le mouvement et convertit ces vibrations en une énergie électrique utile pour l'alimentation de l'électronique d'un implant ou pour charger sa batterie. Cette thèse se concentre sur la seconde catégorie (comme les échantillons de la Fig. -1) même si un certain nombre de résultats sont applicables également à la première.

Le premier objectif de la thèse est de trouver un modèle "système" permettant de

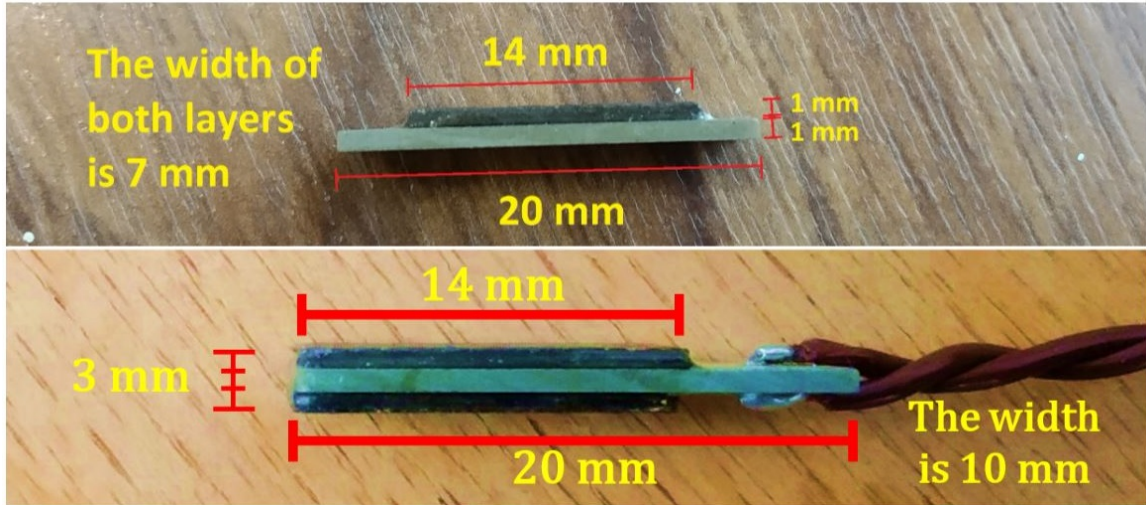


Figure -1: Deux échantillons de transducteurs magnétoélectriques étudiés dans cette thèse (Vert clair : partie piézoélectrique - foncé: partie magnétostrictive)

caractériser les transducteurs magnétoélectriques et de prédire leur comportement de façon fiable en dehors des conditions exactes de caractérisation. Une des principales difficultés réside dans le fait que les modèles de la littérature sont des modèles au niveau "matériau". Pour cette raison, un nouveau modèle a été développé, inspiré d'un modèle classique utilisé pour les transducteurs piézoélectriques Fig. -2.

Le modèle classique des transducteurs piézoélectriques est constitué d'une masse effective  $M$  suspendue à un ressort de raideur  $K$ . Le couplage entre les domaines électrique et mécanique est représenté par le coefficient de couplage  $\alpha$  et les pertes mécaniques sont représentées par l'amortisseur  $c$ . Les autres paramètres du modèle sont la capacité de l'élément piézoélectrique  $C_p$  et la fréquence de résonance en court-circuit  $f_0$ . Dans le but d'arriver à un nouveau modèle des transducteurs ME, plusieurs hypothèses sur les comportements de ces transducteurs ont été posées. Ces hypothèses concernent principalement les origines des pertes dans le système et sur la (non-)linéarité des paramètres du modèle proposé. Pour vérifier ces hypothèses, un grand nombre de séries expérimentales de mesures ont été réalisées d'abord en absence de champ magnétique variable, puis en présence de champ magnétique variable. Dans le premier cas, des mesures d'impédance ont été réalisées avec un analyseur d'impédance à différents niveaux d'actionnement (niveaux de tension) et ces mesures

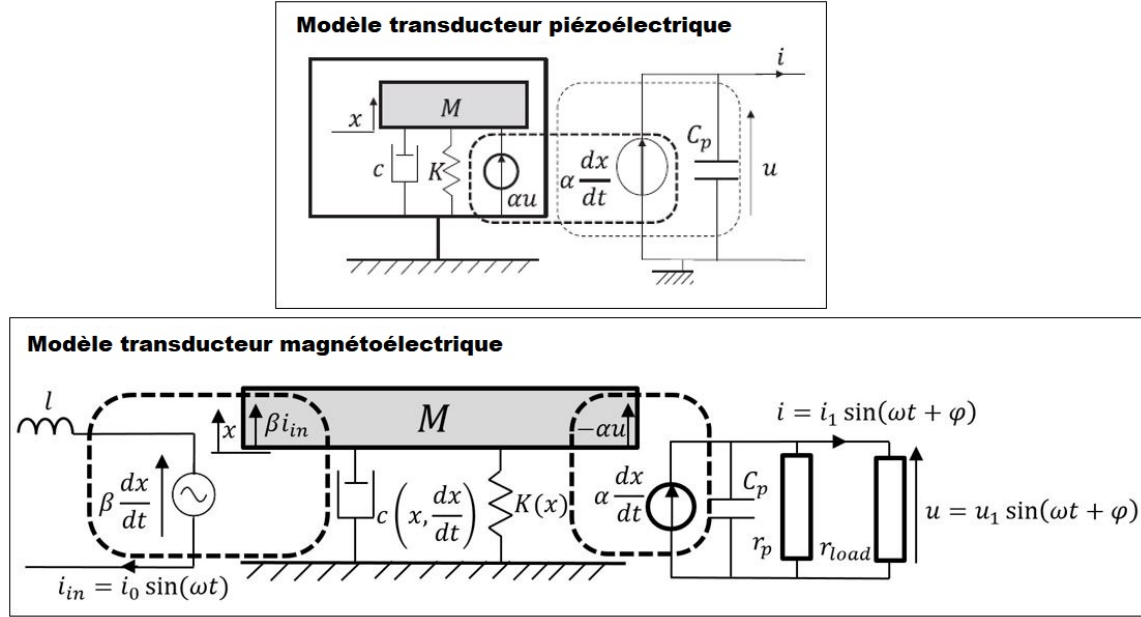


Figure -2: Modèles du niveau "système" (haut: transducteur piézoélectrique , bas: transducteur magnétoélectrique)

ont montré une dépendance de l'impédance du transducteur vis-à-vis des niveaux de tensions, phénomène qui n'apparaissait pas en l'absence de la couche magnétostrictive. Ces résultats préliminaires ont montré que le collage de la partie magnétostrictive à l'élément piézoélectrique a un impact sur la réponse du transducteur. Cette observation a été validée lors de la caractérisation du transducteur ME qui a permis d'identifier les paramètres du système normalisé du modèle: le facteur de qualité  $Q$ , le coefficient de couplage  $k_m^2$  la capacité  $C_p$  et la fréquence de résonance  $f_0$  (Fig. -3).

Après cette première caractérisation, l'identification d'un modèle plus évolué du transducteur ME a été faite en présence de champ magnétique variable grâce à un banc de test construit pendant la thèse, constitué d'une bobine émettrice, d'un support pour les échantillons ME, d'aimants montés sur une glissière, d'un oscilloscope et d'un générateur de fréquence. Pour un transducteur ME, la polarisation de sa partie magnétostrictive permet d'augmenter la puissance récupérée. Cette polarisation se fait en appliquant un champ magnétique statique dans une direction adaptée à l'échantillon à caractériser. Cela a été réalisé grâce à l'ajustement des aimants

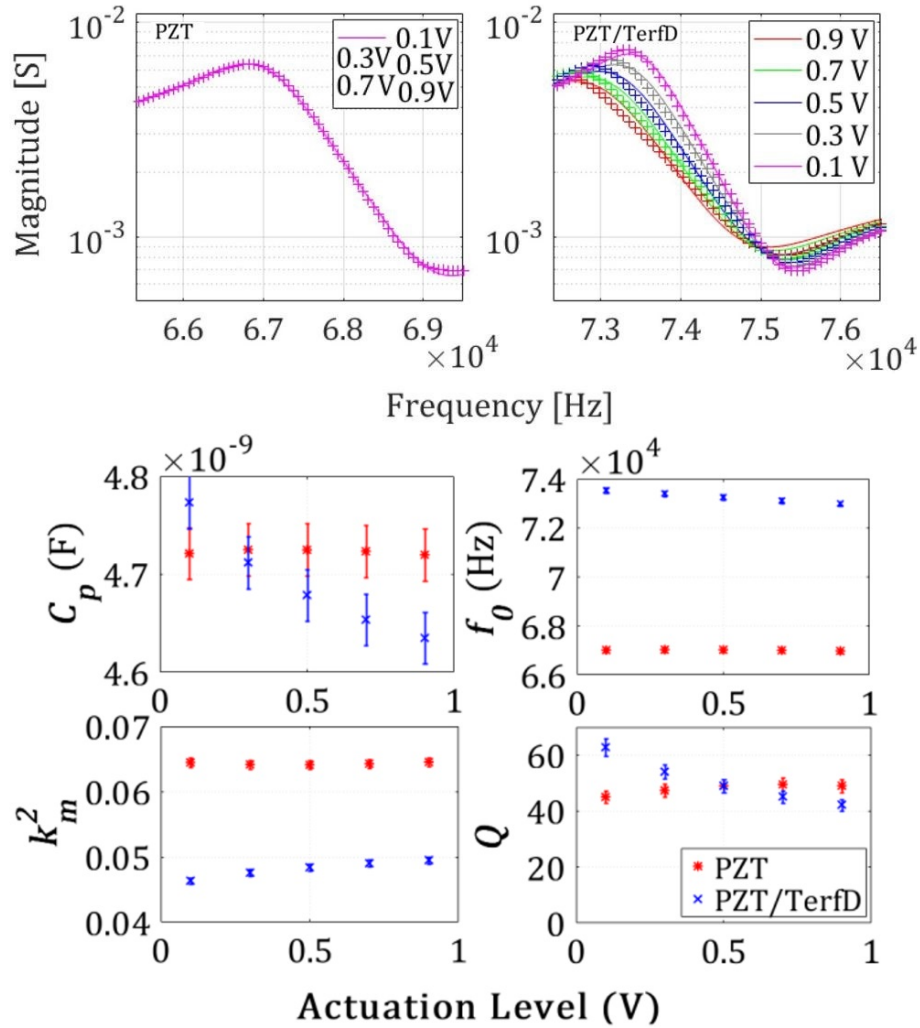


Figure -3: Caractérisation en absence du champ magnétique. Haut: mesures d'impédance de l'élément piézoélectrique (PZT) et du transducteur ME (PZT/TerfD). Bas: résultat de l'identification des paramètres de l'élément piézoélectrique et du transducteur ME en utilisant le modèle classique)

sur la glissière, permettant de trouver la position optimale qui maximisera ensuite la puissance transférée. Le champ dynamique a été assuré par la bobine alimentée par le générateur de fréquence. Le contrôle de la fréquence et du niveau de tension du générateur de fréquence ainsi que l'acquisition des tensions mesurées par l'oscilloscope ont été automatisés par ordinateur. La Fig. -4 montre une photo du banc de test et un exemple de série de mesures automatisées. Ces mesures sont faites sur un intervalle de fréquence qui inclut la résonance du système. Une carte de résistance contrôlée par l'ordinateur a été utilisée pour tester le comportement du système sur différentes charges résistives.

Sur la base des variations de paramètres observées dans la caractérisation en absence du champ magnétique variable, des hypothèses ont été posées sur l'origine des pertes dans le système (transducteur, bobine émettrice et charge connectée au transducteur). La première hypothèse considère que les origines des pertes sont magnétiques (courants de Foucault dans la partie magnétostrictive du transducteur). Pour vérifier cette hypothèse, des mesures à champs magnétique contrôlé ont été réalisées en contrôlant les courants d'entrée dans la bobine sur tout l'intervalle de fréquence. Ces tests à différents niveaux de courant n'ont pas abouti à des résultats cohérents, le modèle résultant donnant des valeurs de paramètres aberrantes dès lors que le modèle était légèrement extrapolé au-delà de son domaine de caractérisation.

La deuxième hypothèse considère que les pertes sont plutôt mécaniques dues à la colle entre la partie magnétostrictive et la partie piézoélectrique du transducteur. Pour vérifier cette hypothèse, la caractérisation du transducteur a été faite à des amplitudes d'oscillation mécanique contrôlées par l'intermédiaire de la régulation de l'amplitude du courant de sortie du transducteur. Dans ces conditions le problème revient à supposer que les paramètres dépendent du courant de sortie pour chaque valeur de charge résistive. Pour cela, des mesures à courant de sortie régulé dans différentes conditions ont été réalisées. Ces mesures ont permis d'identifier les paramètres du nouveau modèle pour chaque niveau de courant et pour chaque résistance. Enfin les lois de comportements des paramètres ont été validées sur des mesures à courant

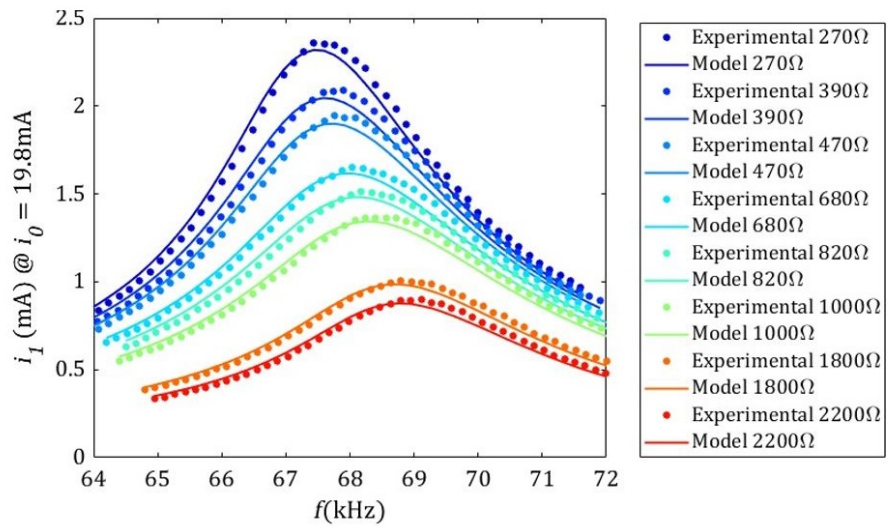
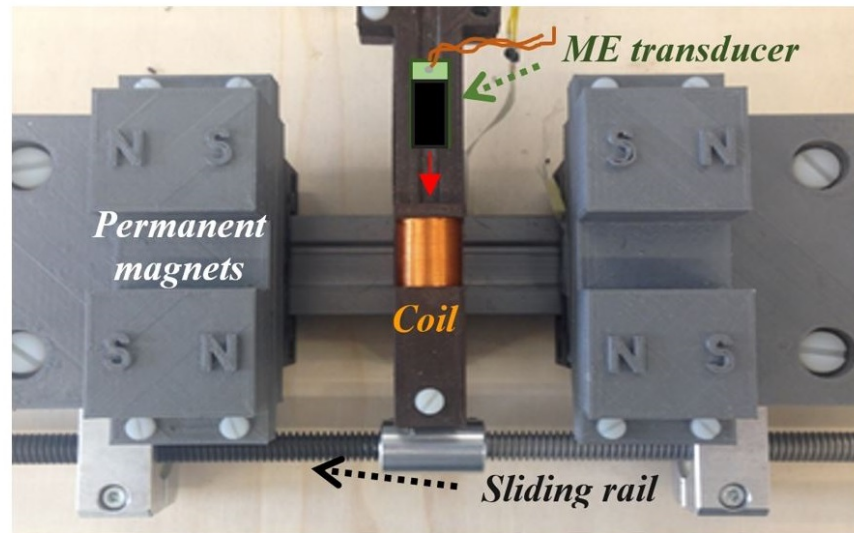


Figure -4: Caractérisation en présence du champs magnétique (haut: banc expérimentale , bas: courbe de la fonctionde transfert à un niveau d'actionnement fixe avec plusieurs résistances

d'entrée contrôlé (et où donc le courant de sortie n'était plus régulé). Cette caractérisation a montré des résultats cohérents bien au-delà de son domaine de mesure.

A partir du modèle ainsi identifié, la deuxième étape a consisté à trouver une stratégie de maximisation de la puissance récupérée par le transducteur ME en présence de champ magnétique variable. Pour cette étude, un modèle électrique équivalent au modèle électro-magnéto-mécanique basé sur le modèle proposé dans la première partie de cette thèse a été introduit. Ce modèle est constitué d'une bobine  $L_{mech}$  de valeur  $M/\alpha^2$  qui représente l'inertie du transducteur, une résistance  $R_{mech}$  de valeur  $c/\alpha^2$  qui représente l'amortissement, une capacité  $C_{mech}$  de valeur  $\alpha^2/K$  (Fig. -5).

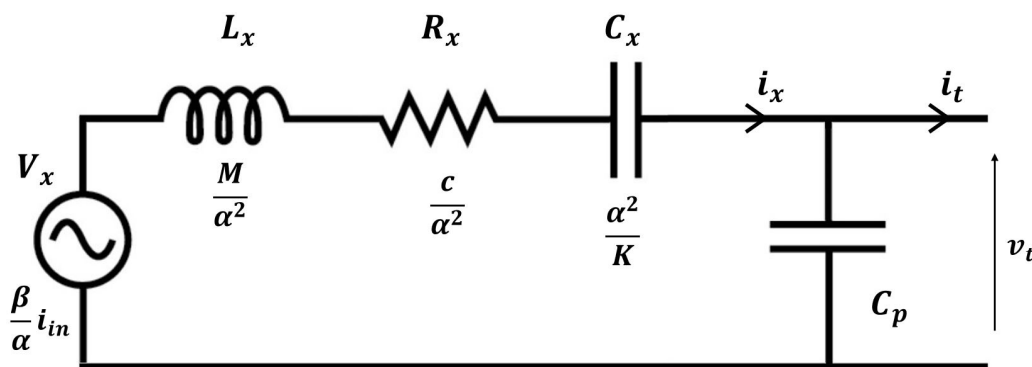


Figure -5: Circuit électrique équivalent du transducteur magnétoélectrique

Afin de trouver le point de fonctionnement optimal du transducteur, une étude théorique fondée sur des considérations d'adaptation d'impédance et sur la méthode du premier harmonique a mis au jour les conditions d'optimalité par analogie avec les transducteurs PE. L'étude montre que le produit  $k_m^2 Q$  utilisé pour optimiser les transducteurs piézoélectriques peut être utilisé pour les transducteurs ME dans la mesure où le facteur de qualité  $Q$  prend en compte l'ensemble des pertes énergétiques dans le système (quelle que soit leur origine). De plus, la littérature fait état d'une expression théorique de la puissance maximale récupérable par un transducteur PE appelée "puissance limite"  $P_{limPE}$ . Par analogie, la puissance limite des systèmes de

transfert d'énergie à base de transducteurs ME  $P_{lim_{ME}}$  a été déterminée. Les mesures de puissance ont validé expérimentalement ce calcul théorique.

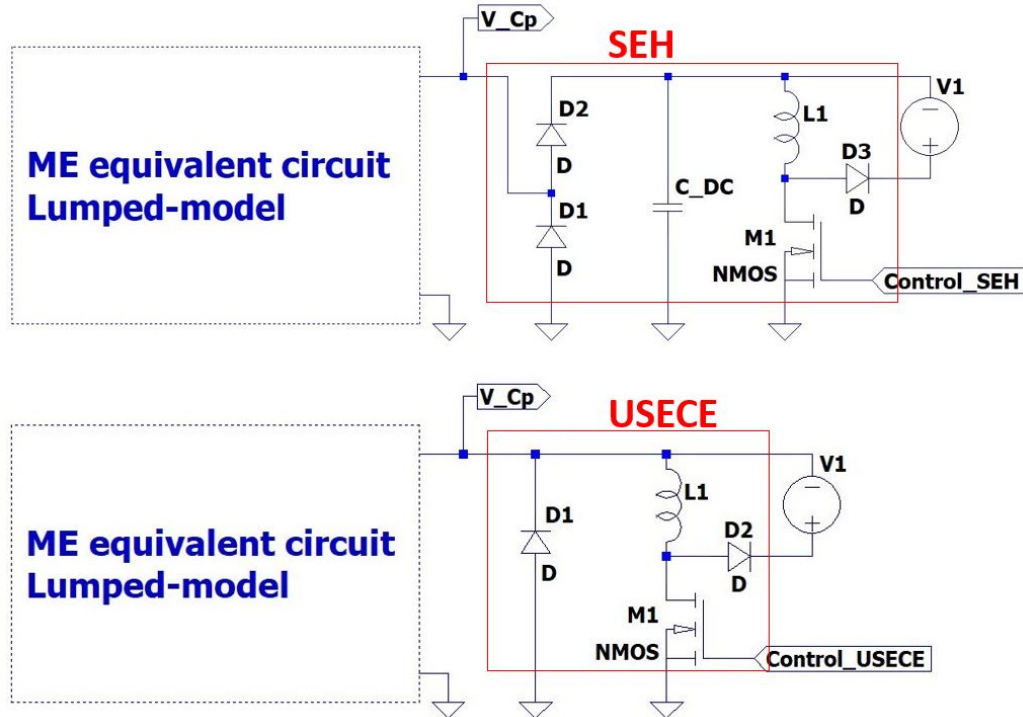


Figure -6: Haut: schéma du circuit SEH, bas: schéma du circuit USECE

Pour atteindre la puissance limite des transducteurs, des circuits de gestion de puissance doivent être utilisés entre la charge et le transducteur. Ces circuits permettent une adaptation d'impédance dans le système (entre transducteur et élément de stockage d'énergie). Le choix du circuit de gestion est un compromis entre maximisation de la puissance récupérée et minimisation de pertes dans les composants. Ce choix est lié à la fois à la puissance qu'on souhaite récupérer ou transférer et aux paramètres des transducteurs utilisés. En se basant sur la ressemblance entre les deux modèles électriques des deux transducteurs PE et ME, des circuits de gestion de puissance PE ont été testés en simulation sur les transducteurs ME.

Deux circuits ont été simulés : le circuit standard SEH (Standard Energy Harvester) constitué d'un étage de redressement, d'une capacité de lissage et d'un convertisseur DC-DC et le circuit USECE (Unipolar Synchronous Electric Charge Extrac-

tion), constitué uniquement d'un redresseur simple alternance et d'un étage d'extraction charge synchrone (Fig. -6). Le choix du premier circuit, bien que complexe à implémenter à ces fréquences de fonctionnement, est assez naturel dans la mesure où il s'agit du circuit le plus représenté et étudié dans la littérature. Le choix du circuit USECE, en alternative au SEH, a été fait sur base de la figure de mérite déterminée dans l'étape de caractérisation. Pour la figure de mérite obtenue, la théorie annonce que la puissance récupérée avec un circuit de type USECE devrait être significativement supérieure à celle récupérée par le SEH. Les résultats de simulation ont montré que, même en présence des non-linéarités du modèle, le circuit USECE parvient à récupérer entre 92% et 98% de la puissance limite récupérable tandis que ce rapport est un peu plus bas avec le circuit SEH soit entre 79% et 90% pour les mêmes niveaux d'actionnement. Du fait des non-linéarités du transducteur, cet écart tend à augmenter à des niveaux de champ magnétique (et donc de puissance émise par la bobine émettrice) plus élevés.

# Acknowledgments

I would like to express my sincere gratitude to everyone supported me to realize this report. I would like to offer my special thanks to the GEEPS laboratory members especially to my thesis director Gerard Sou and the lab members Hakeim Talleb, Chloé Hamel and Aurélie Gensbittel. I would thank the staff at C2N and LIP6 for their warm welcome and to all the jury members. I am deeply grateful to my supervisor Alexis Brenes for his assistance at every stage of this thesis and to Kevin Malleron for his support and his contribution in the experimental part. I would like to extend my sincere thanks to the ISEP teachers and staff, to my friends and my family to their steady support and advice throughout the three past years.



# Abbreviation

- SDOF - Single Degree Of Freedom
- ME - Magnetoelectric
- PE - Piezoelectric
- MS - Magnetostrictive
- SEH - Standard Energy Harvester
- USECE - Unipolar Synchronous Electric Charge Extraction
- WPT - Wireless power transfer
- IPT - Inductive power transfer
- CPT - Capacitive power transfer
- APT - Acoustic power transfer
- ICNIRP - International Commission on Non-Ionizing Radiation Protection
- IMD - Implantable medical devices
- PTE - Power transfer efficiency
- EMF - Electromagnetic field
- SAR - Specific Absorption Rate
- FoM - Figure of merit



# Chapter I

## Wireless power transmission: a review

### 1 Introduction

Wireless power transfer (WPT) techniques are used to transfer electrical energy without cable from a transmitter to a receiver to power an end-device (e.g. small sensors, actuators) which represents the load (see Fig. I-1). These WPT techniques can be classified into categories regarding the type of the source of energy. In this chapter we will cover three types of energy sources: electromagnetic, acoustic, and photovoltaic. The choice of the source depends on the application and on the regulation related to the potential dangers for the users and their environment. In this chapter, we will give an overview of several existing near and far-field techniques used for wireless power transfer (WPT). These techniques are inductive power transfer (IPT), capacitive power transfer (CPT), photovoltaic (PV) and acoustic power transfer (APT). In the first part, we will introduce some evaluation criteria of WPT techniques. Then we will present the main elements of the WPT techniques under study (IPT, CPT, PV, APT) and bring up some important milestones related to these solutions. We will also present some applications of these solutions. A comparison between the WPT solutions will be provided. This comparison is based on evaluation criteria such as the power rate, the dimension of the receiver and the operating frequency of the source.

In the second part of this chapter, we will talk about a specific application of wireless power transfer: the implantable medical devices (IMDs) [1]. We will define IMDs and give some common examples. Then we will talk about the limitation of some wireless power transfer solutions when applied to IMDs. At the end of this chapter, we will introduce the WPT solution based on magnetolectric transducers that we study in this thesis.

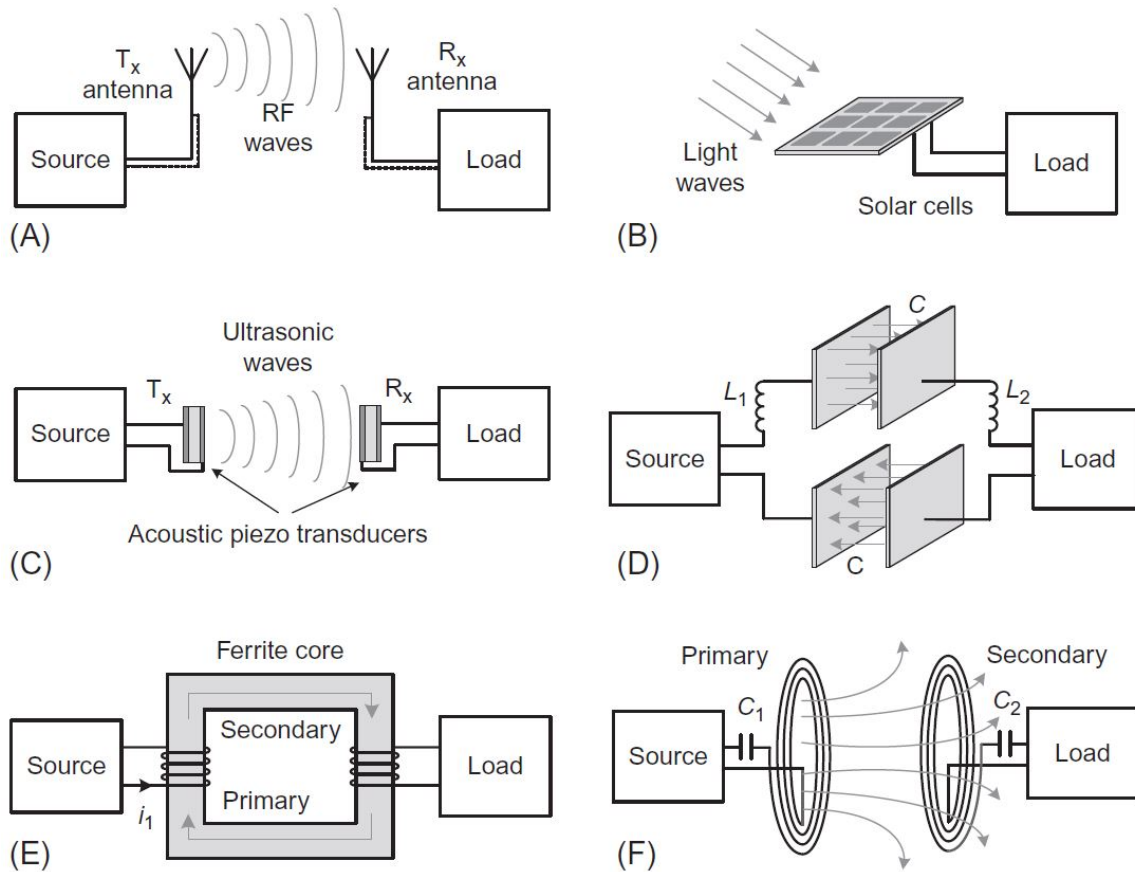


Figure I-1: Examples of wireless power transfer methods. (A) WPT with radio-frequency waves, (B) solar radiation in optical WPT, (C) WPT using ultrasonic waves, (D) capacitive power transfer, (E) tightly coupled inductive power transfer, and (F) loosely coupled resonant inductive power transfer [2]

## 2 Evaluation criteria for wireless power transmission

Before introducing the existing wireless power transfer solutions we will define important evaluation criteria for wireless power transfer (WPT) techniques that help to

make comparisons between them. Some of these criteria describe the performance of the technique and others are related to the norms and regulations of the applications. Here are examples of these two categories:

### 1. Performance criteria

- Power transfer efficiency (PTE): ratio between the output power at the receiver side and the input power at the transmitter side. This ratio quantify the amount of energy that reaches the receiver.
- Distance between the transmitter and the receiver of the WPT technique
- Power density of the receiver
- Directivity: some techniques need to adjust the position of the transmitter and receiver in order to increase the efficiency.

### 2. Regulation criteria

- Energy absorption: there is a limitation for the energy absorption of a human body when using wireless power transfer technique based on electromagnetic field (EMF). Depending on the application, different terminologies are used to describe the limitation [3]. In case of the exposure to EMFs with frequencies below  $6GHz$  the term "specific energy absorption rate" (SAR) is used. It corresponds to the power absorbed per unit mass ( $W/kg$ ). For EMFs with frequencies above  $6GHz$  we use the term "absorbed power density" ( $S_{ab}$ ) which is the density of absorbed power over area ( $W/m^2$ ). These two terms describe the rate of energy deposition (power). They are used when the exposure time is relatively high. For brief exposures there is no sufficient time for heat diffusion. Thus, the use of total energy deposition terms is more relevant than the previous terms. In this case "specific energy absorption" ( $SA$ , in  $J/kg$ ) and "absorbed energy density" ( $U_{ab}$ , in  $J/m^2$ ) are used for EMFs below and above  $6GHz$ , respectively.

- Regulation on the electromagnetic field: Wireless power transfer to charge implants may have damage on the health of the patient if some norms are not applied. For example, the exposure of a human body to a time-varying electromagnetic fields (EMF) results in internal electric fields, in body currents and energy absorption in tissues. The intensity of these fields and energy depends on the coupling mechanisms and the frequency involved. This could cause harmful and undesirable effects on the skin and the tissues (e.g. heating, damages to the nervous system). Therefore restrictions and limitations on the amplitude of the EMF fields are needed for wireless charging applications of implants based on solutions that uses EMF fields (e.g. inductive coupling, capacitive coupling). In this thesis we study a solution based on magnetoelectric transducers which also uses EMF sources to transfer the energy. The International Commission on Non-Ionizing Radiation Protection (ICNIRP) is an independent non-profit organization which aims to protect people and the environment from detrimental exposure to all forms of non-ionizing radiation (NIR). To this end, ICNIRP provides advice and guidance by developing and disseminating science-based exposure guidelines that provide a framework to limit exposure [4]. In [5] we can find guidelines for limiting exposure to time varying electric and magnetic fields for a frequency range from 1 Hz to 100 kHz and in [3] from 100 kHz to 300 GHz. These guidelines separate between two categories of exposure: occupational and general public. The occupational exposures refer to adults who are working in workplaces under known conditions. The general public refers to people of all ages which are unaware of their exposure to EMF. The guidelines on EMF from 100 kHz to 300 GHz [3] gives two types of restrictions for each category: local exposure and whole body exposure for frequencies. At these range of frequencies (100 kHz to 300 GHz) ICNIRP the limitation are time averaged over 6 min. Fig. I-2 shows graphs of the EMF amplitudes and the power density limitations. The ICNIRP guidelines defines the electric fields in-

side the body as the induced electric fields  $E_{ind}$  (V/m). These guidelines consider  $E_{ind}$  as the main component of the EMF that affects the body and specify its regulation. It is considered one of the reference level quantities easy to evaluate because it can be measured outside the body. Other important reference level quantities are the incident magnetic field  $H_{ind}$ , incident power density ( $S_{inc}$ ), planewave equivalent incident power density ( $S_{eq}$ ), incident energy density ( $U_{inc}$ ), and plane-wave equivalent incident energy density ( $U_{eq}$ ) [3].

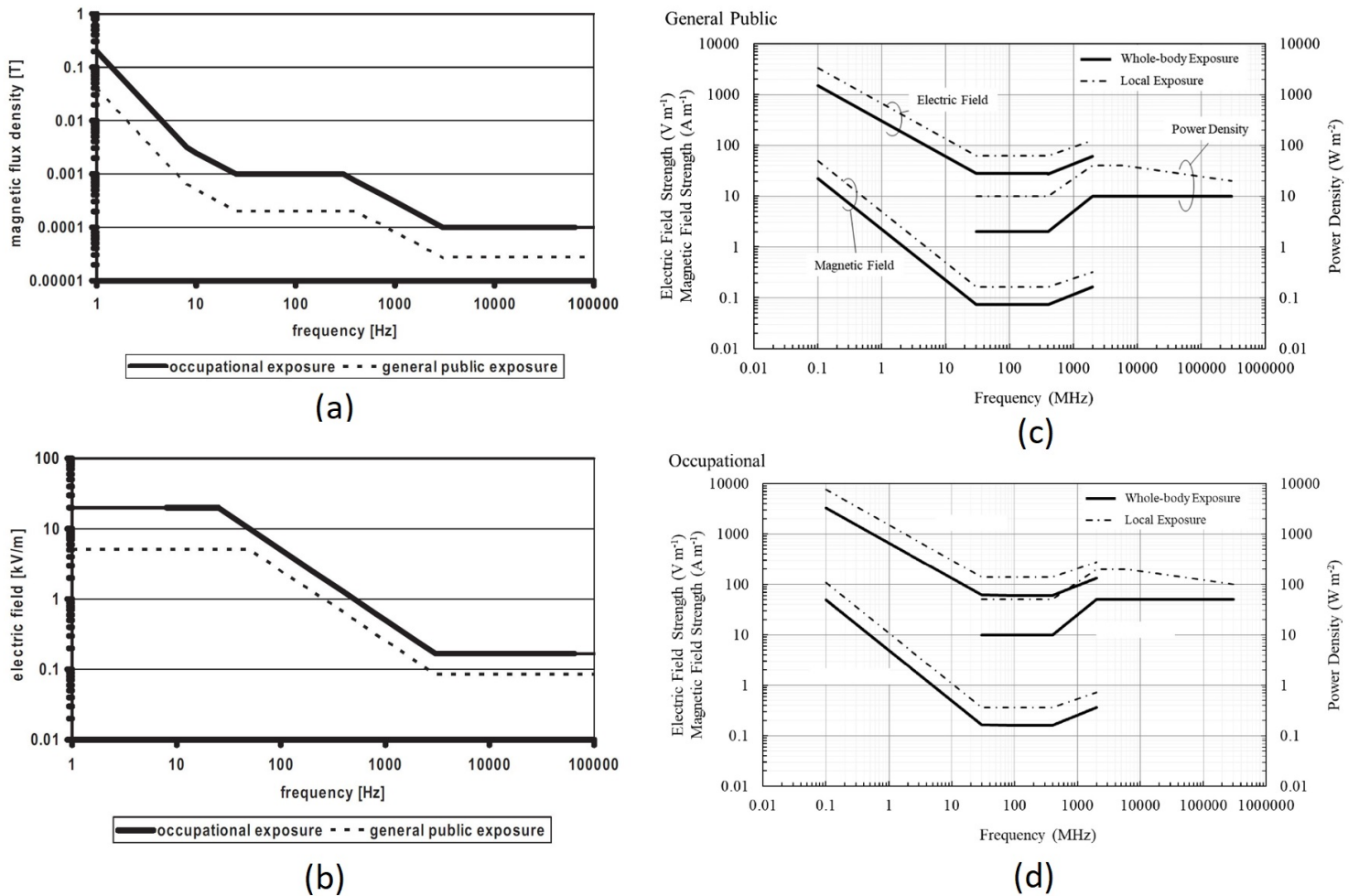


Figure I-2: Left: Reference levels for exposure to time varying (a) magnetic fields (b) electric fields from 1Hz to 100kHz [5]. Right: Reference levels for time averaged exposures of 6 min, to electromagnetic fields from 100 kHz to 300 GHz for the two categories, (c) general public (d) occupational [3]

- Regulation on the type of substance used in the technique: One of the regulation that aims to limit the use of dangerous substances in the electric and electronic equipment is the Restriction of Hazardous Substances (RoHS)
- Dimensions of the device: the volume of the solution is a critical criteria for health technology especially for implants

### 3 Wireless power transmission techniques

In this section we will introduce some health technology applications using different wireless power transfer (WPT) techniques. These applications will be classified into three categories with respect to the type of the energy source send by the emitter. These sources are the electromagnetic sources (inductive and capacitive power transfer), the acoustic sources and the light sources.

A comparison will be made based on several criteria, in particular the transferred power, the size of the receiver, the frequency of operation and/or the sensitivity to directivity. We will insist on the criteria that can be used for a fair comparison. Other information will sometimes be provided regarding the power transfer efficiency and the peak power levels. However, one should keep in mind that the two latter criteria are very hard to compare or to use as a performance indicator. The power transfer efficiency is usually measured in different ways from one work to another and the peak power is not representative of the overall performance of the system. This is why these performance indicators should be reminded with precaution.

#### 3.1 Electromagnetic field sources

An interesting property of electromagnetic waves that they can spread not only into solid material but also into air (and vaccum). This property is widely used in telecommunication applications to transfer the data wirelessly. In fact, the data transmission is a kind of power transfer for communication purposes. Wireless power transfer applications that use electromagnetic waves sources can be divided into two main parts:

inductive power transfer (IPT) and capacitive power transfer (CPT) techniques. Here we will introduce these two techniques and give some examples.

### 3.1.1 Inductive power transfer

The inductive power transfer (IPT) is a wireless power transfer solution based on inductive coupling. Many applications for IPT technology exist, e.g. in electric vehicles or industry [6], biomedical implants [7] or smartphones [8].

The induction phenomenon was discovered by Michael Faraday in 1831. Faraday's law of induction states that the changing in magnetic flux due to a current changing in a conductor induces an electromotive force in another conductor nearby. The corresponding formula of Faraday's law that describes this physical phenomenon is given in I.1. This law was generalized by James Clerk Maxwell to the Maxwell–Faraday equation I.2 which is one of the well-known Maxwell equations in the theory of electromagnetism.

$$e = -N \frac{d\Phi}{dt} (V) \tag{I.1}$$

$e$ : induced voltage,  $N$ : number of wire turns,  $\Phi$ : Magnetic flux

$$\nabla E(r, t) = \frac{\partial B(r, t)}{\partial t} \tag{I.2}$$

$\nabla$ : the curl operator,  $E$ : the electric field,  $\partial$ : the partial derivative operator,  $B$ : the magnetic field,  $r$  and  $t$  are the position and the time respectively [9, 10].

Typically the transmitter in IPT solutions is one coil or more that sends variable magnetic fields (sinusoidal in general) to a receiver (coil). The magnetic field is controlled by regulating the amplitude and the frequency of the alternative current that passes through the coils of the transmitter. The frequency range for IPT applications can go up to 10 MHz [11]. In some example the good power transmission ratio could achieve 90% or more with a gap distance between the transmitter and the receiver should be up to 30cm [12, 13, 14].

The number of coils used to transfer the power has an impact on the efficiency.

Fig. I-3 shows an example that illustrates the impact of the distance  $d$  on a 2-coil system as well as on a 4-coil system with fixed coil dimensions ( $r = 30\text{cm}$  as the coil radius and  $a = 3\text{mm}$  as the cross-sectional radius of copper wire). The example shows that the efficiency of the 2-coil systems drops dramatically at distances superior to the diameter of the coil ( $2r$ ). On the other side the 4-coil (see Fig. I-4) systems can improve the performance of transmission efficiency [15] but the order of magnitude of the working distance remains similar.

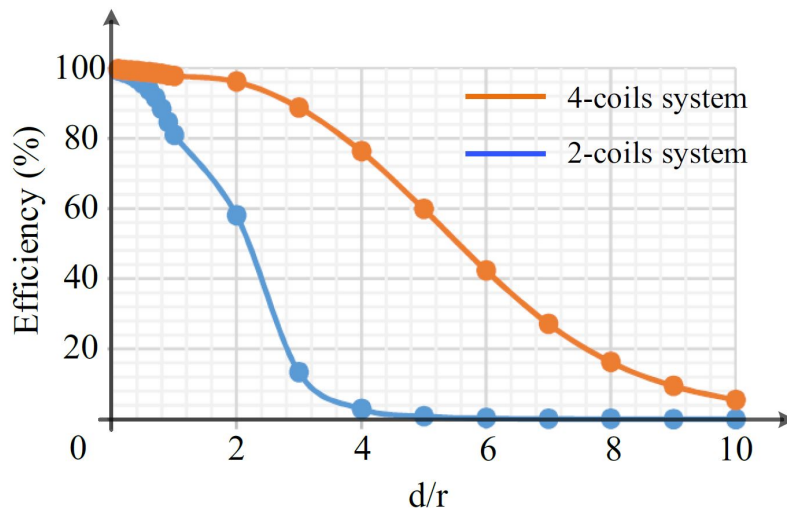


Figure I-3: Impact of the distance  $d$  on the power transmission efficiency of 2-coils (blue) and 4-coils (red) IPT systems ( $r$  is the coil radius) [16]

Moreover, the power transfer efficiency is also related to the power operating point for a given circuit. It tends to decrease when the level of transmitted power increases mainly due to heat dissipation. Therefore, to achieve higher efficiency, forced cooling of the circuit can improve the efficiency [18]. Unfortunately, this comes at the cost of more complex implementation and make the implementation impossible for implanted systems.

An example of implants that use bioresorbable coil is presented in [19]. It uses a Magnesium-based coil with a diameter of  $10\text{mm}$ . The working distance is about  $8\text{cm}$  and the operating frequency is near to  $5\text{MHz}$ . The implant generates voltages of  $100\text{--}300\text{ mV}$  at the nerve which are sufficient to induce nerve activation. The biocompatibility is an interesting property of this example which give it an advantage

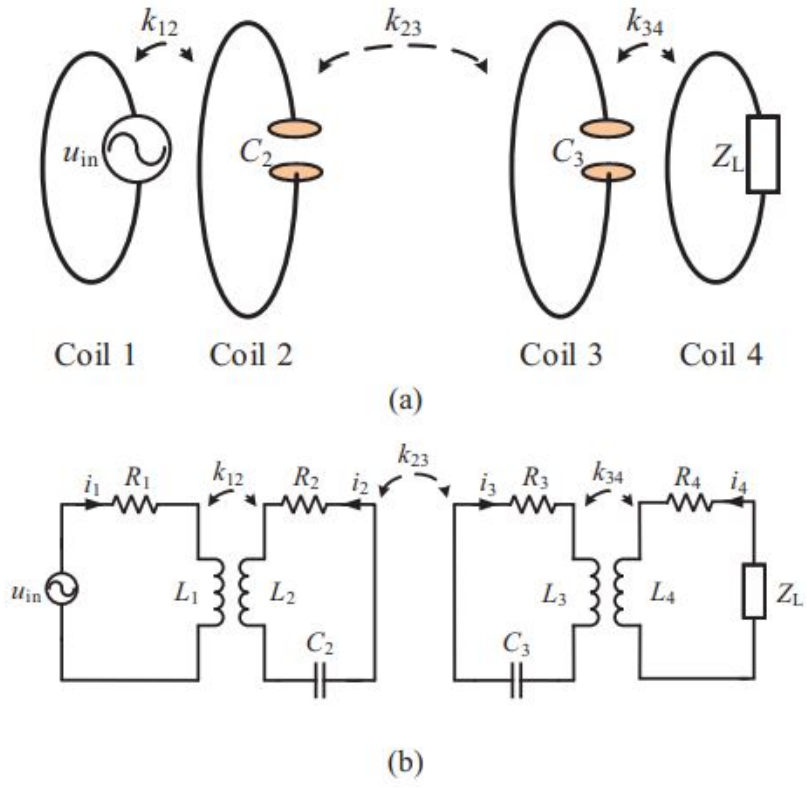


Figure I-4: The 4-coil WPT system. (a) Physical structure. (b) Lumped circuit model [17]

on other type of coil-based solutions. However, the corresponding levels of power are not given so that one cannot easily compare this solution with other existing alternatives.

In [20], an example on the development of an integrated circuit using the inductive link to transfer power through biological media is introduced. The receiver is fully integrated on a single chip in standard CMOS with no additional postprocessing steps or external components which is an advantage of this chip. The dimension of the chip is  $2mm \times 2.18mm$  and the optimal operating frequency is between  $160MHz$  and  $187MHz$ . The transmitter can safely emit over  $100mW$  at  $160MHz$  to a neural implant while staying under SAR limitations. However, with a distance of  $1cm$  between the chip and the transmitter the power transfer efficiency is no more than  $1.42\%$  in air medium and about  $0.8\%$  with bovine muscle medium.

Another health care application is the mechanical circulatory support systems [21]. In this work, a self-driven circuit with minimized volume was developed to achieve efficiencies higher than  $90\%$ . The transferred power can reach about  $30W$  to meet with the requirement of the application. This level of transmitted power is extremely large. However, one should keep in mind that it comes with specific constraints and drawbacks. First, the receiver is a large coil of  $3.4cm$  diameter, hardly compatible with implants (see Fig. I-5). Secondly, the circuit is also quite large due to heat dissipation constraints (see Fig. I-5). To date, one cannot be sure about the actual levels of power that a miniaturized and/or integrated circuit which would behave similarly could stand. In addition, the frequency is still relatively high ( $800kHz$ ) for this size of receiver, and a reduction of the receiver size would come with a higher frequency. Last but not least, the device is sensitive to the orientation of the receiver with respect to the emitter, as one can see in Fig. I-5 where the two have been specifically placed and fixed in front of each other to ensure maximum power transfer. Such a precise orientation would be hardly reachable in real-life implementation. Regardless of these drawbacks, this solution is one of the best competitors for the wireless power supply of implanted systems.

Some recent solutions have been proposed based on a rotor magnet [24, 25] for EM

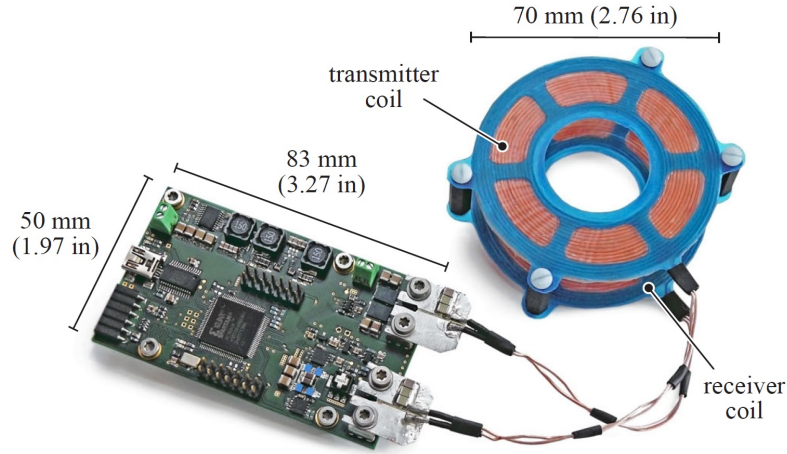


Figure I-5: Photograph of the proposed prototype including the energy transmission coils. [21]

Table I.1: Examples on the inductive power transfer application

<i>Ref.</i>	<i>Year</i>	<i>Working distance</i>	<i>Power level (max)</i>	<i>Frequency</i>	<i>Receiver dimension</i>
[22]	2019	20 to 50mm	447mW	13.56MHz	Length: 30mm Width: 20mm
[23]	2019	10mm	31.62mW	434MHz	Coil diameter: 1.6mm
[21]	2015	20mm	30W	800kHz	Coil diameter: 3.4cm Thickness: 40μm
[20]	2014	1mm	1.42mW	160MHz	Chip length: 2.18mm Chip width: 2mm

power transfer at low frequencies ( $<200\text{Hz}$ ). The transmitter consists of a rotating permanent magnet. The receiver is made from biodegradable coils (e.g. Magnesium-based). A schematic of the solution and its working principle are shown in (Fig. I-6).

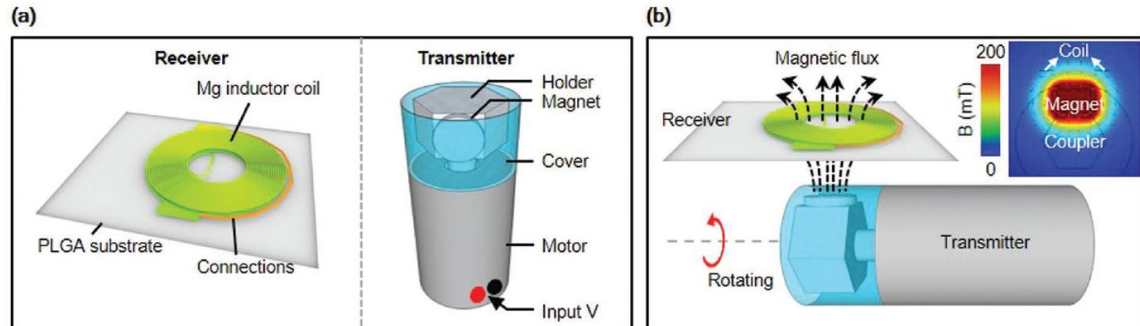


Figure I-6: (a) Schematic illustrations of a Mg coil as the receiver and a rotating magnet as a transmitter for wireless power transfer. b) Schematic diagram of the working principles. [24]

The transmitted power can be controlled by controlling the rotation speed of the magnet. At a frequency of  $58\text{Hz}$  the peak power density can reach  $10\text{mW.cm}^{-2}$  when changing the working distance between 4 to  $10\text{mm}$  (the diameter of the coil is about  $3.2\text{cm}$  and the thickness is about  $30\mu\text{m}$ ). The same concept was introduced in [25]. However, these solutions reach very low peak output voltages ( $<300\text{mV}$ ) hardly compatible with conditioning circuits mainly to overcome the diode threshold voltage. In addition, they bring out a peak output power of around  $20\text{mW}$  but the corresponding average output power is very low, even if the data provided in the literature is insufficient to determine its exact value. The available data suggest that we can expect the average output power to be lower than  $100\mu\text{W}$ . For these reasons, we do not consider these solutions as potential candidates for our targeted applications.

### 3.1.2 Capacitive power transfer

The first experience on capacitive coupling of Nikola Tesla's was done in 1890, [11]. In a typical structure of a capacitive power transfer (CPT) system, the coupling is done by two capacitors as presented in Fig. I-7 [26, 27, 28]. Through a compensation network at the primary side (power transmitter), an alternative voltage source is

connected to the first plates of the two coupling capacitors and at the secondary side (power receiver) the second capacitors plates are connected to a rectifier in order to power a load or charge a battery.

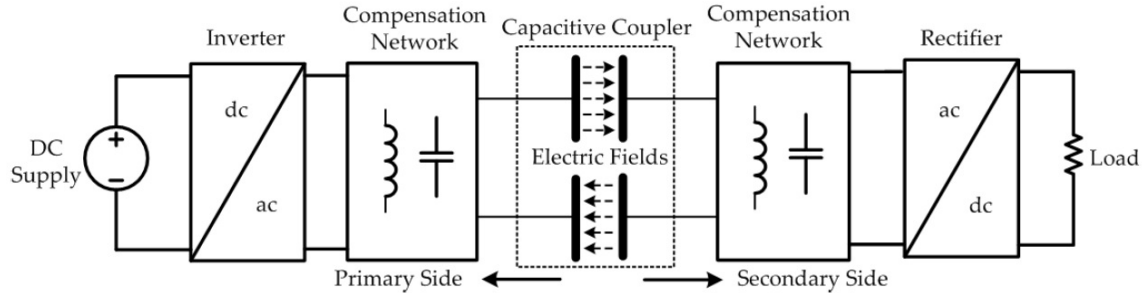
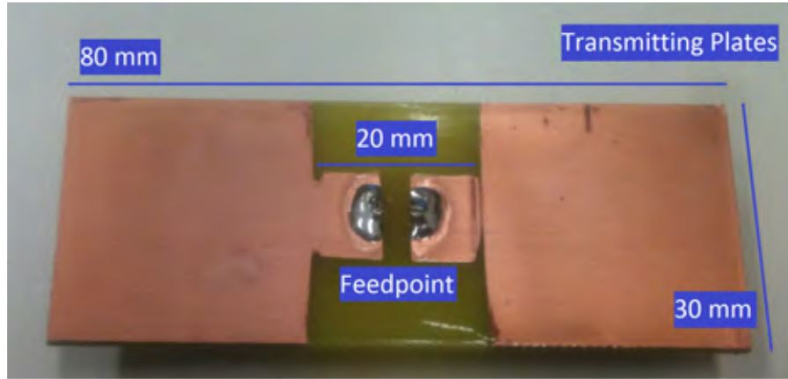


Figure I-7: Typical structure of a capacitive power transfer (CPT) system [28]

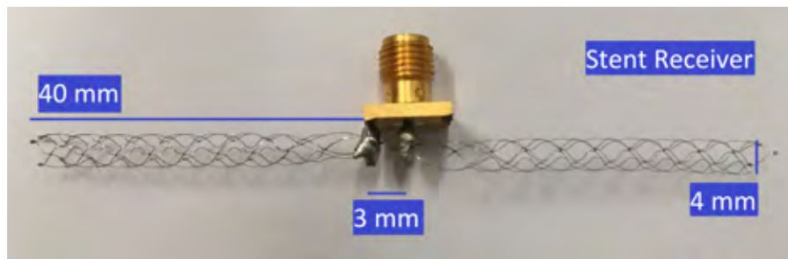
One of the disadvantages of this technique is that it is very sensitive to the gap distance between the plates of the capacitors, which should typically be below 1mm in order to reach 90% of efficiency [11]. The frequency range can go up to hundreds of MHz.

CPT technique can be used for health care application. An example of CPT solution experimented on a primate is given in [29]. In this study, an experiment was performed on a primate cadaver. The frequency range tested in this application is between 50 and 200MHz. The smallest receiver tested is constituted of 2 patches of  $10 \times 20mm^2$ . It was implanted at 7mm in the arm of the cadaver. The measurements show a possible power transfer at approximately 100mW without exceeding the limits on the SAR regulation ( $1.6W/kg$ ). This study shows that CPT-based systems are a viable alternative to power implants.

A more recent example of CPT technique is the stent-based system studied in [30]. In this technique two stents are used as the receiver plate of the capacitor link. Each stent measures 4 mm in diameter and 40 mm in length. The transmitter is a board of  $30mm \times 80mm$  formed by two plates electrically isolated as shown in Fig. I-8. The power transfer efficiencies achieved are 2.6% and 1% when the stent is placed at depths in bovine muscle tissue of 15 mm and 30 mm respectively, which highlights that this transduction principle loses a lot of emitted energy in the environment of the implant. Nonetheless, the capacitive link can accept a maximum of 53mW input



(a)



(b)

Figure I-8: Experimental components used for the capacitive power transfer setup a) The transmitting plate b) the receiver: two 40 mm long stents [30]

power before exceeding the safe specific absorption rate limit of 1.6 W/kg averaged over 1 g of tissue. This corresponds to a transmitted power of approximately 1.4mW. In this example the peak of transferred power is measured at frequencies between 200MHz to 400MHz.

An invivo demonstration of an implant based on charge-balanced rectification of high frequency (HF) current bursts through skin electrodes is introduced in [31]. The implant is a tube with a 3cm length and a diameter of 1mm. The power is delivered as a HF bursts (1MHz) with a repetition frequency of from 10Hz to 200Hz. The concept of the solution is shown in Fig. I-9). The same concept was presented in [32] where the transferable power can reach 1mW.

One recent implementations of CPT can be found in [33], where a deeply-implemented biomedical CPT solution is introduced. This new technique is called "Capacitively Coupled Conductive Transcutaneous Energy Transfer (CCCTET)". It operates at 6.78MHz and offers an appreciable amount of safe power to be delivered deep in the

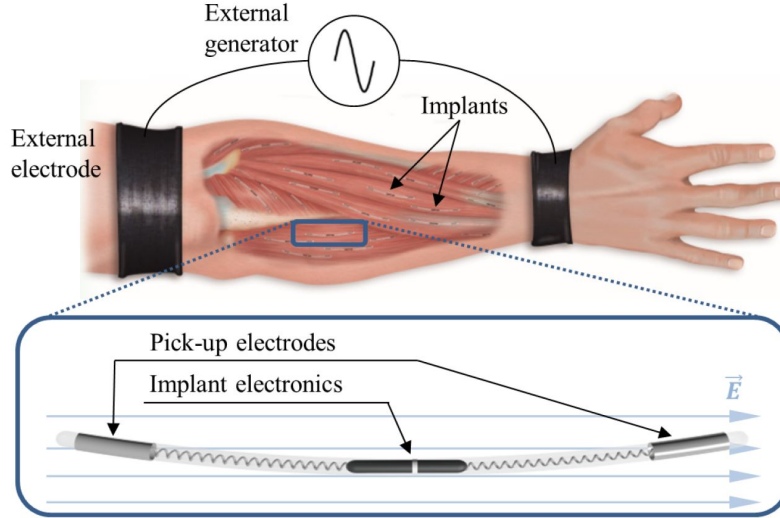


Figure I-9: Explanation of the thin tube-shape implant concept. When the tube is exposed to an electric field generated by a pair of external electrodes, the power will draw to the implant by the internal electrodes located at its opposite ends. [32]

tissue. The author compared this new technique with other solution with respect to the power density and implantation depth. This technique is able to deliver  $10mW$  to a device implanted deeply in the body at about  $75mm$ .

Table I.2: Examples of capacitive power transfer

<i>Ref.</i>	<i>Year</i>	<i>Working distance</i>	<i>Power level (max)</i>	<i>Frequency</i>	<i>Receiver dimension</i>
[33]	2020	$75mm$	$15mW$	$6.78MHz$	Plate diameter up to $2cm$ Thickness: $30\mu m$
[32]	2020	–	$1mW$	$5MHz$	Tube diameter $< 1mm$ Length $< 15mm$
[30]	2018	$15$ to $30mm$	$1.4mW$	$200MHz$ to $400MHz$	Stent diameter: $4mm$ length: $83mm$
[29]	2017	$7mm$	$94mW$	$50 - 200MHz$	Length: $20mm$ Width: $10mm$

To get rid of certain constraints imposed by inductive or capacitive power transfer such as the relatively high frequencies and the sanitary limitations, a more exotic alternative exists with light-based power transfer. In the next section, we will briefly present some of these implementations to evaluate how promising they are in order to power implants in the human body.

## 3.2 Light sources

Since the discovery of the photovoltaic effect in 1839 by Becquerel [34, 35], the solar cells were always a hot topic for many scientific communities. These cells are used and studied as light harvesters, as light receivers for wireless communications [36] and also for Wireless power transfer [37]. A photovoltaic cell can be modeled under certain assumptions as a single-diode equivalent circuit (see Fig. I-10) [38] which is derived from the double diode model explained in [39].

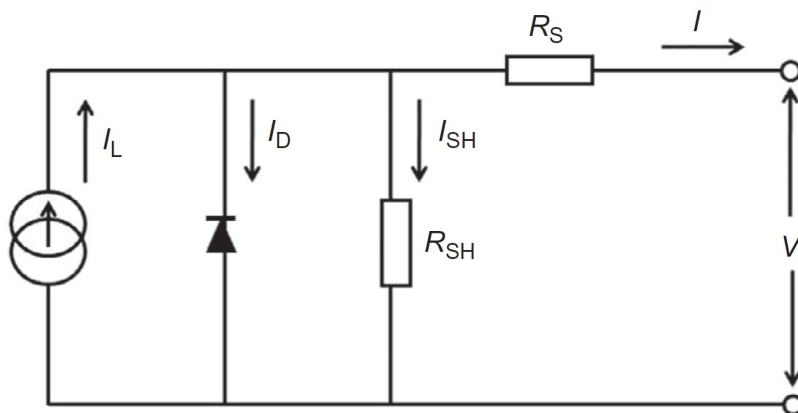


Figure I-10: Single diode equivalent circuit [38]

For a given temperature and irradiance the current–voltage characteristic of the p–n junction is given as mentioned in [38] by:

$$I = I_L - I_0 \left( e^{\frac{q(V + IR_S)}{nkT}} - 1 \right) - \frac{V + IR_S}{R_{SH}} \quad (A) \quad (I.3)$$

The parameters in this equation are: the short circuit current  $I_{SH}$  (A), the light current  $I_L$  (A), the diode reverse saturation current  $I_0$  (A), the Boltzmann constant  $k$  ( $m^2 kg s^{-2} K^{-1}$ ), the temperature  $T$  (K), the diode ideality factor  $n$ , the output voltage  $V$  (volt), the series resistance  $R_s$  ( $\Omega$ ), the shunt resistance  $R_{SH}$  ( $\Omega$ ).

We can find in the literature many examples of implantable medical devices powered by photovoltaic energy harvesters [37]. For instance, this technology can be applied on devices that power cardiac implants (e.g. pacemaker). An example of flexible solar cell arrays which requires simple dermatological surgery was introduced

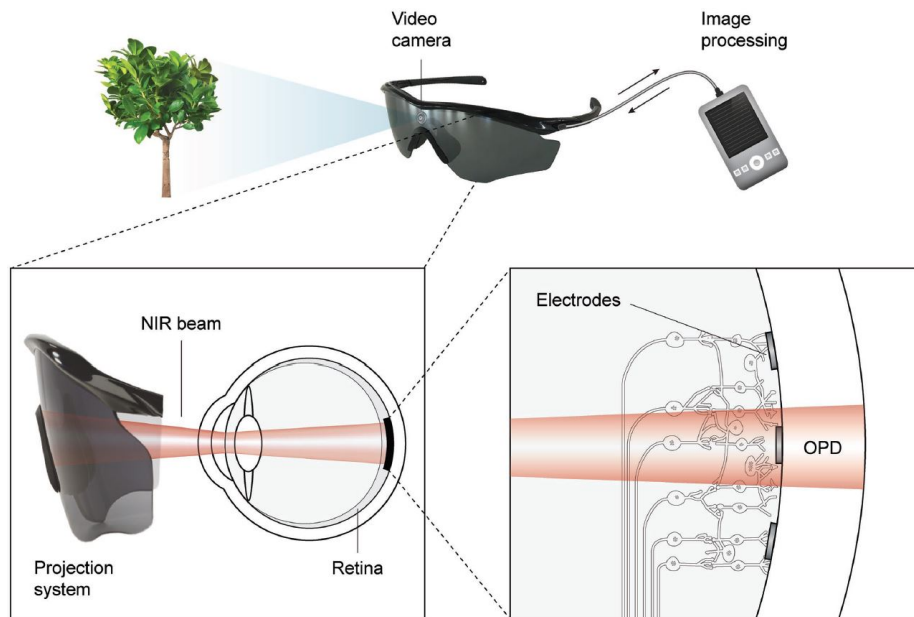


Figure I-11: Concept of photovoltaic retinal implant based on NIR-sensitive OPDs. The image captured by a head-mounted camera is processed by a portable computer and projected onto the subretinal implant via a near-to-eye projection system using pulsed NIR light. The OPD array converts incoming light into pulsed photocurrent that is delivered to nearby nerve cells by stimulating microelectrodes [40]

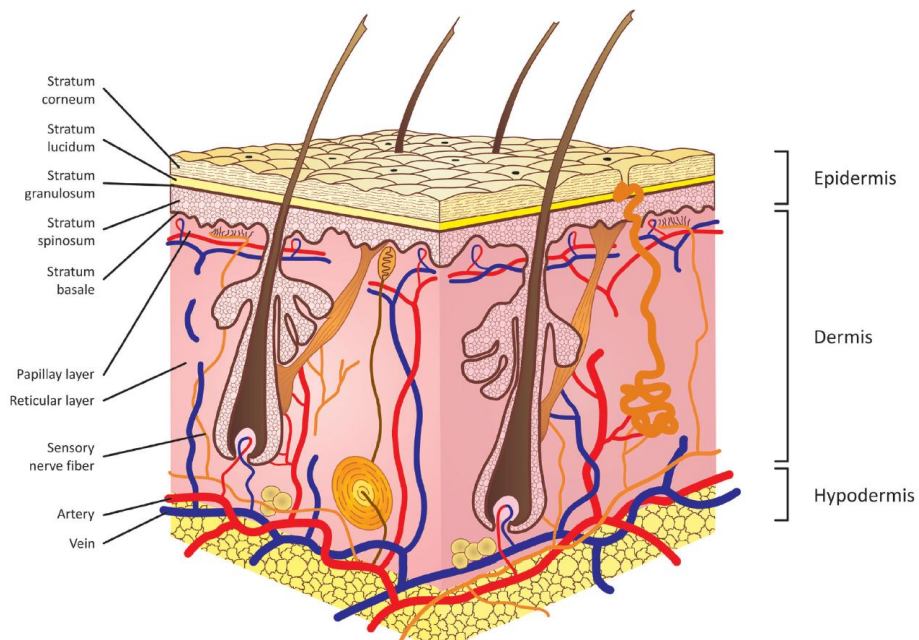


Figure I-12: Layers of human skin [41]

in [42]. These PV harvesters can be found also in retinal implants that help to restore the sight of a patient suffering from degenerative eye diseases. In [40] a photovoltaic retinal prosthesis is introduced. It uses organic photodiodes (OPDs) sensible to near infrared (NIR) light. The concept of this solution is shown in Fig. I-11. Also we can find the PV technology applied on devices implanted in the subcutaneous region of the skin (hypodermis in Fig. I-12 [41]).

Another example on PV application implanted under the skin is given in [43]. This example predicts the performance of the proposed PV device only with simulation using finite element method. The simulation results showed a maximum output power level of  $17.2mW$  with an efficiency of 17.2%. Moreover, we can find also biodegradable photovoltaic material used for implantable devices. In [44] an example of a device that provides active diagnostic or therapeutic function over a timeframe, and then disappears within the body to avoid secondary surgical extraction.

Table I.3: Examples on photovoltaic power transfer

<i>Ref.</i>	<i>Year</i>	<i>Working distance</i>	<i>Power level (max)</i>	<i>Power density (max)</i>	<i>Receiver dimension</i>
[45]	2020	1mm	$8.4\mu W$	$74\mu Wcm^{-2}$	surface: $11.1mm^2$ width: $4\mu m$
[44]	2018	4mm	$60\mu W$	–	Length: $8.77mm$ width: $4.2mm$
[42]	2016	3mm	$0.647mW$	–	Length: $13mm$ width: $10mm$

### 3.3 Acoustic sources

#### 3.3.1 Piezoelectric material

Piezoelectric materials have the ability to generate an electric field under applied mechanical stress (direct effect). Inversely, they are also able to develop internal stress when they are exposed to electric field (converse effect). The direct effect was discovered by the Curie brothers (Pierre and Jacques Curie) in 1880 and the converse effect by Gabriel Lippmann in 1881 [46, 47]. The mechanical stress could be generated

by ultrasound waves or mechanical contact. Fig. I-13 illustrates an idealized response of a piezoelectric cube in the two effects (direct and converse). Hence, piezoelectric materials are used for actuation and sensing applications as energy harvesters [48] [49] for many applications such as motors and actuators [50], frequency standards (e.g. crystal oscillator) [51] and sonar [52].

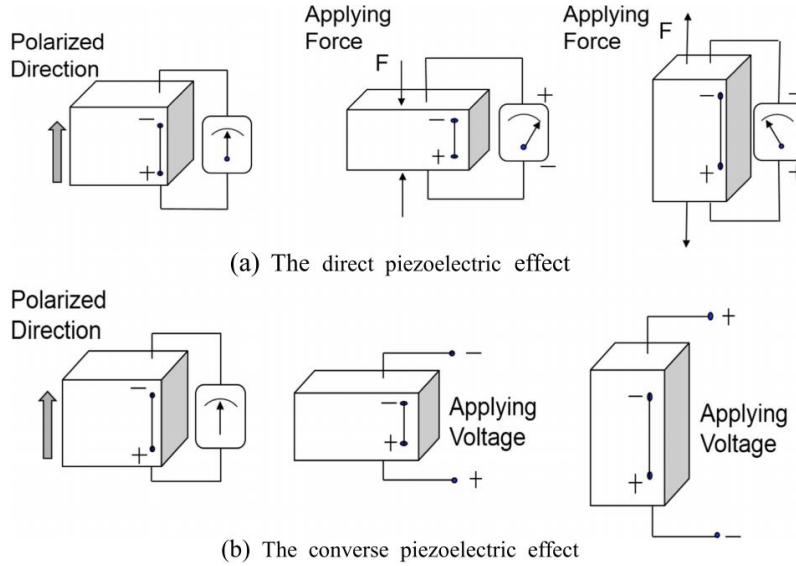


Figure I-13: Schematic representation of the longitudinal direct (a) converse (b) piezoelectric effect [53].

Ferroelectric perovskites ceramics as  $Pb(Zr, Ti)O_3$  (PZT) could be a good example to understand how piezoelectric materials work at the crystallographic level. These PZT ceramics are among the materials exhibiting the largest piezoelectric effect. Above the Curie temperature the unit cell of the material has a cubic structure as shown in Fig. I-14 (a). Below this temperature these units transform into asymmetric tetragonal structure Fig. I-14 (b). This makes the unit cell polarized due to the displacement of the atom which sits at the body-center position of the cube (B-site atom). In ceramics, these polarized cells form adjacent domains. Typically, these domains are randomly oriented as shown in Fig. I-15 (a). This makes the overall net polarization of the material negligible. In order to orient these domains in the same direction, a poling process is required. In this process, a strong electric field is applied to the material (Fig. I-15 (b)). After this process most of the domain retain

their alignment (Fig. I-15 (c)) [54, 55]. As a result, the material will have a remanent polarization ( $P_r$  in Fig. I-16) and can be used as a piezoelectric transducer.

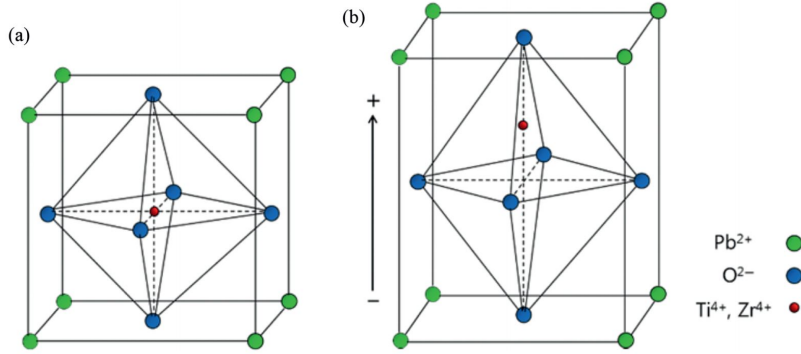


Figure I-14: Perovskite PZT unit cell. (a) PZT unit cell in the symmetric cubic state above the Curie temperature. (b) Tetragonally distorted unit cell below the Curie temperature [54].

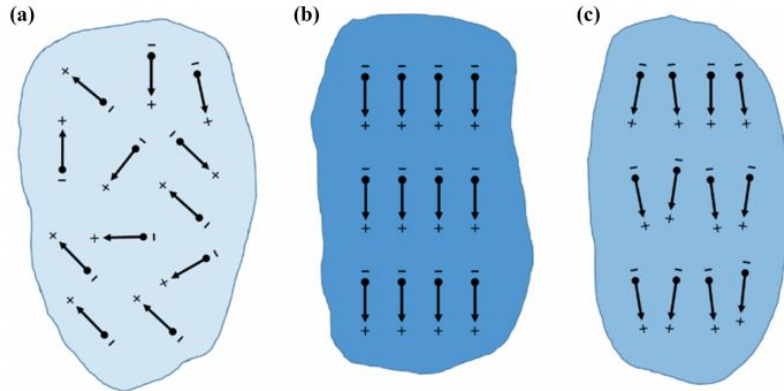


Figure I-15: Piezoelectric domains in piezoelectric materials. (a) Randomly oriented domains, Domains during (b) and after (c) the poling process. [54]

From a system-level perspective, piezoelectric transducers are generally modeled as an lumped equivalent RLC circuit [56] (see Fig. I-17). This model will be used and explained further later in this manuscript. This is a simple single degree of freedom (SDOF) model where  $\sigma_{in}$  is an equivalent stress generator which represents the stress developed as a result of external vibrations.  $\alpha$  is the equivalent turns ratio of the transformer which represents the coupling between both electrical and mechanical domains.  $C_p$  is the capacitance of the piezoelectric bender.  $u$  is the voltage across the piezoelectric device. The mass or the inertia of the generator is represented as an

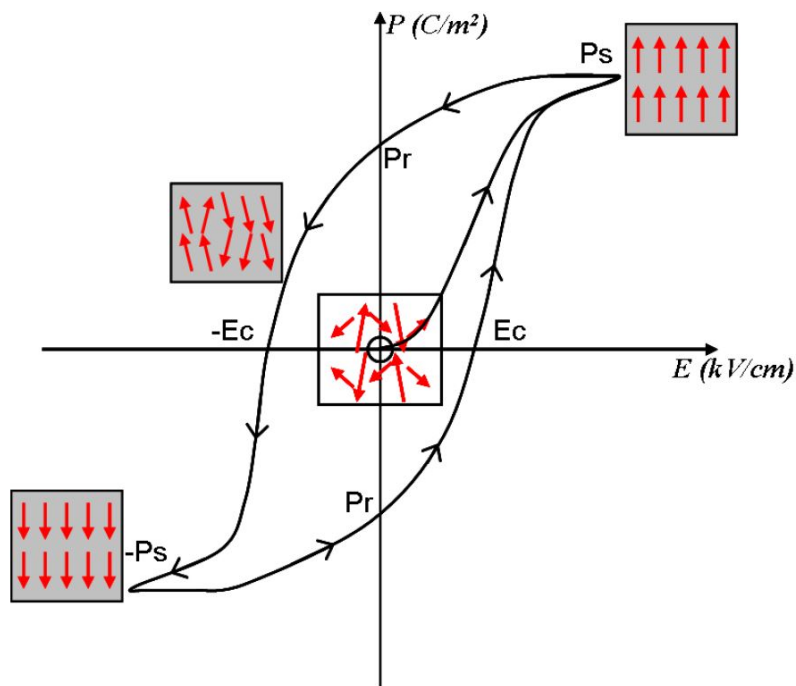


Figure I-16: Schematic diagram of ferroelectric hysteresis graph. Here the definitions are as follows;  $E_c$ : coercive field;  $P_s$ : saturation polarization;  $P_r$ : remanent polarization. The arrows indicate direction of polarization for dipoles in a domain. [55]

equivalent inductor  $L_m$ . The damping is represented by an equivalent resistor  $R_m$ . The mechanical stiffness is represented by an equivalent capacitor,  $C_m$ .

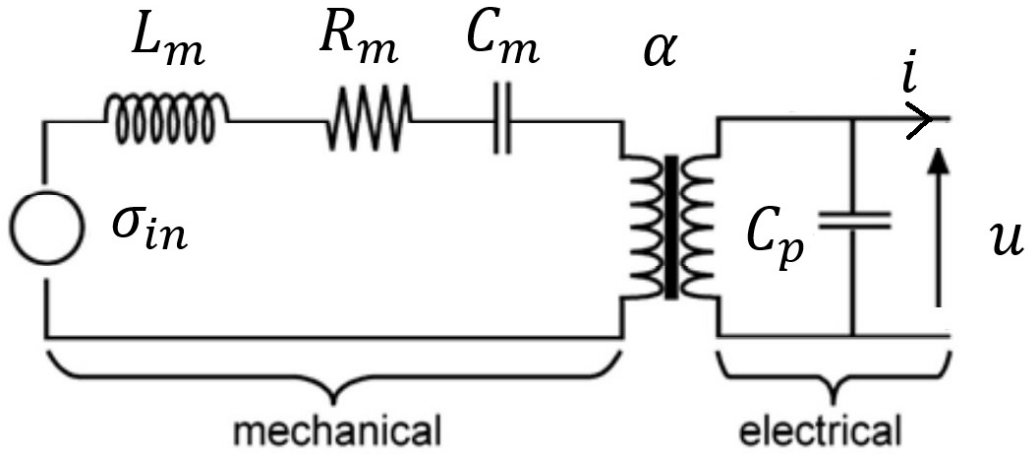


Figure I-17: Circuit representation of the piezoelectric generator. (Note that node 1 is used in the derivation of equation [56]).

### 3.3.2 Acoustic power transfer based on piezoelectric transducer

Typically, acoustic power transfer (APT) uses a pair of piezoelectric transducers (a transmitter and a receiver) to transfer energy in the form of ultrasound waves. A fundamental schematic of the APT technology is shown in Fig. I-18. This APT system (transmitter and receiver) can be represented as an equivalent lumped circuit as shown in Fig. I-19.

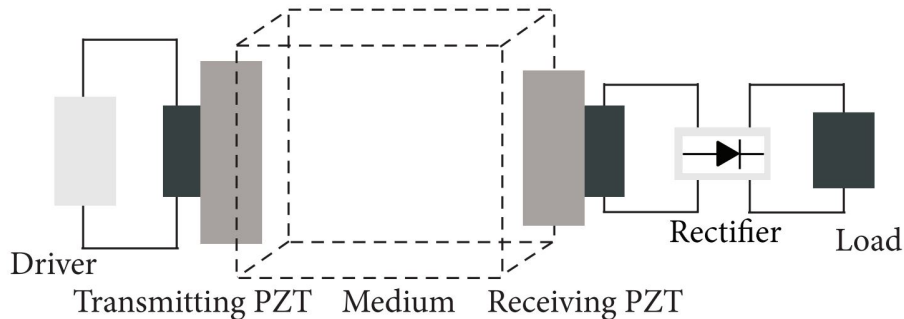


Figure I-18: Schematic of acoustic power transfer technology based on piezoelectric transducers [47].

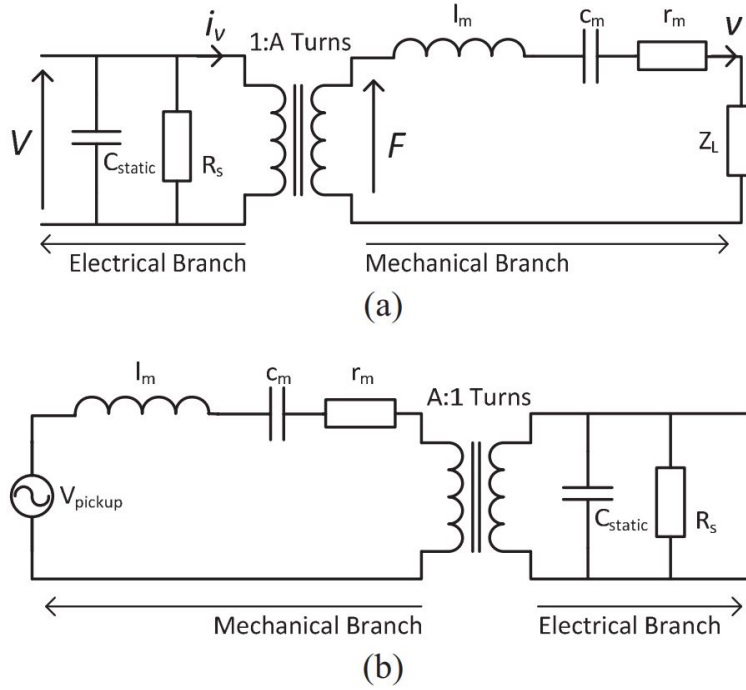


Figure I-19: (a) Transmitting transducer equivalent circuit. (b) Pickup transducer equivalent circuit. [57]

The acoustic wave behaves differently in two region denoted by: near-field and far-field [1]. The near-field is when the receiver (RX) is close to the transmitter (TX). This region is defined as the region where the acoustic beam is convergent. This zone only exists as long as the diameter of the emitter is larger than the wavelength of the acoustic wave. The other is the far-field region where the acoustic wave is spherical and where the acoustic beam diverges. Hence, in this region, the wave amplitude decreases when the distance between RX and TX increases. The transition region between near and far fields is the best location where the receiver should be installed, to get the largest density of acoustic energy. This distance is known as Rayleigh distance [58] and is defined by I.4.

$$L = \frac{D^2 - \lambda^2}{4\lambda}(m) \quad (\text{I.4})$$

Where  $\lambda$  (m) is the wavelength of the acoustic wave and  $D$ (m) is the diameter of the transmitter (TX).

A representation of the regions of an acoustic wave is shown in Fig. I-20.

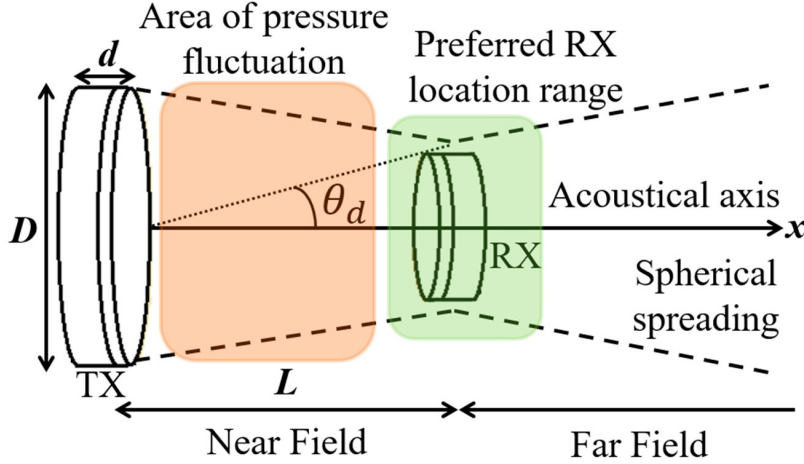


Figure I-20: Representation of near-field and far-field regions of an acoustic wave generated by TX and incident on RX [1].

In table I-21, we present a summary of a review on APT for different applications [47]. As shown in the table, the technique can be used for implementable medical applications. For these devices, the operating frequency range goes from  $35kHz$  to  $30MHz$ . The efficiency can reach 45% at  $400mm$  of gap distance. Other review on implants using APT technique can be found in [58]. In this review the author also make a comparison between APT and EM wireless power transfer solution.

AET type	Frequency (min-max)	Active range (max)	Efficiency % (max)	Power level (max)
Wall-through	24.5 kHz–13.56 MHz	1 m	88	1.068 kW
Implants	35 kHz–30 MHz	400 mm	45	5.4 W
Others	20.46 kHz–782 kHz	8.6 m	20	2 W

Figure I-21: Summary of the review on APT applications [47].

APT technique can also be a solution for deep implanted medical devices. In [59], the working distance is about  $70mm$  with 1% efficiency. In [60] is an example of ultrasonic link in a phantom material medium that mimics the human tissue with a higher working distance of  $10.5cm$  and higher efficiency up to 1.6%. An ultrasonic solution for millimeter-sized biomedical implants is introduced in [61]. In [62], an application based on piezoelectric micromachined ultrasonic transducers (pMUT) was presented

and compared with a commercial off-the-shelf (COTS) transducers. The output voltage is about 1.41V with pMUT structure and higher with of COTS structure 0.96V. [63] is an example of APT with transcutaneous ultrasounds. The operating frequency of the application is 650kHz. The working distance go up to 5cm and the peak power transfer efficiency of 39% at a power level of 100mW. One of the main difficulties of APT is the need for positioning the ultrasonic source directly in contact with the skin. A recent work on an acoustic power transfer for neurostimulators has been reported in [64]. These examples show an advantage of APT solution on with EM based solution in term of operating frequency which is relatively low.

Table I.4: Examples of acoustic power transfer

<i>Ref.</i>	<i>Year</i>	<i>Working distance</i>	<i>Power level (max)</i>	<i>Frequency</i>	<i>Receiver dimension</i>
[64]	2021	18.5mm	9.43mW	3.6MHz	diameter: 6mm
[62]	2019	40mm	0.23mW	88kHz	surface: 2mm × 2mm Thickness: 40μm
[60]	2014	105mm	28mW	1MHz	Length: 10mm width: 5mm
[59]	2012	70mm	8mW	200kHz	diameter: 10mm Thickness: 1mm
[63]	2010	50mm	100mW	650kHz	diameter: 15mm Thickness < 5mm

### 3.4 Comparison between the WPT techniques

To compare the different WPT applications we have built a graph, reported in Fig. I-22. It represents the amount of power transferred in each application as a function of the surface of the receiver. Since the operating frequency is also an important parameter to take into account, we indicate it also (when the technology is not DC). These applications are divided into three categories depending on the energy transmitted to the implants: electromagnetic, acoustic and light. We can notice that the techniques that rely on EM sources are positioned at the top of the graph which means that, these techniques show a great potential. However, the operating fre-

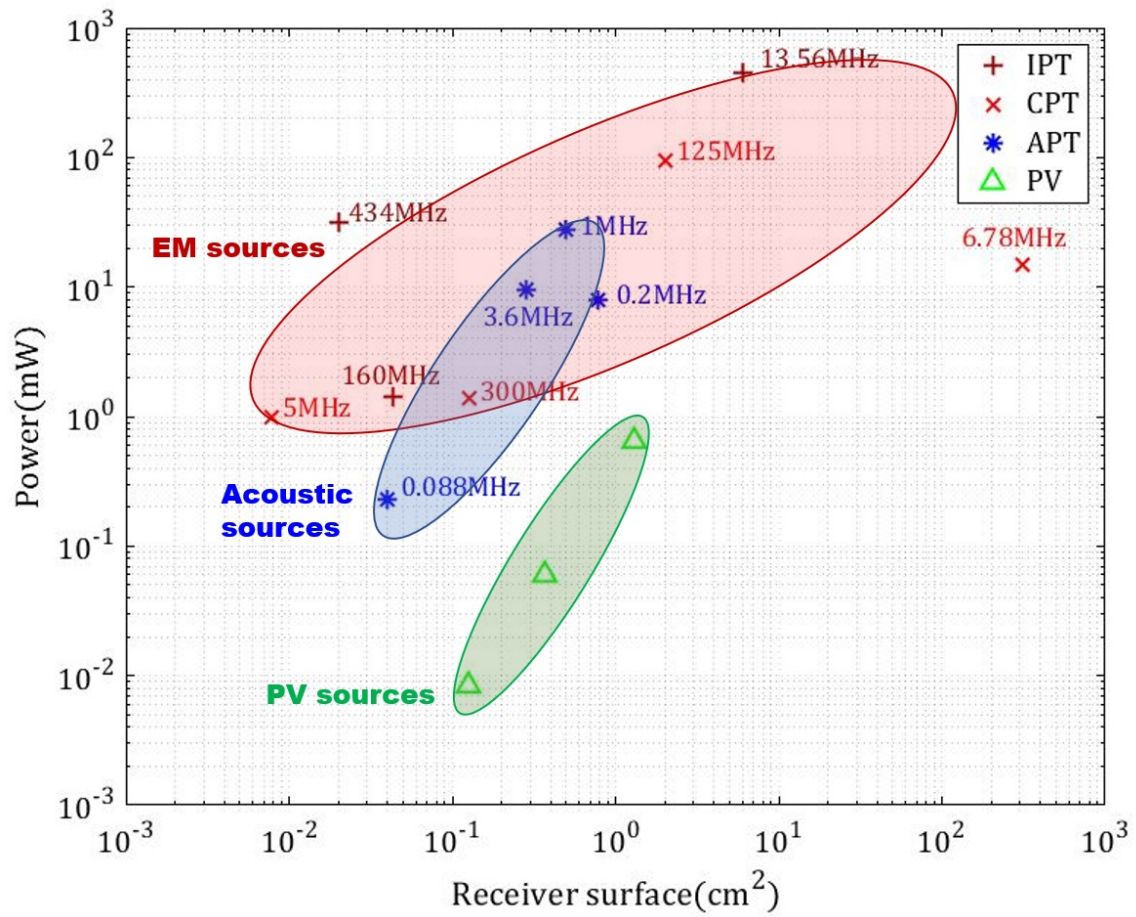


Figure I-22: Graphical comparison between different application for 4 wireless power techniques based on the power level and the surface of the receiver used in the application

quency of these application tends to be large ( $>5\text{MHz}$ ). We will keep this in mind for our investigations. Acoustic power transfer delivers a decent amount of power at large dimensions (receiver of around  $1\text{cm}^2$  typically). However, this power decreases significantly if one tries to reduce the size of the receiver. This gives an advantage for acoustic power transfer technologies. Another drawback of APT is that it requires a precise orientation and alignment of the receiver with the transmitter to be at the optimal position [65]. Light-based sources are positioned at the low part of the graph which means that one can expect very low power from these techniques. As illustrated on the graph, recent works based on light power transfer have still managed to achieve a good amount of power (typically  $10\text{mW}$  with small receivers) so it seems that these solutions may have a promising future. As discussed previously, acoustic sources present one advantage compared to EM sources : they reach a decent amount of power for relatively small devices at low frequencies (generally lower than  $1\text{MHz}$ ) while EM sources require frequencies larger than  $10\text{MHz}$  to bring out sufficient power transfer. In this thesis, we try to find the best of both worlds : a hybrid technology combining acoustic power transfer (mechanical vibrations) and EM power transfer (transfer via electromagnetic waves) which combines a high output power with small receiver surface for relatively low frequencies and being less sensitive to the orientation of the emitter compared to EM or acoustic competitors.

## 4 Study case: wireless charging of implants

### 4.1 Implantable medical devices

Implantable medical devices, named also implants, are devices implanted into the body either by a surgical or medical method, or introduced by a medical intervention into a natural orifice. Their main function is to detect and/or fix a failure of an internal organ. Cardiac pacemakers, coronary and artery stents, hip implants, interocular lenses and implantable insulin pumps are common examples on implantable

devices. Fig. I-23) shows the power requirement of some implantable medical devices [66]. Some of these implants do not need battery to operate as the batteryless nerve stimulator which is a pain control on demand device [67] (see Fig. I-24). Other implants are battery-powered. When the battery is discharged, a surgery is needed to recharge it again. For devices near to sensitive areas in the body (e.g. heart, brain), heavy surgeries are requested, with risks for patients. This leads the importance of charging wirelessly these devices. The pacemaker is an example of these implants. It controls the heartbeat by generating electrical impulses and delivering them to the heart muscle. This device requires between  $20\mu W$  to  $50\mu W$  of power for the basic operating functions as the sensing, the control and the impulse generation [68]. The volume of the pacemaker is estimated to between  $9 - 45cm^3$  [69]. In this thesis we will try to position our WPT solution with respect to such criteria of the implant design. We took for example the design criteria of the pacemaker in table I.5). The WPT solution should also be biocompatible to not toxicate the tissue once installed inside the body. However this criteria will not be studied in this work. A further study on the packaging of the device could be investigated in future work.

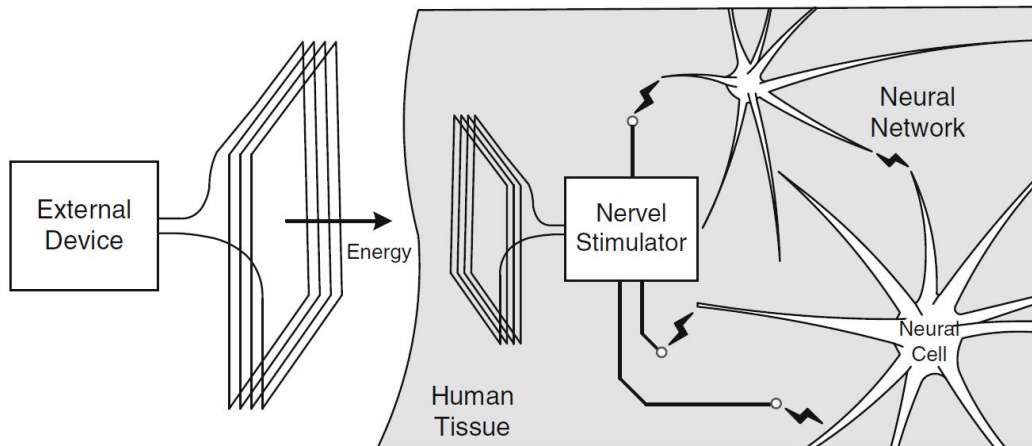
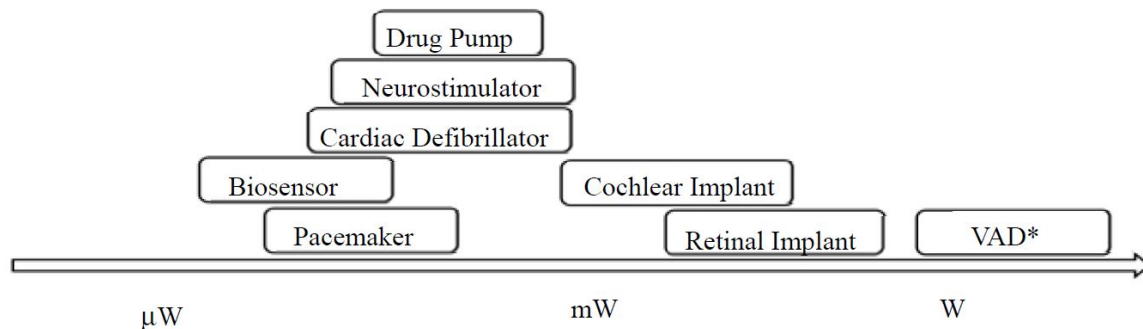


Figure I-23: Wireless power transfer used in a nerve stimulator [70]



\*Ventricular Assist Device

Figure I-24: Range of power requirements of example implantable medical devices [71] .

Table I.5: Pacemaker specification

<i>Power consumption</i>	<i>Dimension</i>	<i>working distance</i>	<i>weight</i>
20 – 50 $\mu$ W	9 – 45 $cm^3$	skin thickness 2 – 3mm [72]	20 – 50g

## 4.2 Magnetolectric transducers for wireless charging

The magnetolectric materials exhibit two effects direct and reverse. The direct effect was discovered in 1888 when the physicist Wilhelm Röntgen found that if a dielectric moves in an electric field it becomes magnetized. The reverse effect came 17 years later when it was discovered that if a dielectric moves in a magnetic field it becomes polarized [73]. The material that has these two properties are called magnetolectric material. Fig. I-25 shows different applications based on ME composites [74]. Magnetolectric transducer can be manufactured using ME materials or composite systems like  $Cr_2O_3$ . In Fig. I-26 we show the most three commonly used ME architectures: particulate composites(0-3), layered composites(2-2) and rod composites(1-3) [74]. Another way to build ME transducers is by joining piezoelectric and magnetostrictive materials.

We have introduced the piezoelectric effect in section 3.3.2 of acoustic power transfer solution. The magnetostriction effect of magnetostrictive materials was discovered in 1842 by the english physicist James Prescott Joule. This effect was observed on materials that changed their length (L) in the presence of magnetic field (H). The first

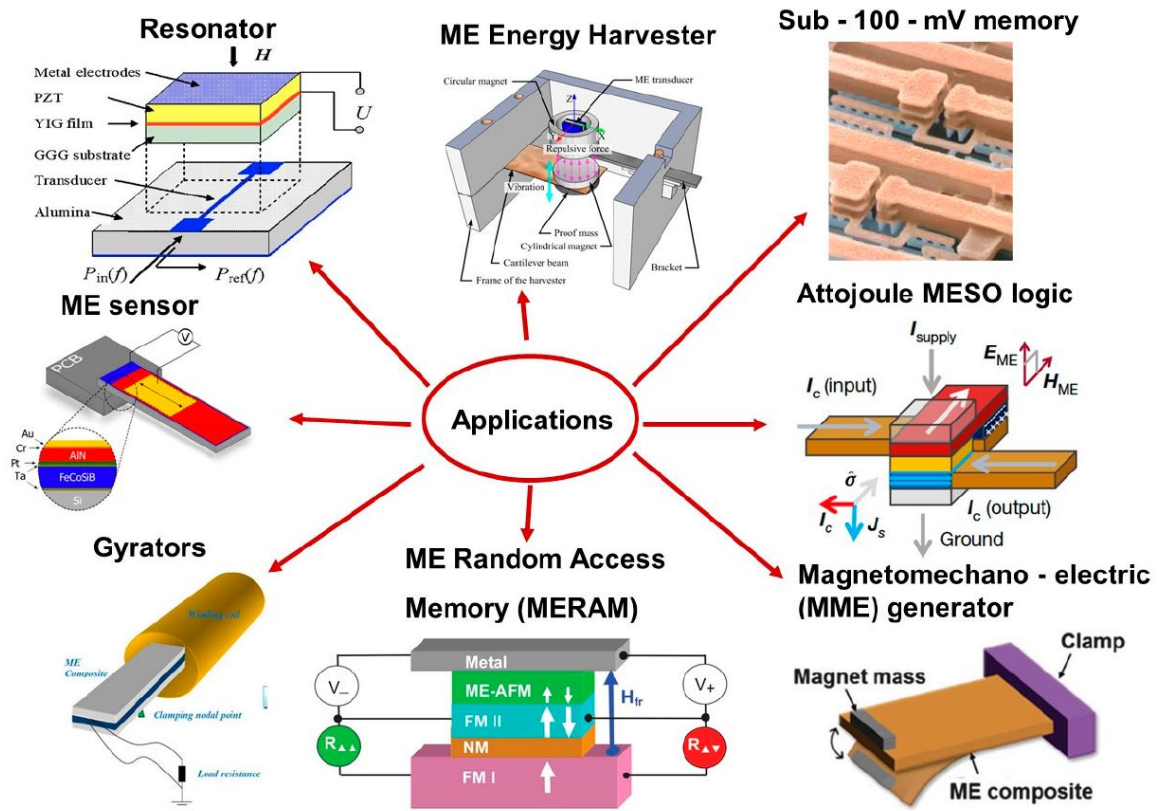


Figure I-25: Various applications of Magnetoelastic composite [74]

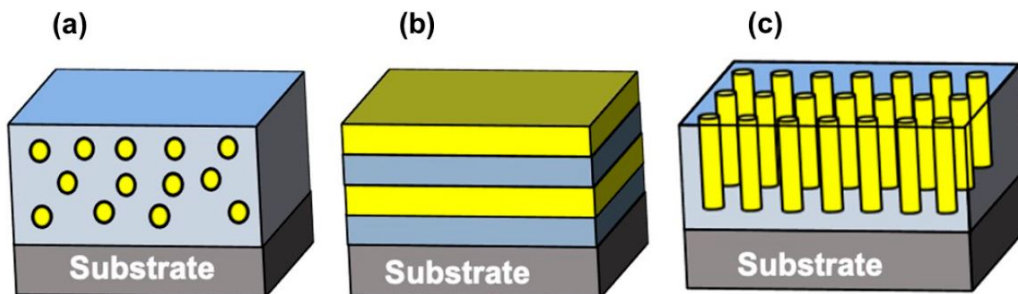


Figure I-26: Schematic of (a) 0-3, (b) 2-2, and (c) 1-3 composite nanostructures [74]

observation was on an iron sample [75]. The magnetostriction coefficient  $\lambda = \Delta L/L$  is defined to quantify this effect.  $\Delta L$  is the material deformation when it is exposed to magnetic field [76, 77]. The cause of this MS effect is explained as a result of the rotation of small magnetic domains in the material. This re-orientation causes internal strains in the material structure [78]. The strains can lead to the stretching, in the case of positive magnetostriction ( $\lambda > 0$ ), and the shrinking in the case of negative magnetostriction ( $\lambda < 0$ ) as shown in Fig. I-27. For instance, when positive magnetisation material are exposed to an AC magnetic field ( $H$ ) the material will stretch for positive and negative magnetic field  $H$  as shown in Fig. I-28(b).

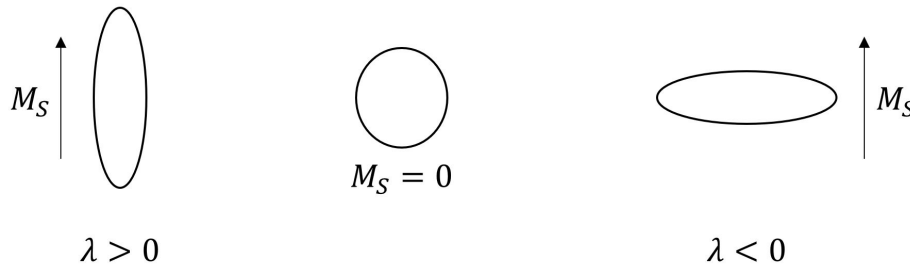


Figure I-27: Change of shape for positive or negative

The ability of MS materials to convert the energy between mechanical and magnetic form make them suitable for both actuator and sensor applications. When MS and PE materials are glued together they can behave as an ME transducer. ME transducer can be used for wireless power transfer. For instance, when the MS layer is exposed to a dynamic magnetic field it will transform it to vibration. This will make the glued PE layer vibrate too and generate at its terminals electric field which can power a load or charge a battery. Some ME transducers operate at frequency relatively low ( $70kHz$ ) in comparison to other solution based on EM sources such as the RFID  $125kHz$  and  $13.56MHz$ . In this case, the allowed magnetic fields amplitude when using these ME transducers is about  $21A/m$ . This is an advantage on RFID solutions ( $16A/m$  for  $125kHz$  and  $0.15A/m$  for  $13.56$  see Fig. I-29). For the aforementioned reasons, ME transducers may be a WPT solution which matches different criteria of an implant specification.

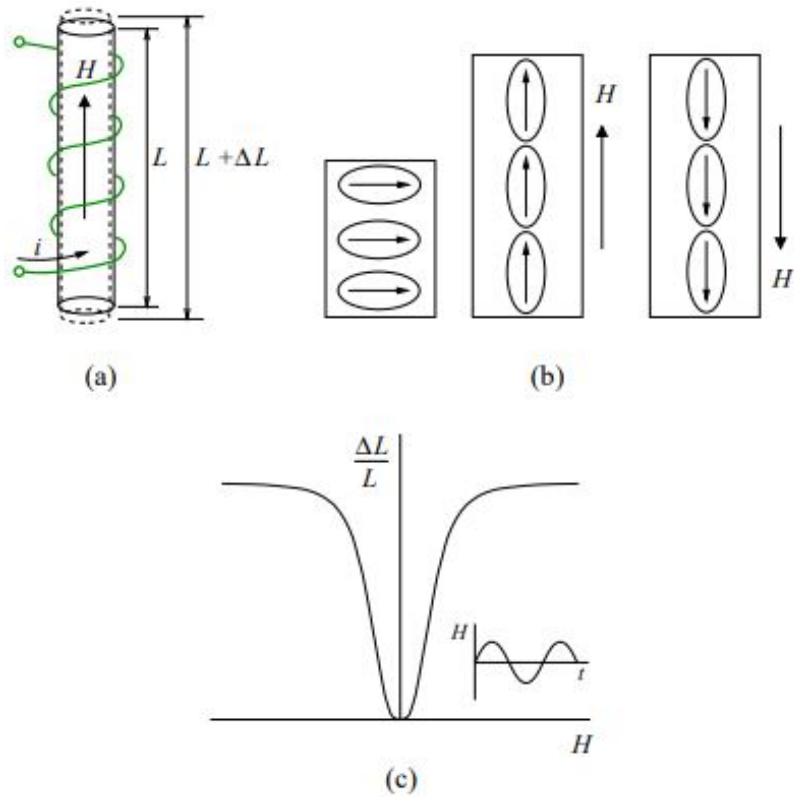


Figure I-28: (a) Magnetisation of magnetostrictive material with magnetic field  $H$  approximately proportional to the current  $i$  that passes through a solenoid (b) the rotation of the domains that change the sample's length (c)  $\Delta L/L$  at different level of magnetic field  $H$  [75]

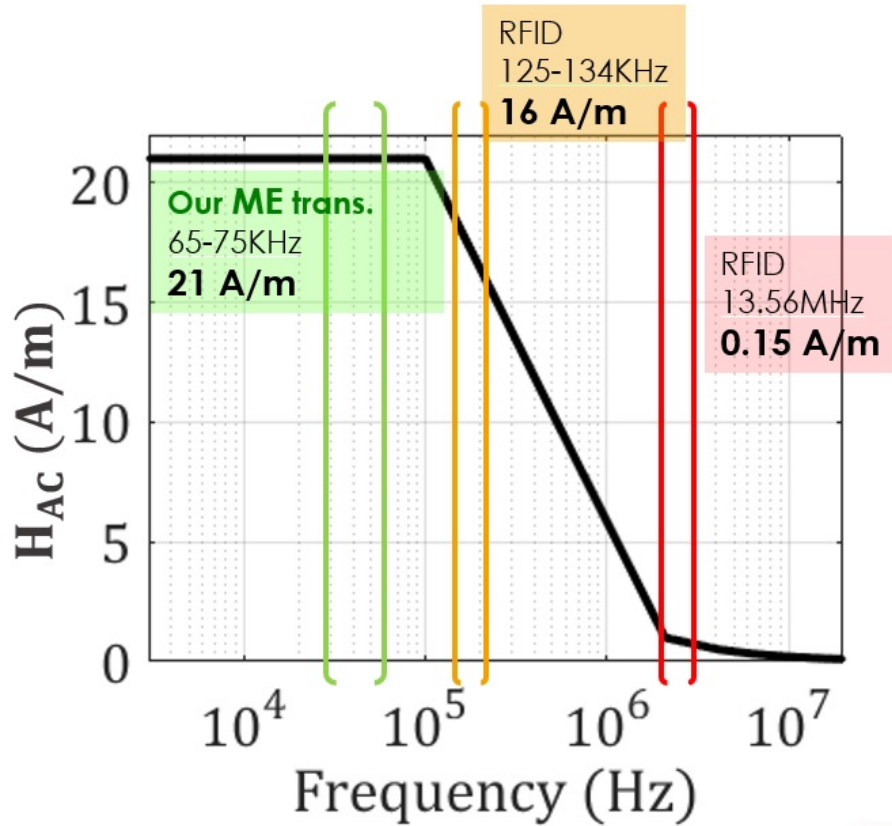


Figure I-29: Magnetic field limitation when using wireless power transfer solutions : RFID (125kHz-134kHz) , RFID(13.56MHz) and our ME transducer (65 – 75kHz). Data taken from the guidelines of the International Commission on Non-Ionizing Radiation Protection (2014)

## 5 Conclusion

In this chapter, different wireless power transfer (WPT) techniques were presented. These techniques were classified based on the energy source. Three categories of sources were presented: electromagnetic (EM), acoustic and light sources. An overview that covers recent WPT application in biomedical domain was carried out. This overview showed that EM-based applications reach a significant level of power compared to existing alternatives. However, the operating frequency of the EM inductive-based solution and their directivity remain drawbacks. On the other hand, applications based on acoustic sources operate at lower frequencies. They can transfer lower amounts of power compared to EM inductive solution but can still achieve a decent power for implanted systems. However this category of WPT applications requires a precise alignment and positioning of the receiver with respect to the emitter, which is unpractical. The third category is based on photovoltaic cells as a power receiver. The dimensions of these cells could reach the  $\mu m$  scale so that it could be used for retinal analysis devices implanted inside the eye or many other implants. The main disadvantage of light source applications is the relatively low power that can be transferred to the load especially when the receiver is implanted deeply in the body.

The design of implantable medical devices is restricted by several limitations (either norms or practical limitations) in order to avoid harming the patient. These restrictions concern the size of the implant, the amplitude and frequency of electromagnetic fields when used as energy sources and the biocompatibility of the device. To match such criteria, a hybrid WPT technique will be introduced. This method uses magnetoelectric (ME) transducers to convert the magnetic field into electrical energy that can power an implants. Chapter II will present the structure and the model of ME transducers. They will be characterized in order to evaluate if they could be good candidates to power medical implants in terms of compromise between transferred power, operating frequency and size of the ME transducer. This characterization is the first required step before a full implementation of power transfer solutions.

# Chapter II

## Characterization of magnetoelectric transducers

### 1 Introduction

After we have explained how magnetoelectric (ME) transducers can be used as a wireless power transfer (WPT) solution, we will show in this chapter how to characterize these ME transducers. First, an overview on existing ME transducers models will be presented. Then we will introduce our new system-level model of the ME transducers. To do that, we will explain the characterization procedure of our ME samples. Therefore, we will present the test bench used to make the measurements and then how to exploit these measurements to characterize the samples in absence and in the presence of AC magnetic fields. At the end of this chapter, we will discuss the results of the characterizations. Also we will talk about the main potential causes of the nonlinearity in the parameter variation when changing the operating point.

### 2 Overview on magnetoelectric transducer modeling

For ME transducers, the energy is converted between three domains: magnetic, mechanical and electrical. A ME transducer model represents the relationships between the variables of these three domains. The constitutive laws are mainly written in

term of the magnetization ( $M$ ), the electric polarisation ( $P$ ), the stress ( $T$ ), the strain ( $S$ ), the electric field ( $E$ ), the magnetic field ( $H$ ), the magnetic induction ( $B$ ) and the electric displacement ( $D$ ). In these laws we find linear and nonlinear coefficients which represent the coupling between the physical domains [79].

A simple model that describes the magnetoelectric (ME) effect is made of a linear relationship between the electric polarisation and the magnetic field ( $H$ ) for the direct effect (II.1) and between the magnetization ( $M$ ) and the electric field ( $E$ ) for the converse effect (II.2) [79].

$$P_i = \alpha_{ij}H_j \quad (\text{II.1})$$

$$M_i = \alpha_{ji}/\mu_0 E_j \quad (\text{II.2})$$

$\alpha_{ij}$  is the susceptibility tensor and  $\mu_0$  is the permeability of the vacuum.  $P_i$  and  $M_i$  are the electric polarization and the magnetization vector respectively.

When the electric and magnetic fields are applied at the same time to ME transducers, the electric susceptibility  $\chi^E$  and the magnetic susceptibility  $\chi^M$  are added in the equations above to represent the influence for the simultaneous application of the magnetic and electric fields.

$$P_i = \alpha_{ij}H_j + \chi_{ij}^E E_j \quad (\text{II.3})$$

$$M_i = \alpha_{ji}/\mu_0 E_j + \chi_{ij}^M H_j \quad (\text{II.4})$$

ME composites are made of magnetostrictive (MS) and piezoelectric (PE) materials. The material-level model of such transducers includes the mechanical variables as the stress and the strain to represent the intermediate phase of the energy conversion. For symmetric layered structures the equation of the model can be written as in (II.5),(II.6) and (II.7).

$$S_i = s_{ij}T_j + d_{ki}E_k + q_{ki}H_k \quad (\text{II.5})$$

$$D_i = d_{ki}T_i + \epsilon_{kn}E_n + \alpha_{kn}H_n \quad (\text{II.6})$$

$$B_i = q_{ki}T_i + \alpha_{kn}E_n + \mu_{kn}H_n \quad (\text{II.7})$$

where  $S_i$  (the strain tensor component);  $D_k$  (the vector component of the electric displacement) and  $B_k$  (the vector component of the magnetic induction) represent the extensive variables. The intensive variables are represented by  $T_j$  (the stress tensor component);  $E_k$  (the vector component of the electric field) and  $H_k$  (the vector component of the magnetic field). The other terms are  $s_{ij}$  (an effective compliance coefficient);  $d_{ki}$  (a piezoelectric coefficient);  $q_{ki}$  (a piezomagnetic coefficient);  $\epsilon_{kn}$  (an effective permittivity);  $\mu_{kn}$  (a permeability coefficient); and  $\alpha_{kn}$  (a ME coefficient) [79]. The aforementioned constitutive equations are the basis for finite element analysis (FEA) widely used to model the ME transducers [80, 81, 82, 83, 84].

An important merit index of material level model is the magnetomechanical coupling factor  $k^2$ . In [85], it is defined as an energy ratio as in the following formula  $k^2 = \frac{g_{ME}^2}{g_{MM}g_{EE}}$ , where  $g_{ME}$  is the coupled magnetoelastic energy,  $g_{MM}$  is the purely magnetic energy and  $g_{EE}$  is the purely elastic energy. We can find it also written in terms of material properties of the composite  $k^2 = \frac{\mu_0 q^2}{S^H \chi^T}$  ( $\mu_0$  is the permeability of free space,  $S^H$  is the mechanical compliance at fixed magnetic field,  $\chi^T$  is the magnetic susceptibility at fixed stress, and  $q$  is the piezomagnetic coupling coefficient) [85].

This coefficient is similar to the global electromechanical coupling coefficient for the piezoelectric transducer defined as  $k^2 = \frac{E_E^S}{E_M^I} = \frac{E_M^S}{E_E^I}$  ( $E_E^S$  is the stored electrical energy,  $E_M^I$  is the input mechanical energy,  $E_M^S$  is stored mechanical energy and  $E_E^I$  is input electrical energy), and to the material coupling coefficient  $k_{ij}^2 = \frac{d_{ij}}{\epsilon_{ii}^X s_{jj}^E}$  where  $d_{ij}$  is the piezoelectric strain coefficient,  $\epsilon_{ii}^X$  is the permittivity at constant stress and  $s_{jj}^E$  is the mechanical compliance of the material under constant electric field conditions [86, 87].

Another significant parameter for ME transducer is the mechanical quality factor

(*Q-factor* or  $Q_m$ ). For a linear system left in open-circuit, it can be determined by the  $Q_m = \frac{f_r}{\Delta f}$  where  $f_r$  is the resonance frequency and  $\Delta f$  is the  $-3dB$  bandwidth observed from the strain spectrum [88, 89]. The Q-factor of laminate ME resonator can be given by  $\frac{1}{Q_m} = \frac{1}{Q_{mech,mag}} + \frac{1-n}{Q_{mech,piezo}}$  where  $Q_{mech,mag}$  and  $Q_{mech,piezo}$  are respectively the effective mechanical Q-factor of the magnetostrictive and the piezoelectric material [90].

Another type of model is the electrical equivalent model. [91, 92, 93, 30]. We can find in the literature some models that bridge the gap, for specific structures, between material coefficients and the system-level coupling  $\alpha$  which represents the coupling between the applied mechanical force  $F$  and the output voltage  $u$  as defined in II.8.

$$F = \alpha u \tag{II.8}$$

Some models even account for nonlinear effects [94]. However, finding the relationship between material-level and system-level model in the general case, and accounting for energy losses with a material-level model remains a complex task. This explains why, in general, system-level parameters are fitted a posteriori based on experimental results.

In comparison to FEM model, the system-level models are easy to use because they involve few parameters to be determined. Moreover, these models are required for electrical design. This is why this thesis develops a single-degree-of-freedom (SDOF) system-level model capable to quantify the nonlinearity in the ME transducer. This was done by studying the variation of the model parameters when the operating conditions change.

### 3 Experimental setup

Before going into detailed characterization, we describe, in this section, the transducers studied during the thesis. The optimization of these transducers has been not performed in this work as it had already been done in a previous work [95][96].

### 3.1 Magnetolectric transducer samples

Our magnetolectric transducers are composed of two materials: a magnetostrictive (MS) and a piezoelectric (PE) layer. The MS material converts the magnetic energy into mechanical energy and the PE material converts the mechanical energy into electrical energy. The material layers are glued together with epoxy glue. This makes both layers vibrate together when the magnetostrictive layer is exposed to alternative magnetic fields (sinusoidal). To enhance the performance of the transducer, the magnetostrictive layer needs to be magnetized by exposing it to a DC magnetic field. The main possible configurations for the magnetization and the polarization of the transducer are shown in Fig. II-1 . Based on previous work [95], one of the most promising configuration is the L-T type which is used for our samples.

Moreover in [96, 95], 45 piezoelectric materials were tested to evaluate their performance when glued to the same magnetostrictive material. This study showed that the combination between the piezoelectric material PZT-5H with the magnetostrictive material (Terfenol-D) transfers the highest power. Note that Terfenol-D is a magnetostrictive material known for its high strain capabilities and therefore it is relatively common in the industry [95], which makes it easy to purchase. The main samples that we used in our study are:

1. "PZT-5H/Terf-D": One magnetostrictive layer of Terfenol-D longitudinally-polarized ( $7mm \times 14mm \times 1mm$ ) glued to a piezoelectric layer of PZT-5H longitudinally-polarized ( $7mm \times 20mm \times 1mm$ ), (see Fig. II-2).
2. "P51/2 $\times$ Terf-D": Two magnetostrictive layers (Terfenol-D longitudinally-polarized) of the same dimensions ( $10mm \times 14mm \times 1mm$ ) glued to a piezoelectric plate of P51 longitudinally-polarized ( $10mm \times 20mm \times 1mm$ ), (see Fig. II-3).

Each side of the piezoelectric layer of the samples is soldered to a wire.

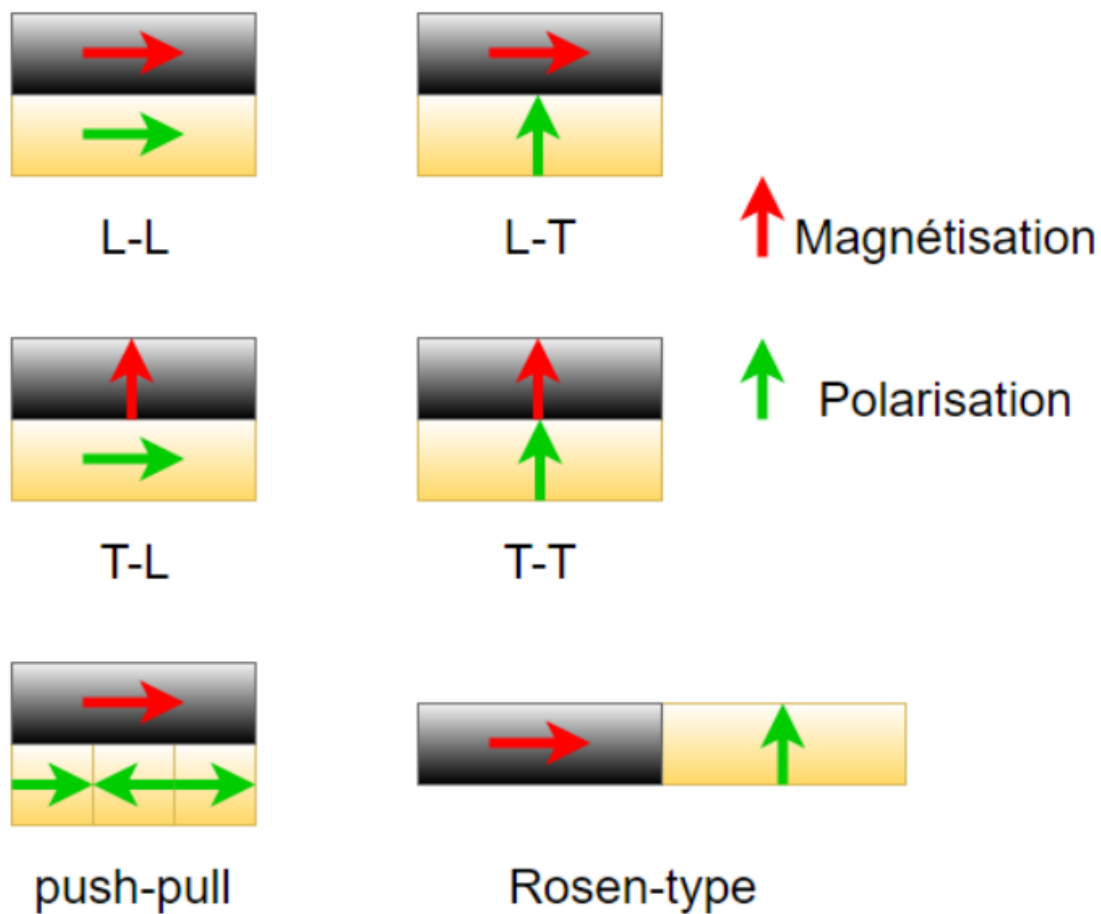


Figure II-1: Main polarization and magnetization configurations of magnetoelastic transducer [97]

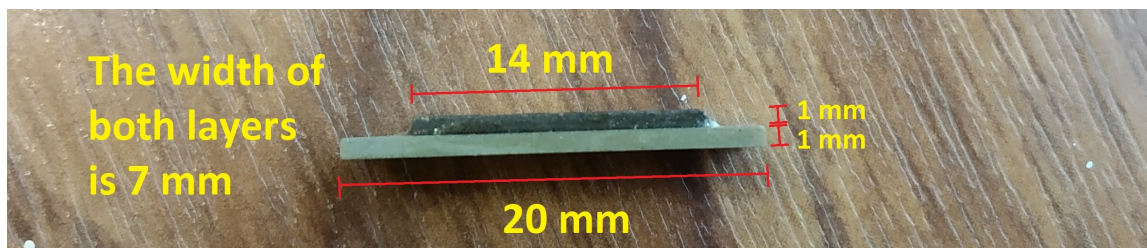


Figure II-2: "P51/2×TerfD" sample: magnetoelastic composite transducer (light green : piezoelectric layer - dark: magnetostrictive layer)

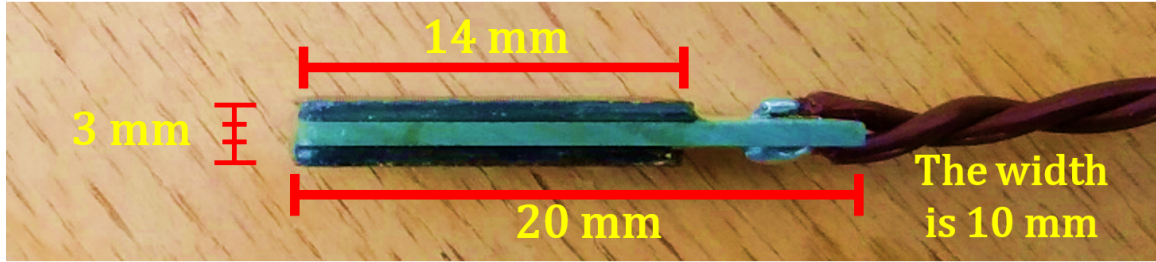


Figure II-3: Magnetolectric sample: a piezoelectric layer (light green) in the middle and two magnetostrictive layers (Dark) each one is glued at one side of the piezoelectric plate.

## 3.2 Characterization procedures

### 3.2.1 Introduction

In this section, we will introduce the validation procedure of our system level model for ME transducers. In this purpose, we will present the different assumptions and experimental study that helped in this process. A discussion on the origin of the losses in the system (excitation coil, ME transducer and load) will be carried out.

### 3.2.2 Characterization in the absence of AC magnetic fields

#### 3.2.2.i Introduction

The aim of the characterization in the absence of AC magnetic field is :

- to characterize the piezoelectric layer and check its linearity,
- to discover the impact of adding magnetostrictive layer to piezoelectric element on a commonly used piezoelectric model [98].

Thus we will start by introducing the piezoelectric model used for characterization. Then we will identify the parameters of the first ME sample (PZT/TerfD) based on admittance measurements. At the end, we will discuss the results and conclude.

#### 3.2.2.ii System-level model

Piezoelectric transducers sometimes exhibit nonlinear behaviors [99], but when they operate at low levels close to one of their resonance frequencies, they are usually

modelled as a coupled single-degree-of-freedom mechanical resonator. This model is introduced in Fig. II-4. It is made of an effective mass  $M$  suspended by a spring of stiffness  $K$ . The factor  $\alpha(N.V^{-1})$  accounts for the bidirectional coupling between the mechanical and the electrical domains. The capacitor  $C_p$  represents the capacitance of the piezoelectric element. The damper  $c$  models the mechanical losses of the system. In the absence of AC magnetic field, we assume that the model of a single-degree electromechanical resonator (Fig. II-4) remains valid when the MS layer is glued to the piezoelectric layer. However, we expect that the MS layer modifies the equivalent coefficients of the model  $M$ ,  $K$ ,  $c$ ,  $\alpha$  and  $C_p$ . The validity of these assumptions is verified further in this chapter. The equations of the model are the following:

$$M \frac{d^2x}{dt^2} + c \frac{dx}{dt} + Kx + \alpha u = 0, \quad (\text{II.9})$$

$$i = \alpha \frac{dx}{dt} - C_p \frac{du}{dt} \quad (\text{II.10})$$

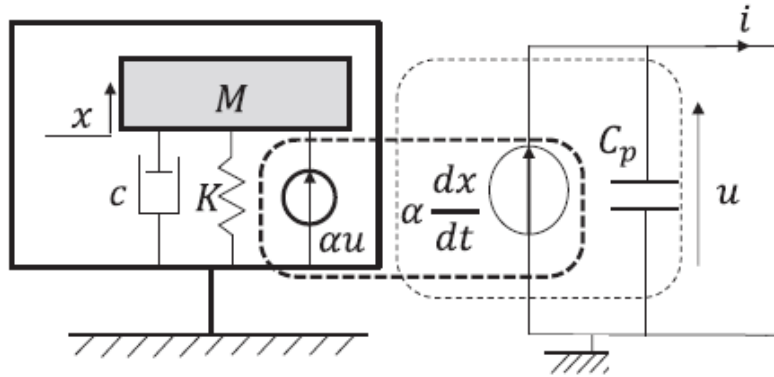


Figure II-4: Electromechanical model of a linear electromechanical resonator (where  $x$  is the displacement)

For the study, we also define the quality factor  $Q = M\omega_0/c$  and the expedient electromechanical coupling coefficient  $k_m^2 = \alpha^2/KC_p$ . The natural (short-circuit) angular frequency is written  $\omega_0 = \sqrt{K/M}$ . Based on this model, a parameter identification was performed.

### 3.2.2.iii Admittance measurements

Admittance measurements were performed to identify the parameters of the model in

absence of AC magnetic field. The measurements were made with a Hewlett Packard 4194A Impedance Analyzer. The transducer used in this first characterization is the first sample "PZT-5H/Terfenol-D" (denoted also "P-T sample") shown in Fig. II-2. The results were compared to the transducer without the MS layer. We denote as "P sample" the PE transducer alone (PZT-5H layer). Admittance measurements were taken with the sample holder shown in Fig. II-5. This sample holder is designed to reduce perturbations related to the contact with the sample when taking measurements. Admittance curves measured on the P sample and P-T sample are reported in Fig. II-6. The frequency interval starts at  $50kHz$  and ends at  $90kHz$  with a step of  $100Hz$  (401 point for each actuation level). For both samples, the linear SDOF model fits very well with the measurements, for each actuation level. With visual observation, we can see that the curves for P sample are superimposed. This means that the model parameters do not change when the applied voltages increase. This is a well-known result for piezoelectric materials at low actuation level. On the other side, the P-T sample admittance response is voltage dependent. This proves that the MS layer has a significant impact on the model parameters. This impact is to be determined by further analyses, in the upcoming sections of this chapter.



Figure II-5: The sample holder ((a): picture, (b): schematic) "M" denotes a mechanical contact and "E" an electrical contact. "PE" plate in green and "MS" plate in black

### 3.2.2.iv Parameter identification

The damping coefficient  $c$ , the capacitance  $C_p$ , the mass  $M$ , the coupling coefficient

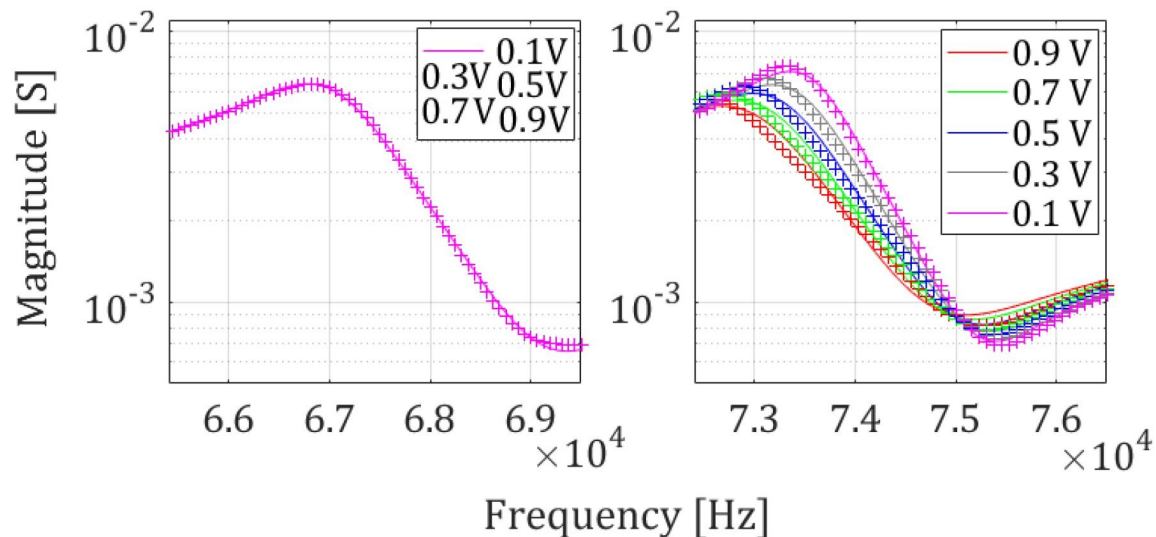


Figure II-6: Measurements (cross +) performed in the absence of a AC magnetic field and corresponding fits (solid lines). Admittance of the “P sample” (left) and “P-T sample”(right) for several voltage levels. In the case of P sample all the curves at different actuation levels are superposed. Thus we show only one curve.

$\alpha$  and the stiffness  $K$  in the equations (II.9) and (II.10) are all present in three normalized parameters: the quality factor  $Q$ , the coupling coefficient  $k_m^2$ , the natural frequency  $f_0 = \omega_0/2\pi$ . Therefore we reduced the number of parameters to determine to four ( $Q$ ,  $k_m^2$ ,  $f_0$  and the piezoelectric element capacitor  $C_p$ ).

Table II.1: Normalized variables of the piezoelectric model

<i>Variable</i>	<i>Quantity (unit)</i>	<i>Normalized variable</i>
$\omega$	Vibration angular frequency ( $rad.s^{-1}$ )	$\Omega = \frac{\omega}{\omega_0}$
$x$	Displacement of the resonator ( $m$ )	$X = \frac{xM\omega_0^2}{\beta i_1}$
$i$	Output current ( $A$ )	$I = \frac{ik_m^2 M\omega_0}{\alpha\beta i_1}$
$u$	Output voltage ( $V$ )	$U = \frac{u\alpha}{\beta i_1}$

$$\ddot{X} + \frac{1}{Q}\dot{X} + X + U = 0 \quad (II.11)$$

$$I = k_m^2 \dot{X} - \dot{U} \quad (II.12)$$

To identify the parameters of the P and P-T samples we fit the impedance measurements illustrated in Fig. II-6 using the empirical output impedance formula of

the model (II.13). This formula is derived from the normalized equations (II.11) and (II.12). The normalized variables are given in Table II.1. The fitting procedure is based on a nonlinear least-squares fitting algorithm (Matlab script based with lsqnonlin function).

$$Y = \frac{\frac{\Omega^2}{Q} + j(\Omega^3 + \Omega k_m^2 - \Omega)}{\Omega^2 - 1 - \frac{j\Omega}{Q}} \quad (\text{II.13})$$

### 3.2.2.v Results and Discussion

We report, in Fig. II-7, the parameters obtained at several actuation voltages. As one can expect from a linear model, all the parameters estimated on the P-sample are constant. On the contrary, significant variations of the estimated parameters are observed on the P-T sample ("PZT-5H/TerfD"). The addition of a MS layer strongly impacts the electromechanical behavior. The results clearly show that, on the P-T sample, all the parameters are function of the voltage level. In particular, the quality factor of the P-T sample decreases by around 50% between 0.1V and 1V. One of the most important characteristic when trying to optimize a power transfer system is the figure-of-merit (FOM)  $k_m^2 Q$  (see Fig. II-8) [100]. Due to the sharp decrease of the quality factor, the FOM of the P-T composite also decreases strongly (-28%).

### 3.2.2.vi Conclusion

In this characterization we have verified the linearity of the piezoelectric element used in our ME samples. Then, we estimated the overall impact of the addition of a magnetostrictive layer, as well as the nonlinearity introduced by this addition. Contrary to the piezoelectric element alone, we have shown that the coupling coefficient and the quality factor of the ME composite strongly depend on the voltage. In particular, the quality factor of our sample decreases sharply with the voltage level (more than 50% between 0.1V and 1V) which has a strong consequence of the figure-of-merit  $k_m^2 Q$ . In the next section we will tackle the characterization of the ME transducer in presence of AC magnetic field.

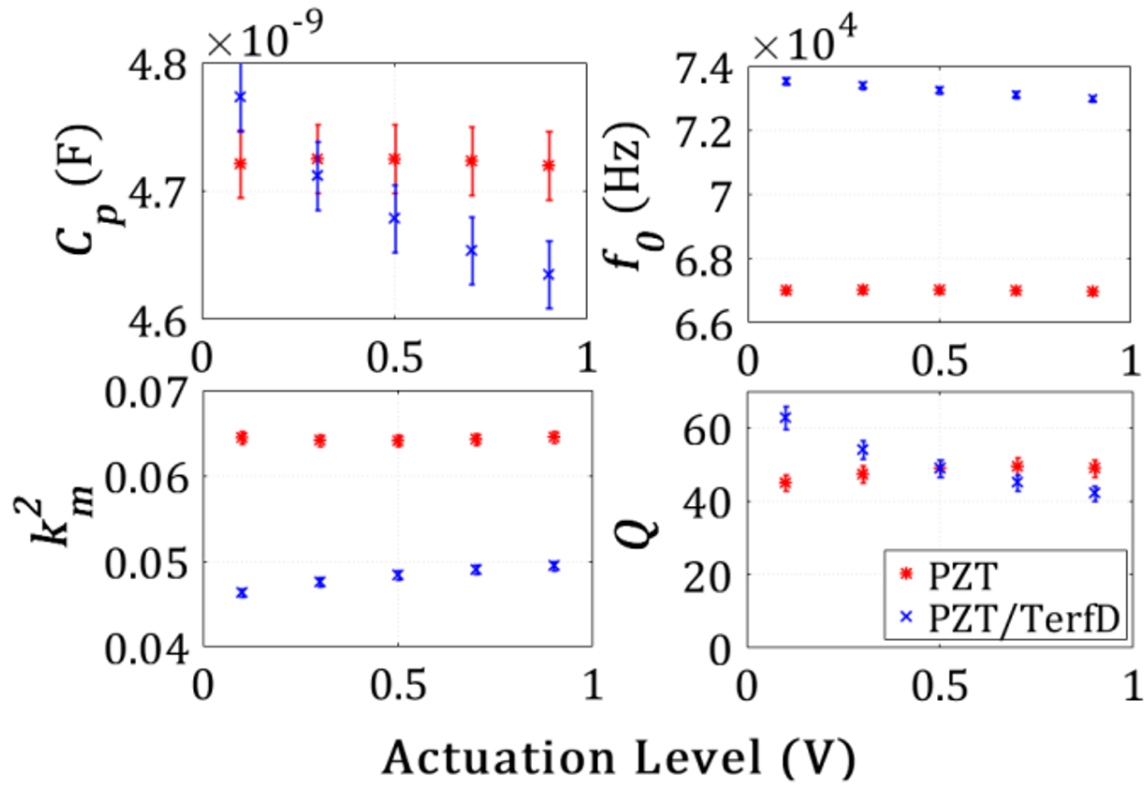


Figure II-7: Parameters estimated from the electromechanical model

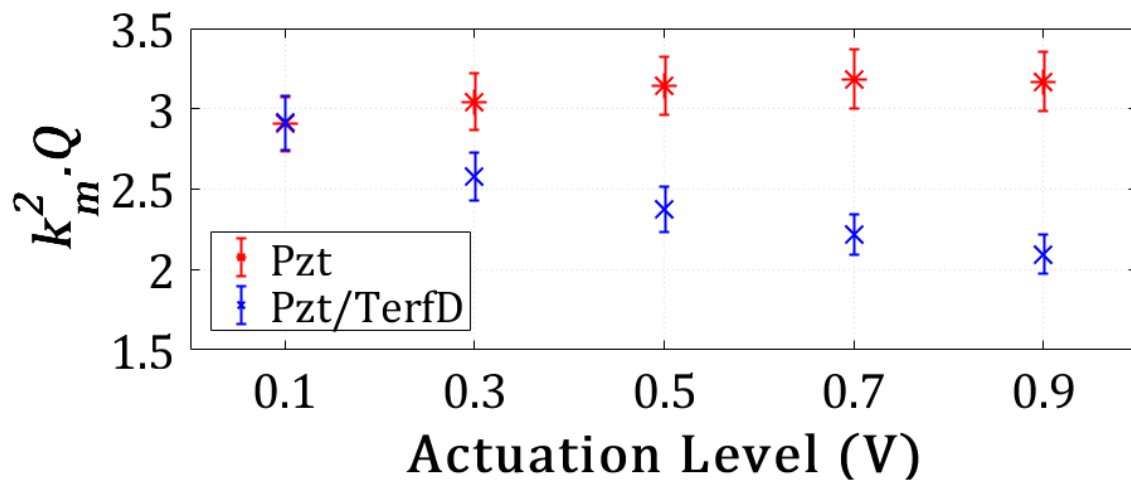


Figure II-8: Evolution of the FOM.

### 3.2.3 Characterization in the presence of AC magnetic fields

#### 3.2.3.i Introduction

This section is dedicated to present the characterization procedure of the magneto-electric (ME) transducers in the presence of AC magnetic fields. We will present first the experimental setup built for this characterization. First, we performed measurements at controlled input voltage of the excitation coil and then at controlled output current. In this section, we will give the result of the parameter identification of both measurement sets. At the end of this part, a discussion on the origin of the losses in the system (excitation coil, ME transducer and load) will be conducted.

#### 3.2.3.ii Characterization setup

In the setup, the sample is placed in a sample holder exposed to an DC magnetic field (approximately  $H_{DC} = 40 \times 10^3 (A/m)$ ) by a permanent magnet arrangement and AC magnetic field by an excitation coil. The DC magnetic field is chosen in order to maximize the open-circuit voltage when the transducer is actuated by an AC magnetic field at resonance. The output of the Agilent 33220A wave function generator is applied to the coil. Voltage measurements are done with a R&S®RTB2004 oscilloscope. We designed a feedback loop based on a PID controller in the setup to control voltages in the system. We can either control the voltage delivered across the actuator or the voltage across the piezoelectric generator. A picture and a schematic of the setup are given in Fig. II-9 and Fig. II-10. The ME sample "P51/2×Terf-D" for this characterization is shown in Fig. II-3. It is a composite of one piezoelectric layer (material:P-51) and two magnetostrictive layers (material:Terfenol-D).

#### 3.2.3.iii First assumption: predominant magnetic losses

##### a Introduction

This section explores a first assumption where the magnetic losses are predominant in the system in the presence of AC magnetic field. We assume here that they are the origin of the observed variations in the response of the ME transducer when the

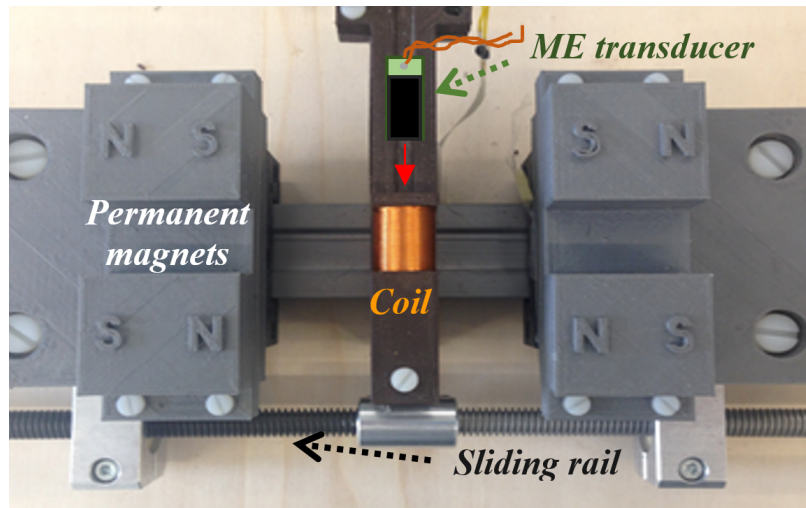


Figure II-9: Experimental setup test bench consisting of: an excitation coil (100 turns, 18mm of diameter, 0.1mm $\varnothing$ wire), a sliding rail to adjust the permanent magnet position and to reach the optimal static magnetic fields  $40 \times 10^3(A/m)$ . The ME transducer is inside the sample holder surrounded by the coil.

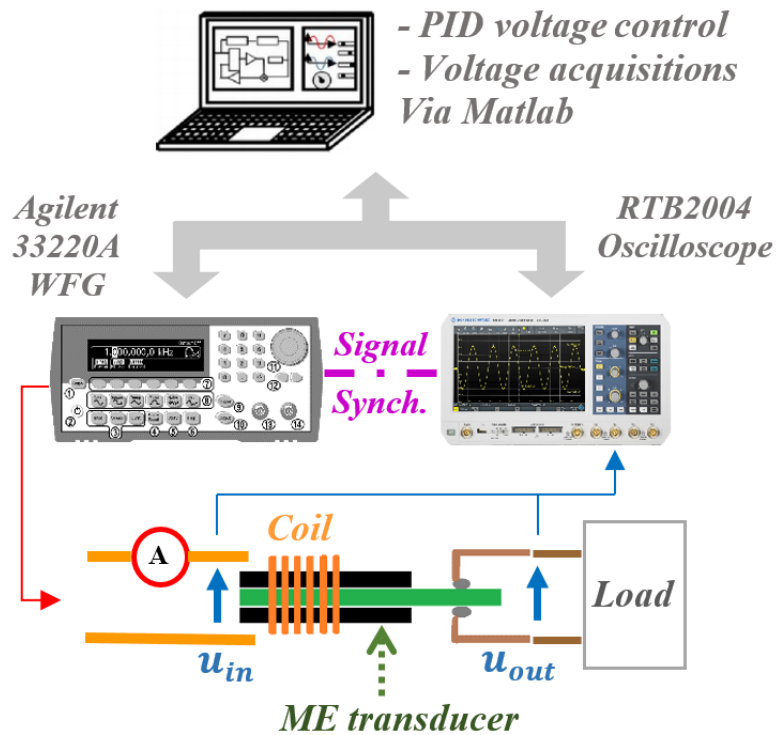


Figure II-10: Schematic of the experimental setup.

actuation levels increase. To separate the effect of magnetic field from other effects we performed sets of measurements at fixed AC magnetic field amplitudes. Since we cannot have access to the value of the AC magnetic field inside the sample with precision, we regulate the input current applied to the emitting coil while performing a frequency sweep. To take into consideration the effect of the coil in the system, we proposed a new ME model. Based on the measurements, we identify the parameters of the ME transducer sample "P51/2×Terf-D". In the end of the analysis, we conclude about the validity of this assumption.

### **b The magnetoelectric transducer model**

The ME transducer is modeled by two coupling stages [101]: the magneto-mechanical coupling (MMC) between magnetic and mechanical domains and the electro-mechanical coupling (EMC) between mechanical and electrical domains. Fig. II-11 describes the overall system. The transducer is placed under a static (DC) magnetic field (not represented in the schematic) and a variable magnetic field at angular frequency  $\omega$  generated by a coil of inductance  $l$  through which a current  $i_{in} = i_1 \sin \omega t$  flows. The resistance of the excitation coil is written  $r$ . The piezoelectric element of capacitance  $C_p$  is connected to a resistive load  $r_{load}$ . The output (piezoelectric) current is written  $i$  and the piezoelectric voltage is  $u$ .

The mechanical model is made of an effective mass  $M$  of motion  $x$  with respect to the base, suspended by a nonlinear spring of stiffness  $K$ . The factor  $\beta$  (N/A) accounts for the bidirectional MMC. The factor  $\alpha$  (N/V) accounts for the bidirectional EMC. The damper  $c$  models the mechanical losses of the system. The resulting equations governing the system are thus (II.14), (II.15) and (II.16).

$$M \frac{d^2 x}{dt^2} + c \frac{dx}{dt} + Kx + \alpha u - \beta i_{in} = 0 \quad (\text{II.14})$$

$$\frac{u}{r_{load}} = \alpha \frac{dx}{dt} - C_p \frac{du}{dt} \quad (\text{II.15})$$

$$u_{in} = l \frac{di_{in}}{dt} + \beta \frac{dx}{dt} + r i_{in} \quad (\text{II.16})$$

To highlight the main parameters of interest for system-level characterization, the variables are normalized as described in Table II.2, where  $\omega_0 = \sqrt{(K/M)}$  is the natural (short-circuit) angular frequency. This leads to (II.17), (II.18) and (II.19) where all normalized parameters are given in Table II.3. One can notice that our normalization procedure brings out the well-known expedient electromechanical coupling coefficient  $k_m^2$  (characteristic of the piezoelectric element [102]) but also a magneto-electrical coupling coefficient  $B_m$ . Considering the analogy with piezoelectric theory, we will call  $B_m$  the expedient magneto-electrical coupling coefficient.

$$\ddot{X} + \frac{1}{Q} \dot{X} + X + U - B_m I_{in} = 0 \quad (\text{II.17})$$

$$\frac{U}{R_{load}} = k_m^2 \dot{X} - \dot{U} \quad (\text{II.18})$$

$$U_{in} = L \dot{I}_{in} + B_m k_m^2 \dot{X} + R I_{in} \quad (\text{II.19})$$

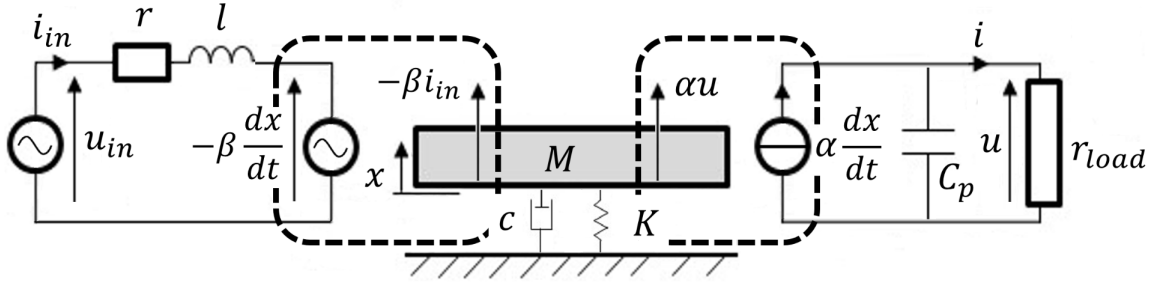


Figure II-11: Magneto-electromechanical model of the ME transducer connected to a resistive load [103]

In the following section, we will show that, based on relevant experiments, the parameters of this model can be estimated.

### c Measurement acquisition

For this characterization, we use the feedback loop of the setup to maintain a constant excitation. Therefore we controlled the input voltage  $u_{in}$  of the coil to regulate the

Table II.2: Notations

<b><i>Variable</i></b>	<b><i>Quantity (unit)</i></b>	<b><i>Normalized variable</i></b>
$\omega$	Vibration angular frequency ( $rad.s^{-1}$ )	$\Omega = \frac{\omega}{\omega_0}$
$x$	Displacement of the resonator ( $m$ )	$X = \frac{xM\omega_0^2}{\beta i_0}$
$i_{in}$	Input current ( $A$ )	$I_{in} = \frac{i_{in}k_m^2 M\omega_0}{\alpha\beta i_0}$
$i$	Output current ( $A$ )	$I = \frac{ik_m^2 M\omega_0}{\alpha\beta i_0}$
$u_{in}$	Input voltage ( $V$ )	$U_{in} = \frac{u_{in}\alpha}{\beta i_0}$
$u$	Output voltage ( $V$ )	$U = \frac{u\alpha}{\beta i_0}$

Table II.3: System-level parameters

<b><i>Coefficients</i></b>	<b><i>Quantity</i></b>	<b><i>Expression</i></b>
$\omega_0$	Natural (short-circuit) angular frequency	$\omega_0 = \sqrt{\frac{K}{M}}$
$Q$	Quality factor	$Q = \frac{M\omega_0}{c}$
$k_m^2$	Expedient electromechanical coupling coefficient	$k_m^2 = \frac{c^2}{KC_p}$
$B_m$	Expedient magnetoelctrical coupling coefficient	$B_m = \frac{\beta C_p \omega_0}{\alpha}$
$L$	Normalized excitation coil inductance	$L = lC_p\omega_0^2$
$R_{load}$	Normalized resistive load	$R_{load} = r_{load}C_p\omega_0$
$R$	Normalized excitation coil resistance	$R = rC_p\omega_0$

input current  $i_{in}$  at a constant value along the frequency sweeps and for all resistive loads. This corresponds to a situation where the AC magnetic field sent to the transducer is constant. We perform two series of measurements: one for the open-circuit case and one for a resistive load  $r_{load}$  of  $1.2k\Omega$ , corresponding to  $R_{load} = 1$  which is the impedance matching condition for the piezoelectric element at resonance. [104].

#### d Experimental results

Based on voltage measurements, we fit  $u/u_{in}$ . We assume that  $f_0 = 1/2\pi\sqrt{K/M}$  is not influenced by the value of the resistive load. The result of the fit is reported in Fig. II-12. “OC” and “LD” refer to the open-circuit and to the resistive-load case respectively. Fig. II-12 shows that the model fits the measurements.

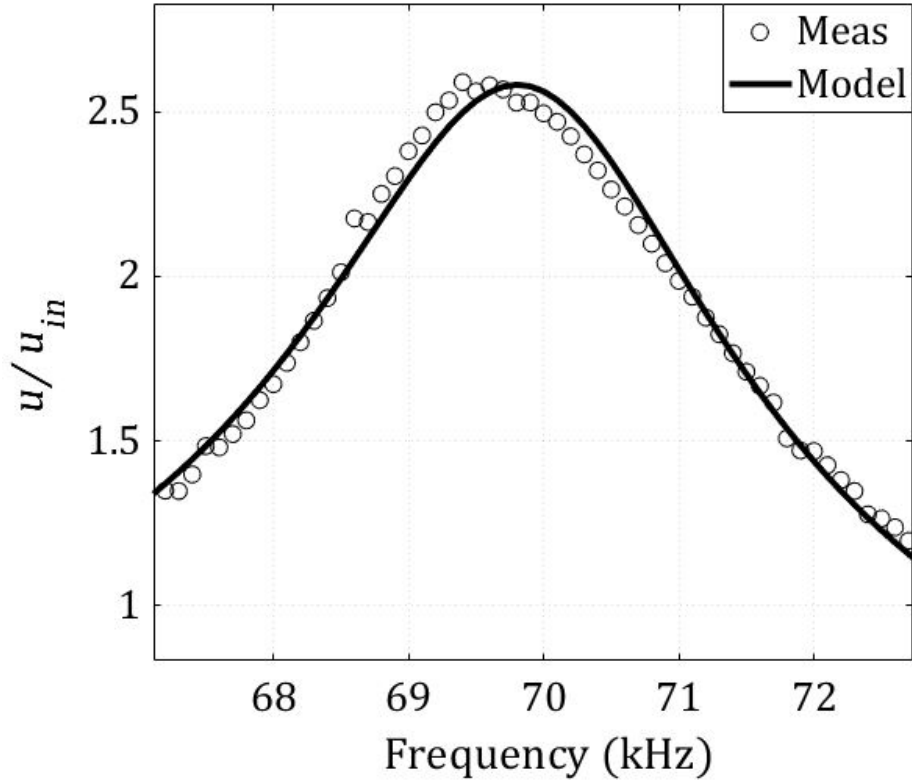


Figure II-12: The fitting results of  $u/u_{in}$  (input voltage level  $3V_{rms}$  open circuit case)

The quality factor  $Q$  and the natural frequency  $f_0$  with and without load are estimated for different levels of input voltage (corresponding to different levels of AC magnetic field). The results are reported in Fig. II-13. The results shows that the

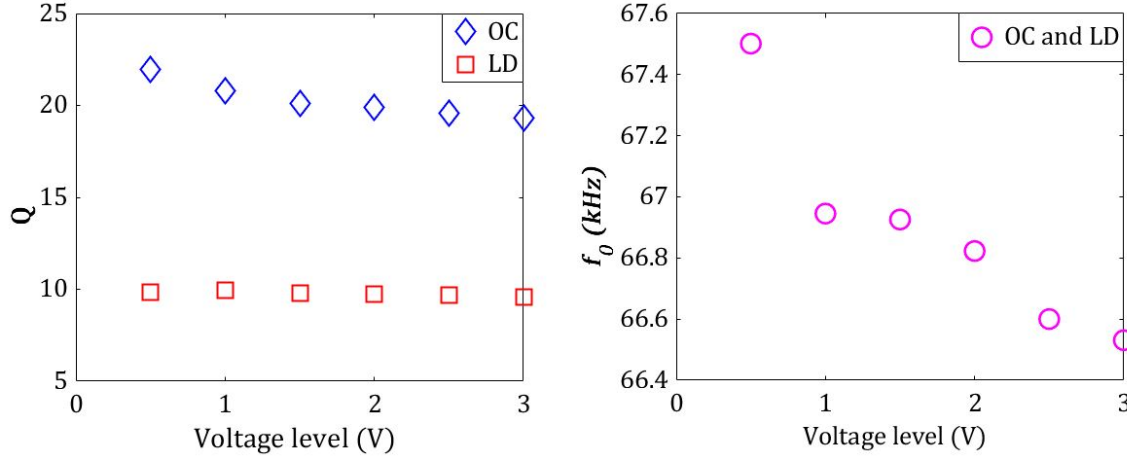


Figure II-13: Estimated parameters of the ME model for open-circuit (OC) and with  $1.2k\Omega$  resistive load (LD) case (left: quality factor  $Q$  and right: the natural frequency  $f_0$ )

quality factor  $Q$  is 2 times lower in the presence of a resistive load than in open circuit ( $Q$  drops almost from 22 to 10). This cannot be attributed to the losses into the load resistance because these losses are modeled separately ( $Q$  as defined in our system is distinct from the current term  $u/r_{load}$ ). At resonance, the transferred power is proportional to  $Q$  so that estimating the power based on open-circuit characterization would lead to an overestimation of the power by more than 70 times compared to the actual power. As an illustration of this last statement, we plot in Fig. II-14 the measured transferred power along with its theoretical fit and, on the other hand, the power that would be expected from open-circuit characterization. We observe an overestimation for two input voltages. When we connect the transducer to a resistive load of  $1.2k\Omega$ , the transferred power at the resonance are  $7.7mW$  and  $0.22mW$  with input voltage of  $3V_{rms}$  ( $\approx 128(A/m)$ ) and  $0.5V_{rms}$  ( $\approx 21(A/m)$ ) respectively.

### e Discussion and observations

We observe that the quality factor in the presence of output current is significantly lower than in open-circuit. Such nonlinear damping is not expected to take place in a piezoelectric material alone at such small actuation levels. This would tend to prove that the magnetostrictive layer and the magnetic coupling increases the energy

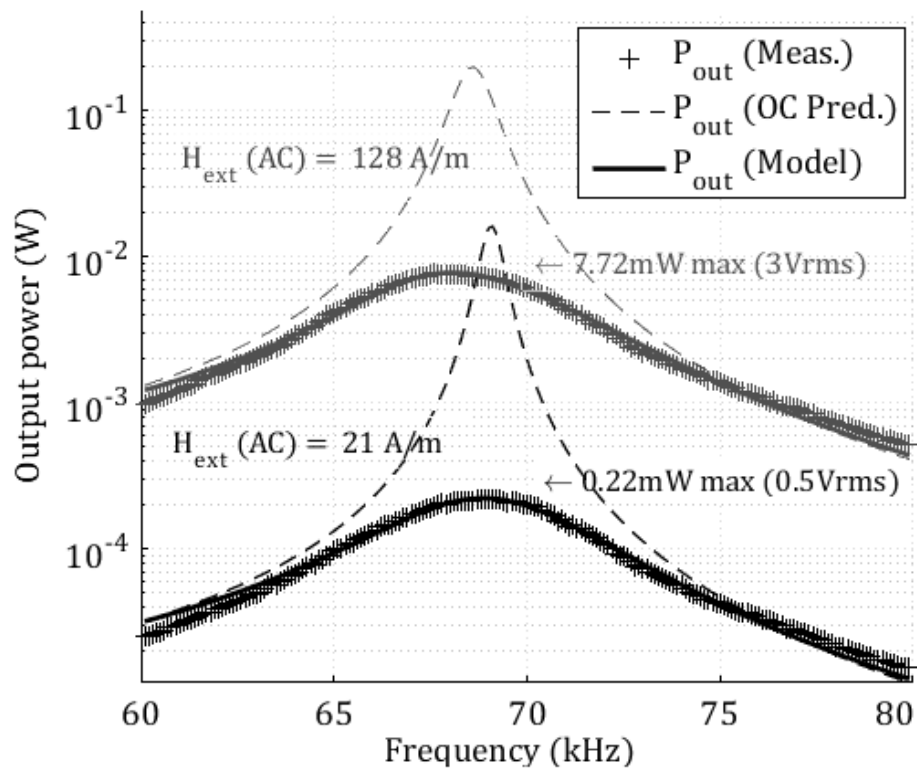


Figure II-14: Measured transferred power (plus sign points + ), estimated transferred power based on open-circuit (OC) characterization (dashed line - - ), theoretical fit of the transferred power based on with load (LD) characterization (continuous line). Two input voltage levels are presented ( $0.5V_{rms}$  and  $3V_{rms}$ ).

losses. Whatever the origin of such losses, it is important to notice that estimating the transferred power based on open-circuit characterization would lead to a wrong prediction, as stated previously. The transferred power at resonance is known to be proportional to the system quality factor [105] explaining the overestimation of the output power observed in Fig. II-14.

### **f Conclusion: failure of the first assumption**

From the parameter evolution depicted in Fig. II-13, one may assume that the quality factor  $Q$  is :

- Almost independent of the input voltage  $u_{in}$  applied to the coil for a fixed load.
- Dependent on the load and thus on the output voltage  $u_{out}$  and/or the output current  $i$ .

However, the output voltage  $u_{out}$  is not constant along a sweep when we regulate the input voltage  $u_{in}$ . This can be observed on the transfer function  $4 \frac{u_{out}}{u_{in}}$  at fixed input voltage in Fig. II-12 ( $u_{out}$  at the boundaries ( $67kHz$  and  $73kHz$ ) is about the half of its value at the resonance (near to  $69.5kHz$ )).

Knowing this, we can conclude that the aforementioned assumptions are contradictory. Consequently, we cannot consider that this characterization at controlled input voltage is a valid method to identify the model parameters. This leads to the failure of the first assumption. This is already a very significant result. Indeed, most existing works characterize their wireless power transfer technologies while regulating the actuation (whether the voltage or the current). If, in some cases, this approach may be valid, our study proves that it must be used with precautions. These results remain valid even if we consider a nonlinear stiffness ( $K(x) = K_0 + K_2x^2$ ) in the equation of the model [106].

### 3.2.3.iv Second assumption: predominant mechanical losses

#### a Introduction

In the previous section, we demonstrated that the characterization at a regulated AC magnetic field amplitude could not explain the evolution in the response of the ME transducer when the load is changed. In this section, we will check if losses are mainly due to mechanical vibrations. First we present an improved version of the magneto-electromechanical model and the assumptions that we made on the model parameters. As for the previous assumption, we need to separate the mechanical effects from other effects. Hence, using the feedback loop of the setup, we will propose a method to control the movement of the transducer indirectly. For that purpose, we make measurements at a regulated displacement amplitude of the transducer equivalent mass. Based on these measurements we will characterize the ME transducer. Finally we discuss the results validate this second assumption.

#### b Characterization setup

As described in the theoretical part, the damping coefficient  $c(x, \frac{dx}{dt})$  and the stiffness  $K(x)$  are expected to change when the amplitude  $x_m$  of the displacement  $x$  varies. Hence, controlling the amplitude of the displacement would ensure that the system parameters do not vary significantly during each sweep. Unfortunately, controlling the mechanical motion without dedicated instruments like a laser vibrometer is complex. However, the motion amplitude  $x_m$  is proportional to the amplitude  $i_1$  of the output current as long as the load resistance is constant (see (II.20) obtained from (II.29)). In (II.20),  $\omega_m = \pi(f_{max} + f_{min})$  is the center of the frequency interval. Equation (II.20) assumes that the resonator is characterized on a narrow frequency range due to its high Q-factor. Hence, controlling the amplitude  $i_1$  of the output current and the load  $r_{load}$  guarantees that the amplitude of the mechanical motion remains constant during each sweep. We performed frequency sweeps from  $f_{min} = 65kHz$  to  $f_{max} = 72kHz$

for several loads around  $r_{load} = 600\Omega$  close to the optimal resistance.

$$x_m = \frac{i_1}{\alpha\omega} \sqrt{1 + \frac{\omega^2}{\omega_0^2} R_{load}^2} \simeq \frac{i_1}{\alpha\omega_m} \sqrt{1 + \frac{\omega_m^2}{\omega_0^2} R_{load}^2} \quad (\text{II.20})$$

### c Presumption based on admittance measurements

Referring to the evolution of the parameters in the absence of AC magnetic field we assumed that the piezoelectric capacitance  $C_p$  and coupling coefficient  $k_m^2$  are constant. To validate this presumption, we performed admittance measurements (with Zurich Instruments MFIA Impedance Analyzer) under  $H_{DC}$  in the absence of AC magnetic field. An example is given in Fig. II-15 where  $f = \frac{\omega}{2\pi}$ .

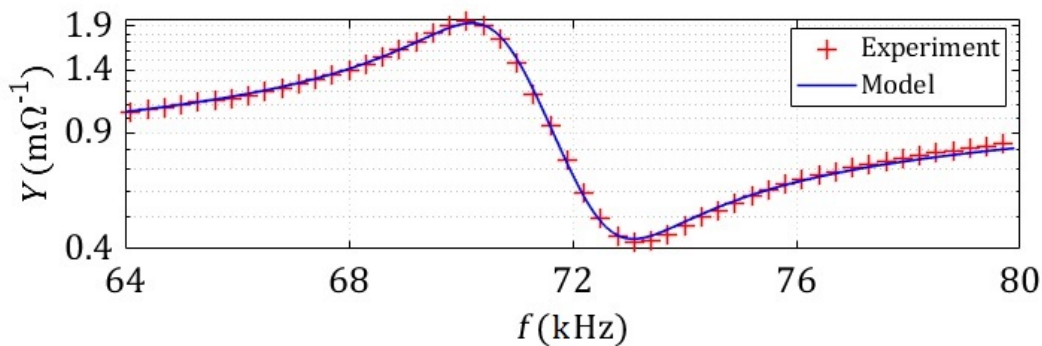


Figure II-15: Admittance measurements ( $u_1 = 1.5V$ ).

The sweep duration is 20s and the sweep step is 100Hz. Measurements at other amplitudes from 0.1V to 3V have shown that neither  $C_p$  nor  $k_m^2$  vary significantly. We found that  $C_p \simeq 2nF$  and  $k_m^2 \simeq 5.48 \times 10^{-2}$ .

### d Linear model with variable parameters

The ME transducer is placed under a static magnetic field (generated by a permanent magnet). A variable magnetic field at angular frequency  $\omega$  is generated by a current  $i_{in} = i_0 \sin \omega t$  flowing through a coil. As the dimensions of the ME transducer are very small compared to the wavelength of the AC magnetic field, the latter is uniform inside the sample. The SDOF model of the magnetolectric transducer (ME) under such conditions is given in Fig. II-16. In this model,  $C_p$  is the capacitance of the piezoelectric element. The leak resistance  $r_p$ , in parallel with  $C_p$ , accounts for the

electrical losses inside the piezoelectric layer. The piezoelectric output current is written  $i$  and the piezoelectric voltage  $u$ . The mechanical model is made of an effective mass  $M$  of motion  $x$  with respect to the base, suspended by a spring of stiffness  $K(x)$ . A previous study has proven that the system exhibits a nonlinear stiffness [106]. For that reason, we assume that the stiffness is given by (II.21).

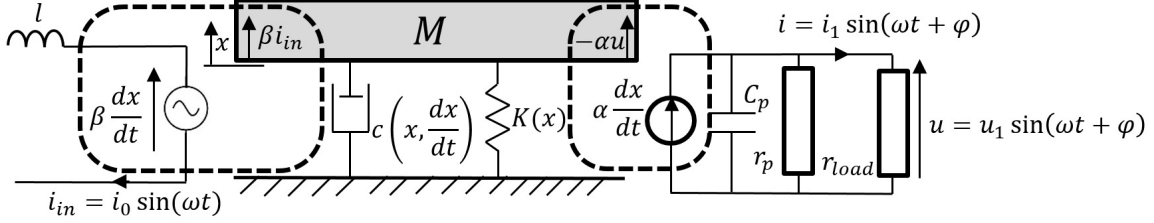


Figure II-16: Magneto-electromechanical model of the ME transducer.

$$K(x) = K_{lin} + K_{NL}(x) \quad (\text{II.21})$$

With this definition,  $K_{lin}$  corresponds to the stiffness of the resonator for a very low vibration amplitude and  $K_{NL}(x)$  to the displacement-dependent stiffness of the system. The natural angular (short-circuit) frequency is  $\omega_0(x) = \sqrt{K(x)/M}$  and the natural frequency is  $f_0(x) = \omega_0(x)/2\pi$ . We also define the natural angular frequency  $\omega_{0lin} = \sqrt{K_{lin}/M}$  in linear regime. The factor  $\beta$  (N/A) accounts for the bidirectional magneto-mechanical coupling (MMC) and the factor  $\alpha$  (N/V) for the bidirectional electromechanical coupling (EMC). One may expect small variations of  $\alpha$  with the motion  $x$  [107, 108, 109] but our experimental results (see section e and f) will allow us to neglect the variations of  $\alpha$ . The mechanical and magnetic losses in the circuit are modeled by a nonlinear damper (II.22).

$$c(x, dx/dt) = c_{lin} + c_{NL}(x, dx/dt) \quad (\text{II.22})$$

With this definition,  $c_{lin}$  accounts for the damping of the resonator at a very low vibration amplitude and  $c_{NL}(x, dx/dt)$  for all the potential sources of nonlinear damping.

Many physical phenomena may be the source of nonlinear damping [107, 110].

Among them, one may expect structural damping when the elastic material is imperfect and/or due to slip or friction or numerous other physical phenomena [111]. Based on these assumptions, the motion of mass  $M$ , is governed by (II.23) and (II.24).

$$M \frac{d^2 x}{dt^2} + c(x, \frac{dx}{dt}) \frac{dx}{dt} + K(x)x + \alpha u - \beta i_{in} = 0, \quad (\text{II.23})$$

$$\frac{u}{r_{load}} = \alpha \frac{dx}{dt} - C_p \frac{du}{dt} - \frac{u}{r_p} \quad (\text{II.24})$$

The corresponding quality factor is defined by (II.25) where  $Q_{lin}$  and  $Q_{NL}(x, \frac{dx}{dt})$  are given in (II.26) and (II.27).

$$\frac{1}{Q(x, \frac{dx}{dt})} = \frac{1}{Q_{lin}} + \frac{1}{Q_{NL}(x, \frac{dx}{dt})} \quad (\text{II.25})$$

$$Q_{lin} = \frac{M\omega_{0lin}}{c_{lin}} \quad (\text{II.26})$$

$$Q_{NL}(x, \frac{dx}{dt}) = \frac{M\omega_0(x)}{c_{NL}(x, \frac{dx}{dt})} \quad (\text{II.27})$$

Unfortunately the aforementioned parameters are dependent on the fabrication process of the sample and the motion amplitude. Hence, no analytical expression is readily available. Therefore we choose a grey-box model for our system.

In this model, the piezoelectric layer is assumed to be leakless ( $r_p = \infty$ ). Since the parameters depend on the mechanical motion, the system is linearized in the vicinity of an amplitude  $x_0$ . In such case, the behavior of the ME system becomes (II.28) and (II.29). The linearized quality factor then verifies (II.30).

$$M \frac{d^2 x}{dt^2} + c \left( x_0, \frac{dx}{dt}(x_0) \right) \frac{dx}{dt} + K(x_0)x + \alpha u - \beta i_{in} = 0, \quad (\text{II.28})$$

$$\frac{u}{r_{load}} = \alpha \frac{dx}{dt} - C_p \frac{du}{dt} \quad (\text{II.29})$$

$$\frac{1}{Q(x_0)} = \frac{1}{Q_{lin}} + \frac{1}{Q_{NL}(x_0, \frac{dx}{dt}(x_0))} \quad (\text{II.30})$$

Based on the notations given in Table II.2, we obtain (II.31) and (II.32), which bring out the expedient electromechanical coupling coefficient  $k_m^2$  [112, 113] given in (II.33) and an expedient magnetoelectric coupling coefficient  $B_m$  (II.34). In (II.32),  $R_{load}$  stands for the normalized resistance  $R_{load} = r_{load}C_p\omega_0(X_0)$ .

$$\ddot{X} + \frac{\dot{X}}{Q(X_0)} + X + U - B_m I_{in} = 0, \quad (\text{II.31})$$

$$\frac{U}{R_{load}} = k_m^2 \dot{X} - \dot{U}, \quad (\text{II.32})$$

$$k_m^2(X_0) = \frac{\alpha^2}{K(X_0)C_p} \quad (\text{II.33})$$

$$B_m(X_0) = \frac{\beta C_p \omega_0(X_0)}{\alpha} \quad (\text{II.34})$$

Table II.4: Notations

<i>Variable</i>	<i>Quantity (unit)</i>	<i>Normalized variable</i>
$\omega$	Vibration angular frequency ( $rad.s^{-1}$ )	$\Omega = \frac{\omega}{\omega_0}$
$x$	Displacement of the resonator ( $m$ )	$X = \frac{xM\omega_0^2}{\beta i_0}$
$i_{in}$	Input current ( $A$ )	$I_{in} = \frac{i_{in}k_m^2 M\omega_0}{\alpha\beta i_0}$
$i$	Output current ( $A$ )	$I = \frac{ik_m^2 M\omega_0}{\alpha\beta i_0}$
$u$	Output voltage ( $V$ )	$U = \frac{u\alpha}{\beta i_0}$

### e Experimental results

In the series of measurements, the amplitude of the output current is regulated at different levels from  $0.28mA$  to  $2.55mA$ . For this range of  $i_{out}$ , the amplitude  $i_0$  of the input current  $i_{in}$  varies from  $2mA$  to  $90mA$ . We perform the measurements for 8 loads between  $270\Omega$  and  $2200\Omega$ . Parameters are identified from a nonlinear least-squares fitting procedure on the transfer function  $u_1/i_0$  which can be obtained

from (II.31) and (II.32) expressed in the frequency domain either numerically or analytically. The corresponding analytical formula is given in (II.35) where  $d_1(\Omega) = 2k_m^2 QR_{load} + 1 + R_{load}^2 \Omega^2$  and  $d_2(\Omega) = \Omega^2 - 2 + R_{load}^2(1 + k_m^2 - \Omega^2)^2$ .

Fig. II-17 illustrates three examples at  $i_1 = 0.28mA$ ,  $i_1 = 1.41mA$  and  $i_1 = 2.55mA$ . The corresponding estimated parameters are reported in Fig. II-18.

$$\frac{u_1}{i_0}(\Omega) = \frac{B_m k_m^2 R_{load} \Omega}{\omega_0 C_p \sqrt{\frac{\Omega^2}{Q^2} d_1(\Omega) + 1 + \Omega^2 d_2(\Omega)}} \quad (\text{II.35})$$

For each load, we observe that:

- the quality factor  $Q$  and the natural frequency  $f_0$  decrease,
- the expedient magnetoelectric coefficient  $B_m$  slightly rises

when the amplitude  $i_1$  of the piezoelectric current  $i$  increases.

## f Further analysis and validation

To analyze further the results given in section e, we quantify the evolution of the parameters with the output current. To that purpose, we start by fitting an empirical law on the parameters  $Q(i_1)$ ,  $f_0(i_1)$  and  $B_m(i_1)$ . The corresponding laws are given in (II.36), (II.37) and (II.38) in which  $i_{min} = 0.28mA$  is the minimum amplitude of the output current set in our experiments. Since each  $r_{load}$  leads to a different mechanical motion amplitude (see (II.20)), the coefficients of the empirical law must be adjusted depending on the resistive load. The values of the parameters in the empirical laws for the resistances tested in this setup are given in Tables II.5, II.6 and II.7. The evolution of  $f_0^2$  corresponds to a spring softening effect, preponderant at low amplitude, and a slight hardening effect balancing the softening effect as the motion amplitude increases. The evolution of  $B_m$  shows that the magnetostrictive coefficient  $\beta$  is proportional to the output current. Last, (II.36) combined with (II.20) shows that the energy losses rise significantly with the amplitude of the mechanical motion. These results provide the quality factor  $Q_{lin}$  (II.39), the natural frequency  $f_{0lin}$  (II.40) and the magnetoelectric coefficient  $B_{m_{lin}}$  (II.41) in linear regime (at low motion amplitude). The corresponding standard deviation  $\sigma$  is also indicated.

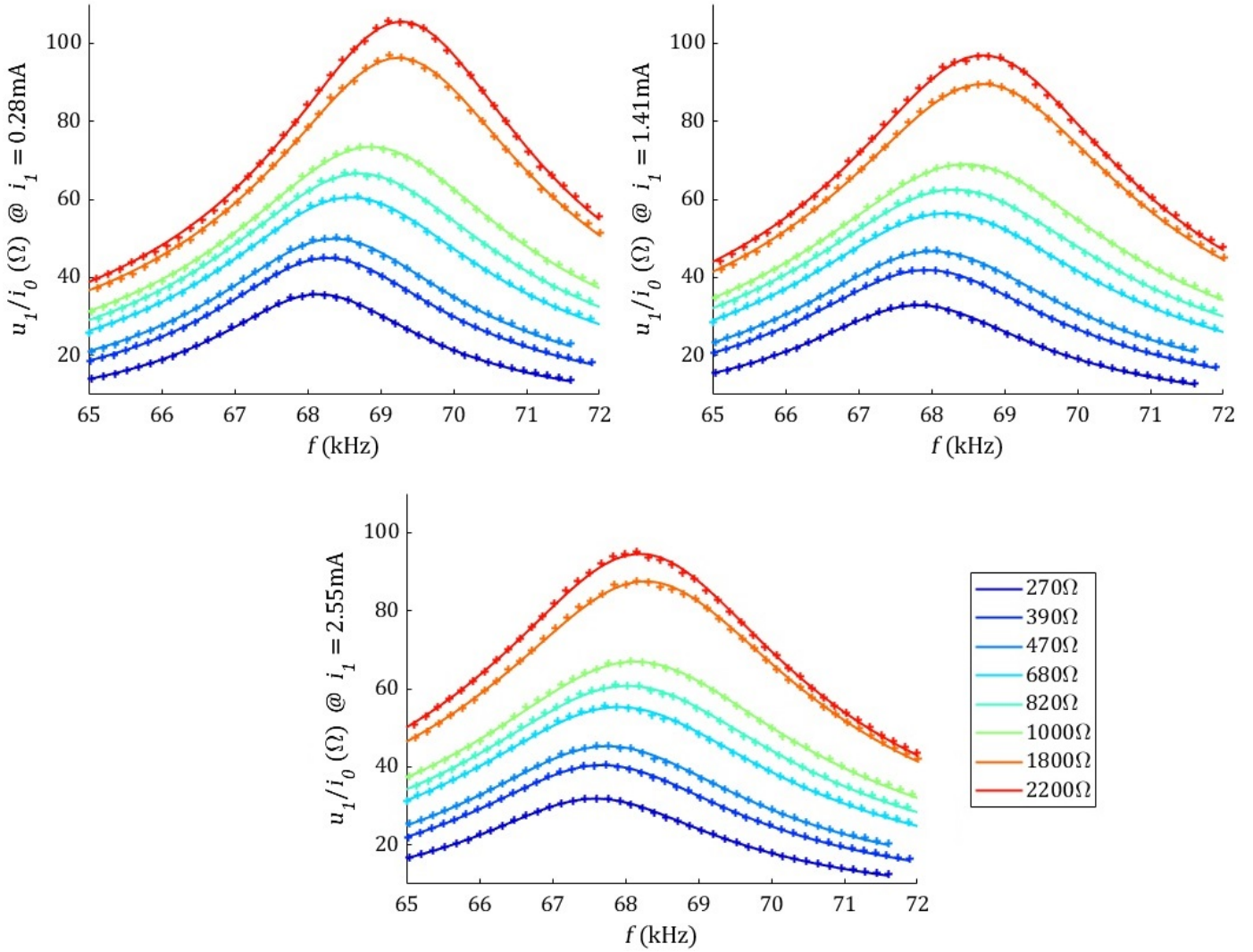


Figure II-17: Model identification: experimental frequency responses  $u_1/i_0$  for a regulated amplitude of the output current (left:  $i_1 = 0.28\text{mA}$ , middle:  $i_1 = 1.41\text{mA}$ , right:  $i_1 = 2.55\text{mA}$ ). Crosses: measurements. Solid lines: model. From blue to black:  $r_{load} = 270\Omega$  to  $r_{load} = 2200\Omega$ .

$$\frac{1}{Q(i_1)} = \frac{1}{Q_{lin}} + p_1 \left( \frac{i_1}{i_{min}} \right)^q, \quad (\text{II.36})$$

$$f_0^2(i_1) = f_{0lin}^2 \left[ 1 - \nu_1 \frac{i_1}{i_{min}} + \nu_2 \left( \frac{i_1}{i_{min}} \right)^2 \right], \quad (\text{II.37})$$

$$B_m(i_1) = B_{mlin} \left[ 1 + b_1 \frac{i_1}{i_{min}} \right], \quad (\text{II.38})$$

Table II.5: Empirical law of  $Q$

$r_{load}(\Omega)$	$Q_{lin}$	$q (\times 10^{-1})$	$p_1 (\times 10^{-2})$
270	47.9	3.484	0.692
390	47.8	3.526	0.695
470	49.0	3.598	0.702
680	56.1	3.012	0.929
820	53.4	3.282	0.820
1000	57.9	3.152	0.883
1800	50.8	4.166	0.620
2200	46.4	4.879	0.502

Table II.6: Empirical law of  $f_0^2$

$r_{load}(\Omega)$	$f_{0lin}$ (kHz)	$\nu_1 (\times 10^{-3})$	$\nu_2 (\times 10^{-4})$
270	68.15	2.84	0.83
390	68.19	2.90	0.77
470	68.21	3.04	0.82
680	68.22	3.15	0.74
820	68.22	3.55	1.10
1000	68.20	3.51	0.93
1800	68.08	4.40	1.08
2200	68.00	4.47	0.65

Table II.7: Empirical law of  $B_m$

$r_{load}(\Omega)$	$B_{m_{lin}} (\times 10^{-2})$	$b_1 (\times 10^{-3})$
270	9.86	7.96
390	9.83	7.06
470	9.69	7.60
680	9.57	7.66
820	9.52	7.23
1000	9.39	6.85
1800	9.05	8.63
2200	9.02	9.14

$$Q_{lin} = \frac{2\pi M f_{0_{lin}}}{c_{lin}} = 51.2 \quad (\sigma = 4.2), \quad (\text{II.39})$$

$$f_{0_{lin}} = \frac{1}{2\pi} \sqrt{\frac{K_{lin}}{M}} = 68160 Hz \quad (\sigma = 81 Hz), \quad (\text{II.40})$$

$$B_{m_{lin}} = 9.5 \times 10^{-2} \quad (\sigma = 3.2 \times 10^{-3}), \quad (\text{II.41})$$

Ultimate validation of our model requires to check its predictivity. To that purpose, we perform another series of measurements where the amplitude  $i_0$  of the input current is regulated, instead of the amplitude  $i_1$  of the output current. If our model is accurate (i.e. if the parameters mainly depend on the output), we should be able to predict the evolution of  $i_1$  during the frequency sweeps at  $i_0$  constant by taking into account the parameter variations identified in Fig. II-18.

We report in Fig. II-19, the predicted evolution of the output current at three regulated amplitudes  $i_0 = 11.3mA$ ,  $i_0 = 19.8mA$  and  $i_0 = 35.4mA$  for several loads, along with the experimental measurements. The agreement between the experiments and the predicted behavior is very good. If the parameters did mostly depend on the AC magnetic field (i.e. on the input current), the predicted behavior would be far from the observations. Despite the good correspondence, we observe a small deviation between the predictions and the measurements which implies that the parameters may also slightly depend on the input current.

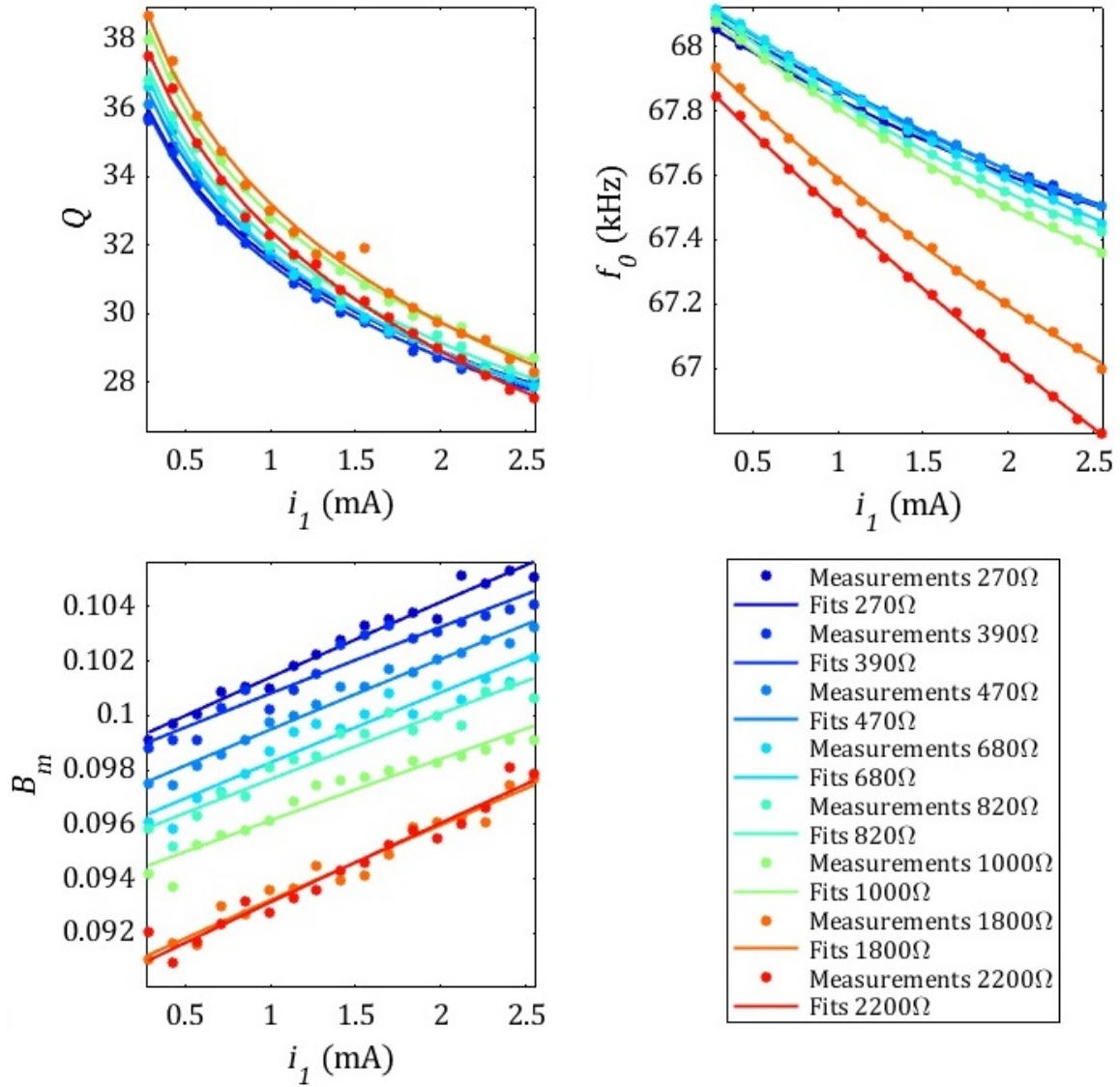


Figure II-18: System parameters as a function of the output current  $i_1$  for several resistive loads. Upper left: quality factor  $Q$ , Upper right: natural frequency  $f_0$ , lower left: expedient magnetolectric coefficient  $B_m$  (Dots : Measurements. Solid lines: Fits).

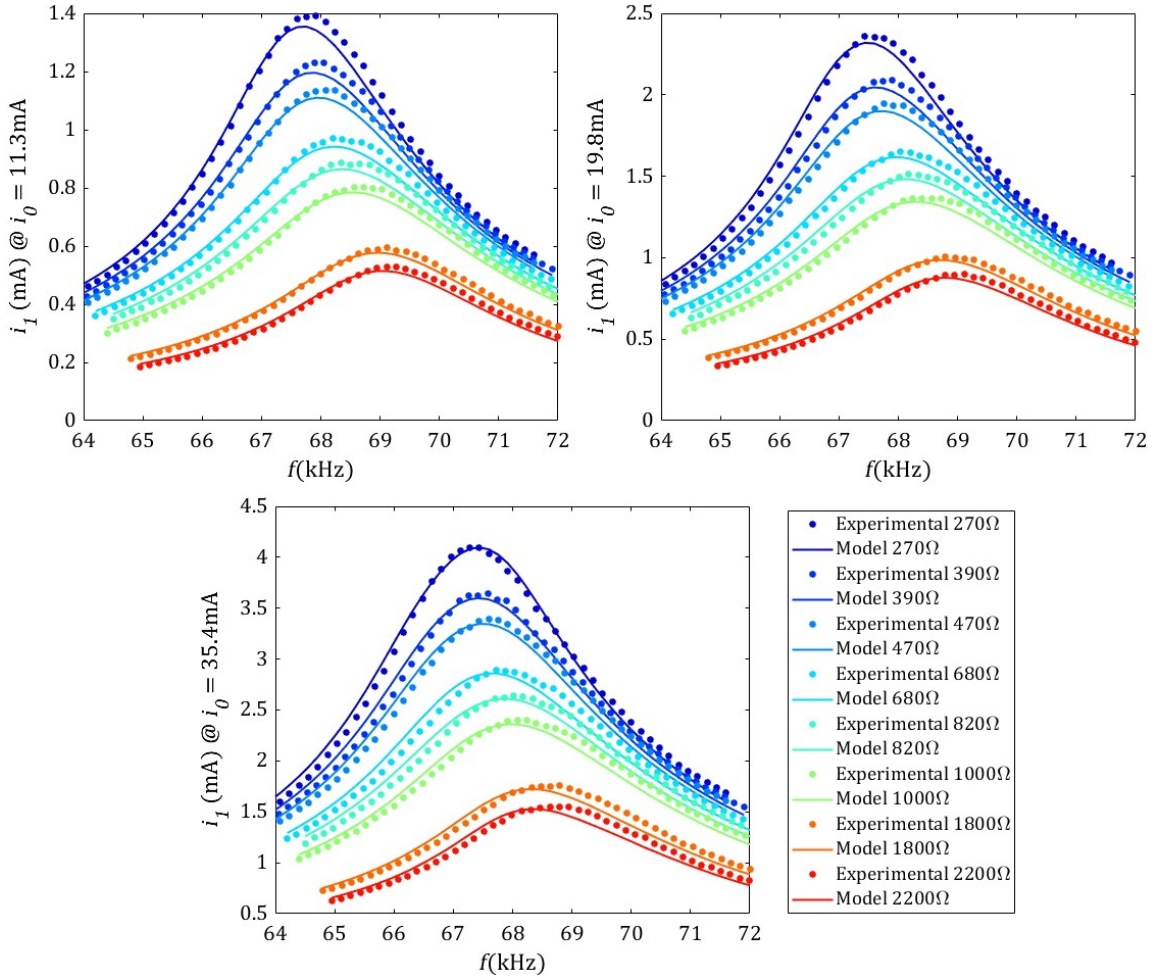


Figure II-19: Model validation: experimental frequency responses  $i_1$  for a regulated amplitude of the input current (left:  $i_0 = 11.3mA$ , middle:  $i_0 = 19.8mA$ , right:  $i_0 = 35.4mA$ ). Dots: measurements. Solid lines: model. From blue to black:  $r_{load} = 270\Omega$  to  $r_{load} = 2200\Omega$ .

Now that the model has been validated, interesting conclusions can be drawn from our characterization. A first set of conclusions relates to the main physical origin of performance degradation in our device. The second set deals with the consequences of the system nonlinear behavior on the circuit design and on the transferable power. These discussions are the subjects of section g.

### **g Discussion about the physical origin of power losses**

Specific physical phenomena lie in the evolution of the estimated quality factor. In terms of energy losses, the overall system can be decomposed into a resistive part in the RLC-series equivalent model of the resonator and a parallel resistance  $r_p$ . In our model, the quality factor  $Q$  accounts for all the energy losses (magnetic and/or mechanical) except the electrical losses related to leakage currents.

#### **Electrical losses**

In section d, we modelled the electrical losses with the leak resistance  $r_p$  and stated that it is often neglected in theoretical as well as in experimental studies. In our case, we measured the parallel resistance  $r_p$  and it is so large that we are not able to determine its exact value. Our measurements suggest that it is superior to  $2M\Omega$ , which is larger than  $r_{load}$  by 3 orders of magnitude. For this reason, we can safely assume that the electrical losses are negligible and are not the cause of the observed variations of the parameters. In particular, they cannot explain the decrease of the quality factor when the current increases.

#### **Magnetic losses**

The origin of magnetic losses is mainly related to eddy current in the magnetostrictive layer [114, 115]. Eddy currents are expected to increase when the AC magnetic fields becomes larger. In section e, we have proven that  $Q$  may reasonably be assumed to be independent of  $i_0$  and dependent mainly on  $i_1$ . Hence, in our setup, the magnetic losses may be neglected compared to the (nonlinear) mechanical losses.

#### **Mechanical losses**

Since other origins have been eliminated, the preponderant energy losses in our system are mechanical. As stated in section d, a damping coefficient that is dependent

on the displacement  $x$  and/or the velocity  $dx/dt$  [108, 110] is typically related to mechanical dissipation. Measurements performed on the PE element before gluing to the magnetostrictive layers have shown that the PE layer alone behaves linearly. Significant discrepancies appear after gluing the PE layer to the magnetostrictive layers. For this reason, we suspect the losses to come from dissipation inside the glue and/or inside the magnetostrictive layers.

## 4 Conclusion

This chapter is dedicated to introduce the experimental study and the validation procedure of our magnetoelectric transducer model. At the beginning, an overview on existing magnetoelectric transducer models have been conducted. Then, the experimental part has been presented. In this part, two characterisation of ME transducers were realized. The first characterisation of our samples was made in absence of AC magnetic field. The objective of this characterisation is to find the impact of gluing the magnetostrictive (MS) layer with the piezoelectric (PE) layer of a composite ME transducer. Therefore, we used an existing piezoelectric system-level model to characterize a PE plate before and after gluing to it a MS plate. For that purpose, different impedance measurements have been realized at different actuation level (voltage). The results showed that the model parameters of the PE plate after gluing the MS layer depend on the voltage. In particular, the quality factor of the composite decreases sharply with the voltage level (more than 50% between 0.1V and 1V) which has a strong consequence of the figure-of-merit  $k_m^2 Q$ . This was not expected to take place in case of PE transducer.

The second characterization have been realised in presence of AC magnetic field. For that purpose, a new experimental setup has been installed. Based on an analytical model with two levels of coupling, we highlighted the parameters of interest at system level, which are mainly the natural frequency, the quality factor, the expedient magnetoelectrical coupling coefficient  $B_m$  and the expedient piezoelectric coupling coefficient  $k_m^2$ . With this new setup, two measurement sets were performed. In the

first set, the measurements have been realized at controlled voltage of the excitation coil. The model parameters were estimated based on open-circuit measurements combined with measurements on an optimal resistive load. In presence of a load (and thus of output current), the observed quality factor is significantly lower than in open circuit ( $-50\%$ ). The power transferred for an AC magnetic field of  $3V_{rms}$  is  $7.72mW$ . Power predictions based on open-circuit measurements would overestimate the transferred power at the resonance more than 70 times the real power. Hence, for wireless power transfer applications, the estimation of the power should take into account the presence of the load. For the second set, the measurement have been performed at regulated output current. Based on these measurements, we proposed a methodology to identify the model parameters. It was noticed that, for the current levels achieved in our setup, the most consistent result is obtained when regulating the output current. This is explained by the dependency between the parameters of interest and the mechanical motion. In particular, the evolution of the quality factor proves that the main origin of energy losses in our device lies in a phenomenon that is dependent on the mechanical vibration amplitude.



# Chapter III

## Power management of magnetolectric transducer

### 1 Introduction

The magneto-electromechanical model in Fig. II-16 introduced in the previous chapter can be represented as a lumped-parameter model as shown in Fig. III-1. The mechan-

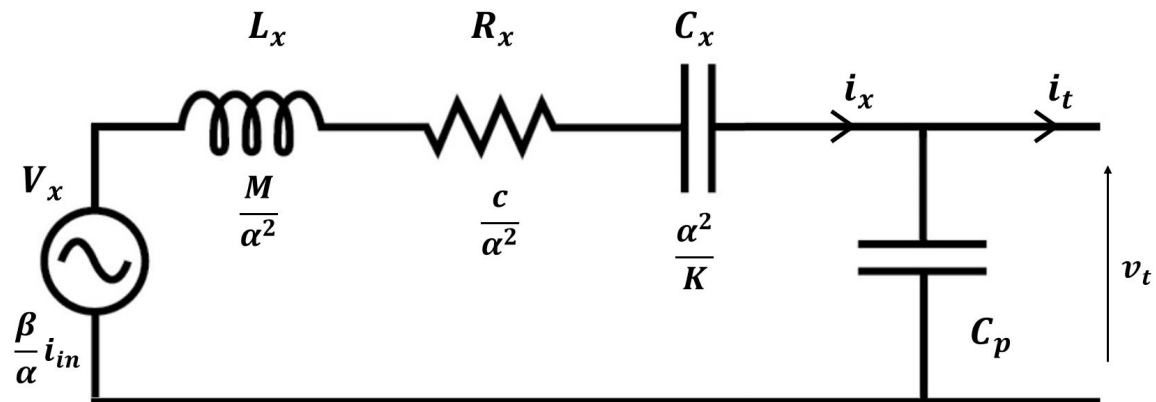


Figure III-1: Equivalent electric circuit of ME transducer

ical part of the transducer can be represented as an RLC circuit connected in series with a voltage source. The voltage source  $V_S = \frac{\beta}{\alpha} i_{in}$  models the mechanical force generated by the magnetostrictive layer when a magnetic field is applied. The RLC circuit models a mechanical resonator of second order with an inductor  $L_x = M/\alpha^2$ , a

resistance  $R_x = c/\alpha^2$ , a capacitance  $C_x = \alpha^2/K$ . The current  $i_x$  models the velocity of the mass. All these parameters with the subscript  $x$  represent mechanical quantities and cannot be measured directly. They can be determined indirectly by making measurements on the electrical terminals of the transducer. The normalized system-level parameters highlighted in the previous chapter are  $k_m^2 = \alpha^2/KC_p$ ,  $Q = M\omega_0/c$  and  $\omega_0 = \sqrt{K/M}$ . The components of the RLC circuit can be expressed as a function of these normalized parameters  $L_x = 1/\omega_0^2 k_m^2 C_p$ ,  $C_x = k_m^2 C_p$  and  $R_x = 1/\omega_0 C_p k_m^2 Q$ . The electrical behavior of the transducer is modeled by the capacitance  $C_p$  connected to the RLC circuit and in parallel with the load.  $v_t$  is the voltage at the terminals of the piezoelectric element. The capacitance  $C_p$  is sometimes considered a parasitic element because it may "short circuit" the mechanical resonator ( $V_x$ ,  $C_x$ ,  $L_x$ , and  $R_x$ ). If the operating point frequency is equal to the short-circuit frequency  $f_0 = 1/(2\pi\sqrt{C_x L_x})$ , the capacitance  $C_x$  compensates for the inductor  $L_x$ . As shown in Fig. III-2, the optimal power transfer will occur when:

- the capacitance  $C_p$  is compensated by connecting in parallel an inductor  $L_p$  so that  $L_p\omega = 1/(C_p\omega)$
- the resistive load is equal to  $R_x$ .

Moreover, if the impedance  $Z_{C_p} = 1/(\omega C_p)$  of the capacitance  $C_p$  is very high compared to the resistance  $R_x$ , only the second condition is required, in other words, when the ratio  $Z_{C_p}/R_x$  is high. One can notice that  $Z_{C_p}/R_x = k_m^2 Q$ . This is a reason why  $k_m^2 Q$  is considered a figure-of-merit for PE transducers. A generator having larger  $k_m^2 Q$  product will be considered as exhibiting a "stronger coupling" compared to a lower  $k_m^2 Q$  product. To conclude, at the frequency  $f = f_0$ , when the figure of merit  $k_m^2 Q$  is large, we can transfer the maximum of the power with a circuit exhibiting a resistive behavior ( $r_{load} = R_x$ ) and without the need to compensate for the capacitance of the piezoelectric element  $C_p$ . On the other hand, when  $k_m^2 Q$  is low, the compensation of the capacitance  $C_p$  is needed to maximize the performance of the transducer. This explains why the architectures able to achieve impedance matching are often more complex for lower coupling (e.g. synchronized-switching architectures)

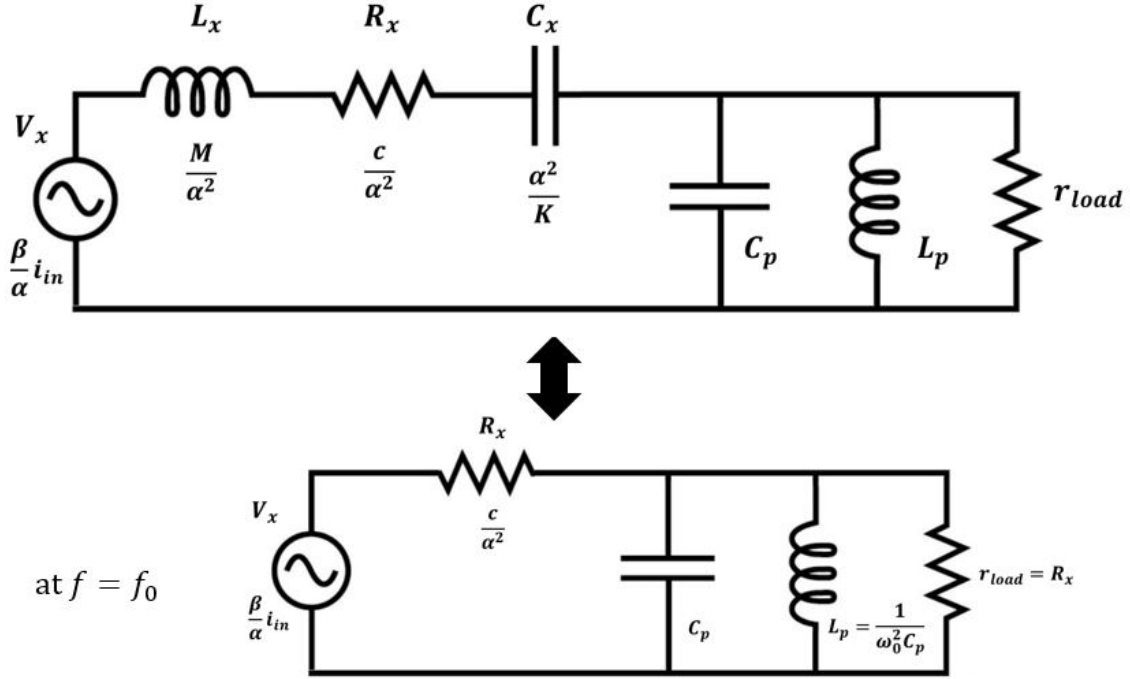


Figure III-2: Lumped circuit representation of the impedance matching between the ME transducer and a resistive load ( $r_{load}$ ) using an inductor  $L_p$  connected in parallel to the capacitance  $C_p$  at  $f = f_0$  ( $f_0$  is the short circuit frequency)

than for larger coupling. Some of these architectures adapted for our situation will be discussed in this chapter.

One could imagine that the addition of a bulky inductor  $L_p$  to compensate for the capacitance  $C_p$  is easy. However, it is not an optimal solution. In practice, the optimal load is not constant at all frequencies which makes it difficult to achieve impedance matching by adding only an inductor. Another reason is that the core losses in the inductor ( $P_{core}$ ) are directly related to the operating frequency  $f$  and the peak value of the magnetic flux density  $B$ . If the operating frequency is large, the inductor losses tend to increase. A wide used calculation formula to predict the core losses is the Steinmetz's equation  $P_{core} \propto f^\alpha B^\beta$  with  $\alpha$  and  $\beta$  two constants found by curve fitting [116] (typically  $\alpha$  is between 1 and 2). At the same time, the optimal resistive load  $r_{load}$  tends to increase because its order of magnitude is  $1/C_p\omega_0$ . Finding an inductor with a decent amount of losses at the operating frequency with dimensions compatible with implants remains a tricky task.

Several power management circuits exist in the literature to ensure impedance matching between PE transducers and the load. Using these circuits, the power transferred to the load may achieve a limit called  $P_{lim_{PE}}$  under certain conditions. In this chapter, we will first develop the condition to achieve the power limit  $P_{lim_{ME}}$  for a ME transducer. Then, we will provide the formula of  $P_{lim_{ME}}$ . Finally, we will choose and adapt existing management circuits to our ME transducers. A discussion on the results will be carried out at the end.

## 2 Output power of magnetoelectric transducer

### 2.1 Power limit of the magnetoelectric transducer

#### 2.1.1 Definition of the power limit

The power limit has a well known definition in piezoelectric theory [100]. In fact, the piezoelectric system (actuation source, transducer and the load) can be modeled as an equivalent electric circuit. If we can apply the impedance matching theory we can transfer the maximum of the power at a specific operating point of the system. This chapter starts with an analogy between PE transducers and ME transducers to determine the expression of  $P_{lim}$  for a ME transducer.

#### 2.1.2 Conditions to reach the power limit

In order to reach impedance matching, some specific operating conditions must be fulfilled. In the literature we can find how to determine these conditions for piezoelectric transducers. To determine them, we followed the same computation procedure as for the PE transducers because of the resemblance between the PE and ME model. This procedure is explained in [102]. Here are the computation steps in brief (note: in this demonstration, all parameters are assumed to be constant):

- We assume that the input current in the coil is a sine wave at a pulsation  $\omega$   
 $i_{in} = i_0 \sin(\omega t)$ .

- We write the expression of the the normalized displacement as follow:

$$X = a_{X_0} + \Sigma[a_{X_n} \cos(n\Omega t) + b_{X_n} \sin(n\Omega t)](n \geq 1) \quad (\text{III.1})$$

- We write the expression of the output power of the ME transducer as a function of the displacement coefficients  $a_{X_i}$  and  $b_{X_i}$
- By computing the maximum of the power ( $dP_{out}/dt = 0$ ), we find the optimal condition on the value of the displacement coefficient. The corresponding condition is  $a_{X_1} = Q/2\Omega$  and that all other terms of the harmonic decomposition are null. This means that  $x$  is a pure sine-wave in quadrature with the actuation current.
- We write the expression of the normalized output voltage as follow:

$$U = a_{U_0} + \Sigma[a_{U_n} \cos(n\Omega t) + b_{U_n} \sin(n\Omega t)](n \geq 1) \quad (\text{III.2})$$

and we integrate it in the first equation of the model

- In the equation III.1 of the model we replace  $U$  and  $X$  by their respective expressions
- We write an equation system (III.3) and (III.4) between the non-zero coefficients ( $a_{X_1}$ ,  $a_{U_1}$  and  $b_{U_1}$ ) by separating the term in  $\sin(n\Omega t)$  and  $\cos(n\Omega t)$ .

$$a_{X_1}(1 - \Omega^2) = -a_{U_1}, \quad (\text{III.3})$$

$$b_{X_1}(1 - \Omega^2) - a_{X_1} \frac{\Omega}{Q} = -b_{U_1} - 1 \quad (\text{III.4})$$

- We compute the coefficients of  $U$  at the maximum power point where the condition on  $a_{X_1}$  already given ( $a_{U_1} = Q(\Omega^2 - 1)/2\Omega$ ,  $b_{U_1} = -1/2$  and the other coefficients in the expression of  $U$  are equal to zero)

- Writing  $u = u_1 \sin(\omega t + \phi)$ , the transfer function between the first-harmonic voltage and the first-harmonic motion can be expressed by the quadratic and the phase components  $U_p$  and  $U_q$  respectively (III.5).

$$\frac{U_1}{X_1} = k_m^2 (U_p(\Omega) + jU_q(\Omega)), \quad (\text{III.5})$$

This leads to the two conditions guaranteeing impedance matching (III.6) and (III.7).

$$\Omega^2 = 1 + k_m^2 U_p(\Omega), \quad (\text{III.6})$$

$$k_m^2 Q = -\frac{\Omega}{U_q(\Omega)} \quad (\text{III.7})$$

### 2.1.3 Figure-of-merit of the magnetoelectric transducer

It was pointed out in [117] that the electromechanical coupling coefficient  $k^2$  is not the primary factor for predicting a piezoelectric energy harvesting capabilities. However we can find in the literature better criteria as the figure of merit (FoM) that depends on the material parameters for material-level models [86]. For piezoelectric system-level model there is a well-known FoM which is the product  $k_m^2 Q$  appearing in (III.7). It was proven that depending on this FoM, optimal power transmission may or may not be achieved by a circuit at a given frequency. It all depends on the mathematical possibility to verify simultaneously (III.6) and (III.7) [102]. Since the rules (III.6) and (III.7) are the same for PE and ME transducers,  $k_m^2 Q$  is also a relevant FoM for magnetoelectric systems. It is an important criterion in choosing the power management circuit for the transducer.

### 2.1.4 The power limit formula

In the literature, the theoretical limitation to the power transferred by a PE transducer when subject to a given acceleration  $\gamma = \ddot{y} = \gamma_m \sin(\omega t)$  is given by (III.8) [118]. This power limit can be achieved with a relevant power management circuit

between the transducer and the load, guaranteeing impedance matching.

$$P_{lim_{PE}} = \frac{M\gamma_m^2 Q}{8\omega_0} \quad (\text{III.8})$$

A significant difference between the PE and the ME transducers is that the latter is not an inertial system, which means that its actuation force  $\beta i_{in}$  (see (II.23)) is not proportional to its mass (whereas it is  $\gamma M$  for the PE transducer (III.10)). Another significant difference lies in the fact that the parameters  $k_m^2$  and  $Q$  are the result of the complex magnetic, mechanical and electrical interaction between the piezoelectric and the magnetostrictive layers. Our experiments prove that both parameters differ from the coupling coefficient and quality factor of the piezoelectric sample alone. No analytical expression is available for such a system. However, considering the analogy between the PE and ME models, the determination of the power limit for a ME transducer actuated by an AC input current  $i_{in} = i_0 \sin(\omega t)$  can be obtained with the substitution (III.9).

$$M\gamma_m \leftrightarrow \beta i_0, \quad (\text{III.9})$$

This substitution leads to the maximum theoretical power  $P_{lim_{ME}}$  (III.11). Contrary to PE transducers, the power limit of ME systems is not proportional to the effective mass  $M$ , but to the square of the expedient magnetoelectric coefficient  $B_m$ . It is also proportional to the transducer FoM  $k_m^2 Q$ , which is a significant difference with the PE case.

$$M \frac{d^2 x}{dt^2} + c \frac{dx}{dt} + Kx + \alpha u - M\gamma = 0, \quad (\text{III.10})$$

$$P_{lim_{ME}} = \frac{B_m^2 k_m^2 Q i_0^2}{8C_p \omega_0} \quad (\text{III.11})$$

All these considerations about the FoM and the maximum power transmission of a ME transducer highlight the importance of the system-level parameters  $k_m^2$ ,  $Q$ ,  $B_m$  and  $C_p$ . In the following section, we validate this model experimentally and quantify the nonlinear behavior of our ME transducer. We determine the impact of this nonlinear behavior on the maximum power and FOM of the generator.

### 2.1.5 Impact of parameter variations on circuit design

The transferable power as well as the impedance matching condition are affected by the nonlinear behavior of the system through the variation of  $Q$ . One may wonder about the consequences of the previous characterization on the output power when the input current is constant, which is the most common and practical situation. In such case, we have demonstrated that a good way to determine the system response is to characterize it at several levels of output current and then reconstruct the response for a given input current. This is what we did in Fig. III-3, where we plot the power vs. frequency curves for the optimal load ( $680\Omega$ ) for regulated input currents of  $11.3mA$ ,  $19.8mA$  and  $35.4mA$ . We compare the result to what one would expect from a characterization of a linear system. This graph highlights how the peak power measured at  $11.3mA$  would be overestimated by around 48% with the linear assumption. Since the load has been optimally chosen, the experimental peak power reaches the power limit  $P_{lim}$  (III.11) predicted from the identified parameters. This discussion remains qualitatively valid for other input levels. However, the situation is even more complex that the exact conclusions quantitatively depend on the considered levels of current. At higher input levels, the same conclusions hold. However, the discrepancy between the linear assumption and the experimentally-validated model increases. For instance, results at  $i_0 = 35.4mA$  lead to an overestimation of 61%, instead of 48% previously (see Fig. III-3).

The nonlinearity of the transducer also affects the value of the optimal load which linear theory would expect to be  $350\Omega$ , as obtained from the results given in [100].

All these considerations have a huge impact on further circuit design.

## 2.2 Power management circuits for magnetoelectric transducer

### 2.2.1 Introduction

The lumped model of the ME and PE transducers are quite similar and could be represented with the same components. We can notice two differences: the first is in the actuation source represented by  $V_S$  ( $\beta i_{in}$  for ME and  $M\gamma$  for PE). The second

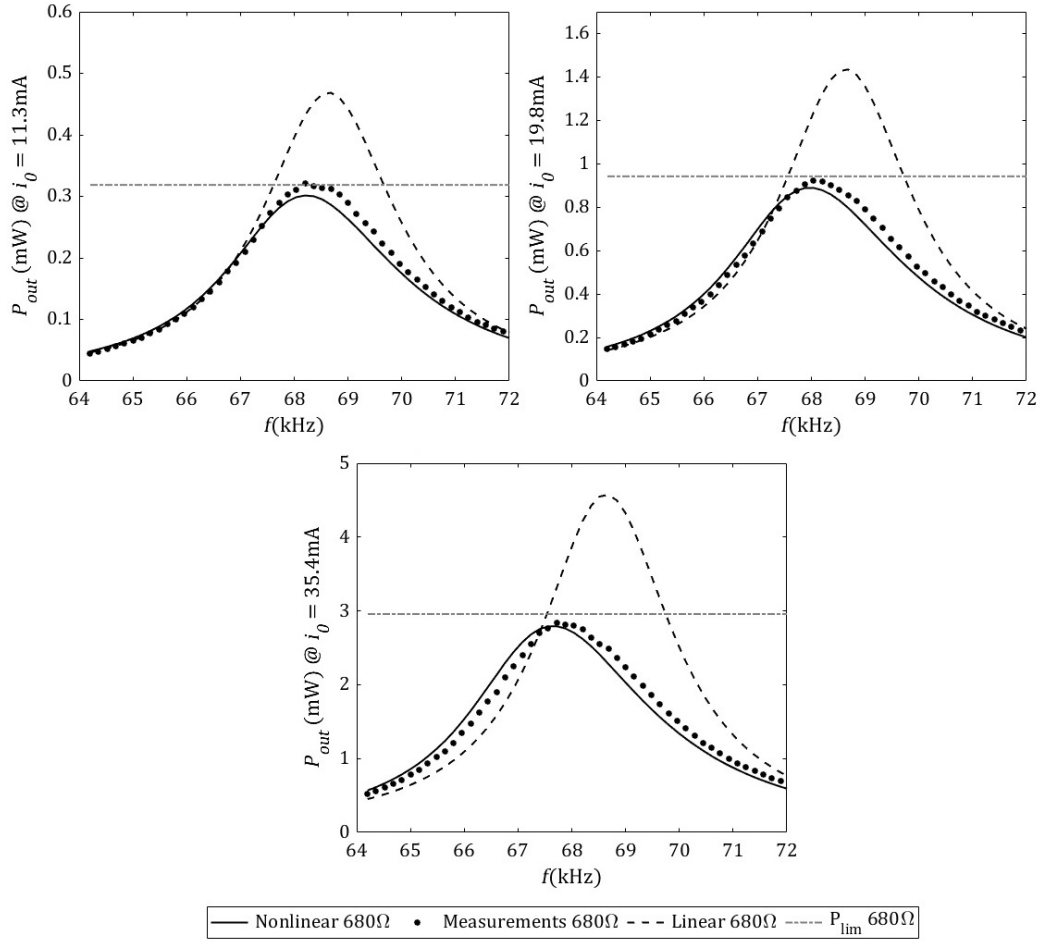


Figure III-3: Power vs. frequency responses for a regulated amplitude of the input current (left:  $i_0 = 11.3\text{mA}$ , middle:  $i_0 = 19.8\text{mA}$ , right:  $i_0 = 35.4\text{mA}$ ). Dots : Experimental measurements. Solid lines : Responses reconstructed based on the characterization at regulated output currents. Dashed lines : Responses expected from a linear model. Dash-dot line (gray): power limit of the ME transducer.

difference is the nonlinear behavior of the ME transducer when the actuation level changes. However, when the amplitude and the frequency of the output current of the transducer are fixed, the parameters of the model are constant. In most of the cases, the load is not optimal. Therefore, to maximize the power transfer we use power management circuit between the transducer and the load. In [102] we find a review on the existing power management circuit for PE transducer. The circuits are classified into strategies (adaptive or non adaptive control), topologies (number of stages in the circuit: rectifier, DC-DC converter,..), architectures and techniques as shown in Fig. III-4 [102]. Due to the similitude between ME and PE models at fixed operating point (fixed amplitude and frequency of the source), and between the conditions to reach the power limit for both transducers, we will choose some of the existing circuits and verify by simulation if they can be used as power management circuits for ME transducers.

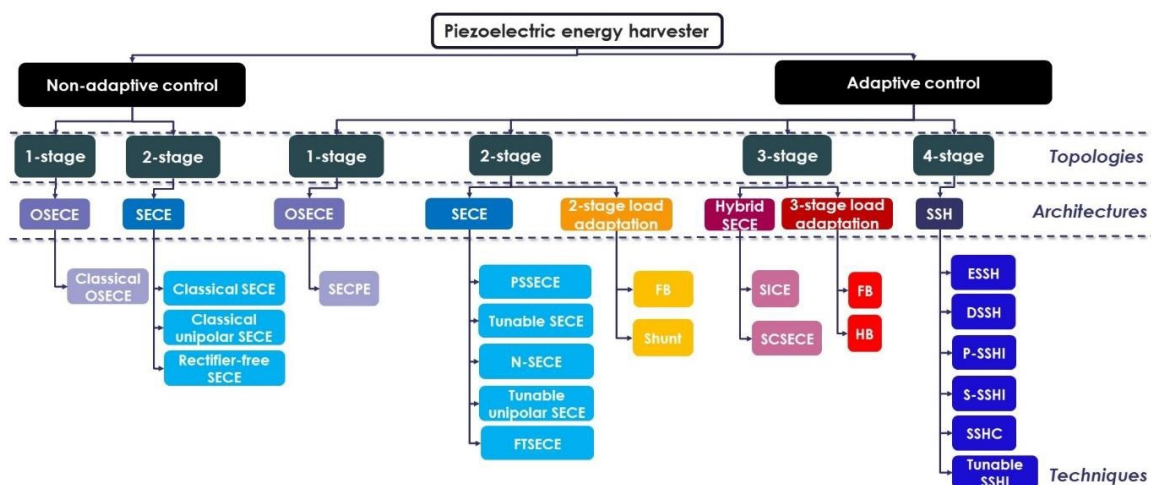


Figure III-4: Summary of the existing strategies, topologies, architectures and techniques of piezoelectric harvesting circuits [102]

### 2.2.2 Power terms in the system

When connecting a power management circuit between the load and the transducer three power terms should be defined. The first term is the emitted power  $P_E$  sent by the excitation coil to the ME transducer. The second term is the extracted power  $P_{ext}$  which is the power transferred from the capacitance  $C_p$  of the piezoelectric element

to the input of the power management circuit. The third term is the harvested power  $P_{harvest}$  which is the power transferred from the conditioning circuit to the load. A schematic shows the power flow in Fig. III-5. One can define then the power conversion efficiency as the harvested power divided by the extracted power.

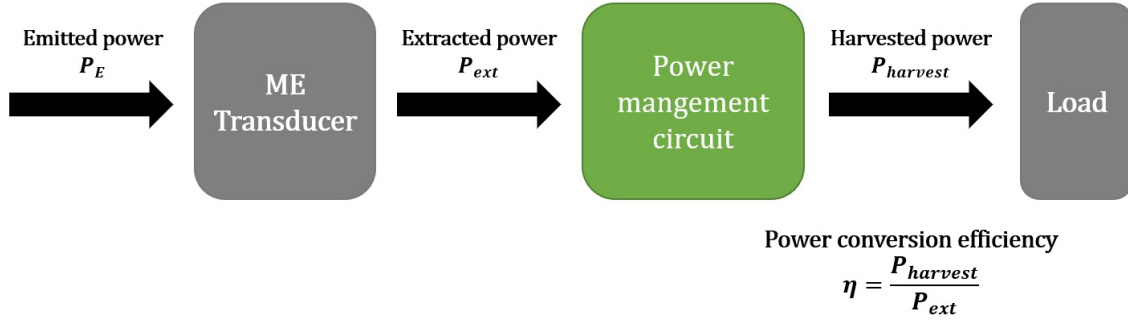


Figure III-5: Power flow in the system (transducer, conditioning circuit and load).  $\eta$  is the power conversion efficiency of the management circuit only.

### 2.2.3 Selection criteria of the power management circuits

For certain PE power management circuits, the value of the figure-of-merit  $k_m^2 Q$  of the PE transducer determines if the output power can reach or not the power limit using these circuits [102]. For instance, the standard circuit (SEH) [119] can achieve the power limit only if  $k_m^2 Q \geq \pi$ . Other circuits as the SECE (Synchronized Electric Charge Extraction) can reach the power limit for only one value of  $k_m^2 Q = \pi/4$ . Fig. III-6 shows the condition on the FoM to reach the power limit for different techniques.

Therefore the FoM  $k_m^2 Q$  will be also a key criteria in the choice of the power management circuit for ME transducer. However, for the ME transducers, the value of  $k_m^2 Q$  depends on the operating point of the transducer. In Fig. III-7 we can notice that our ME sample has a  $k_m^2 Q = 1.5 \approx \pi/2$  at the higher value in the operating point interval ( $i_1 \approx 2.5mA$ ). In this case the circuit USECE may be a good candidate. Fig. III-6 shows also that SSHI can be a power management circuit for PE transducer with any FoM value. However, this techniques may not be a good choice for ME transducer mainly because of the difference between PE and ME transducers in their

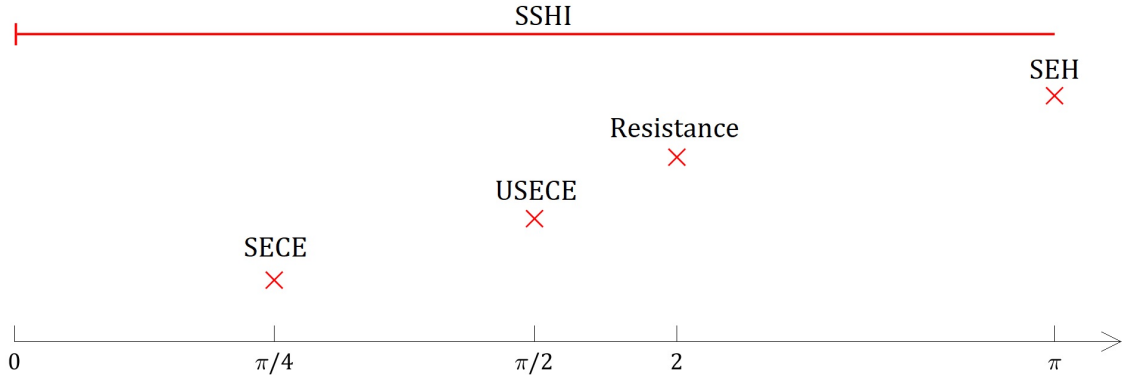


Figure III-6: Optimal values of the figure-of-merit  $k_m^2 Q$  for piezoelectric harvesting techniques

operating frequency (hundreds of hertz for PE transducers and about  $70KHz$  for our ME transducer). In fact the control circuit of the SSHI technique should invert instantaneously the voltage twice a period which requires a very high frequency in the control circuit (compared to the operating frequency). This will significantly increase the switching losses in the control circuit. Therefore, we studied only the Unipolar Synchronous Electric Charge Extraction (USECE) circuit and we compared the results with the standard energy harvester (SEH).

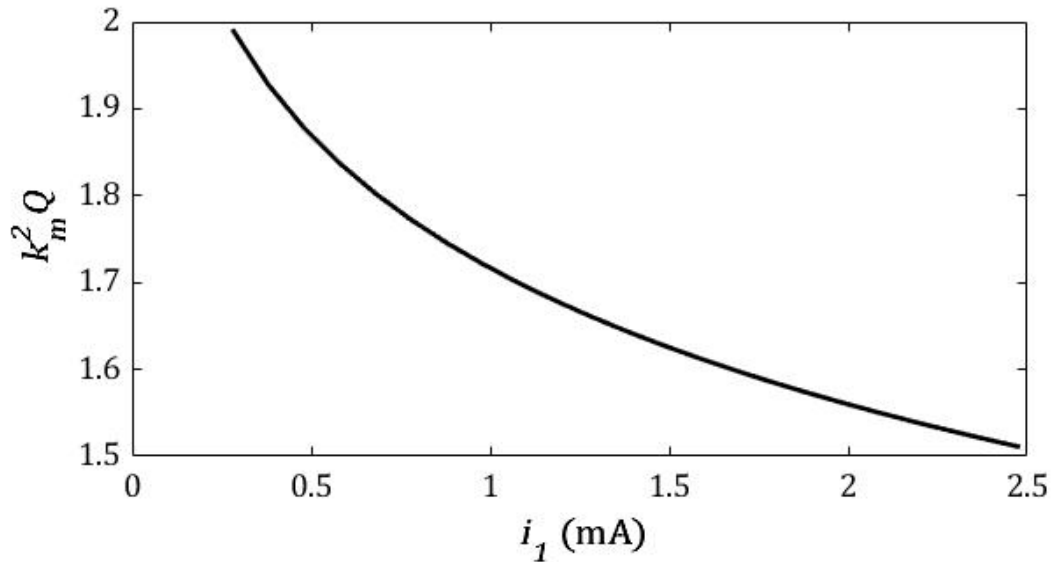


Figure III-7: The dependency of  $k_m^2 Q$  on the output current  $i_1$  of the ME transducer sample

The simulation results will be compared with the theoretical expectation of the ratio between the power limit and the extracted power as a function of the figure of merit  $k_m^2 Q$ . The theoretical expectations are based on the results given in [119] and [120] and can be illustrated as shown in Fig. III-8. In this figure we also show what we can expect as power ratio for the boundaries of the  $k_m^2 Q$  intervals of our transducer ( $k_m^2 Q = 1.5$  and  $2$ ).

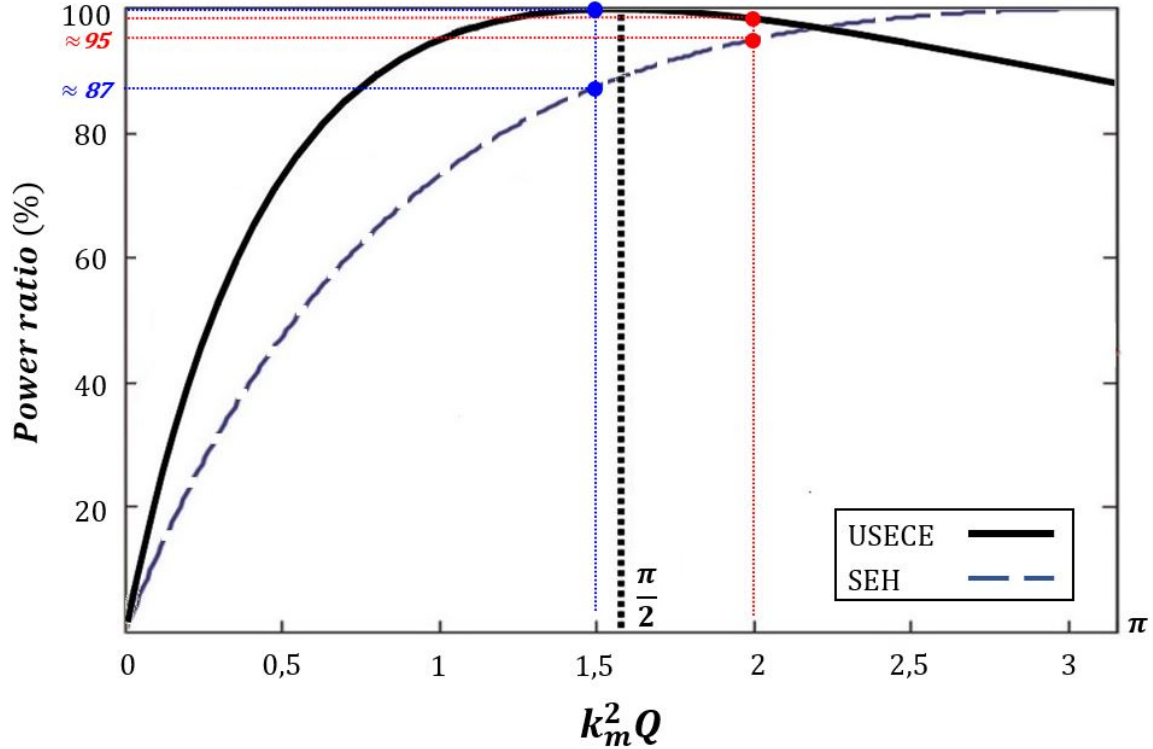


Figure III-8: Ratio between the extracted power and the power limit for USECE and SEH circuits based on the results given in [119] and [120]

#### 2.2.4 Power management circuit simulation

In this section we show and discuss the simulation results for two power management circuits: the SEH circuit [121, 122, 123, 124] and the USECE circuit [120, 125]. These circuits have initially been proposed for piezoelectric transducers. Here we will connect these circuits to the equivalent lumped parameter model of the ME transducer. The circuits were simulated in LTspice. We recall that the ME transducer parameters change with the output current amplitude  $i_1$ . Therefore the components

of the ME transducer electrical model  $L_{mech}(i_1)$ ,  $R_{mech}(i_1)$  and  $C_{mech}(i_1)$  are function of the amplitude  $i_1$  too. In Ltspice we replace the values of these components by the behavioral law introduced in chapter II.

### 2.2.4.i Standard energy harvesting circuit

#### a State-of-the-art : Description of the SEH circuit topology and impedance matching condition

The SEH circuit is based on a rectifier, a smoothing capacitor and a DC-DC converter (often a buck-boost converter). The topology of this circuit is given in Fig. III-9. For a piezoelectric transducer, it was proven that the power limit can be reached with this SEH circuit as soon as  $k_m^2 Q \geq \pi$  if the switching frequency and the duty-cycle controlling the DC-DC converter are properly chosen [100, 126]. This theory is also

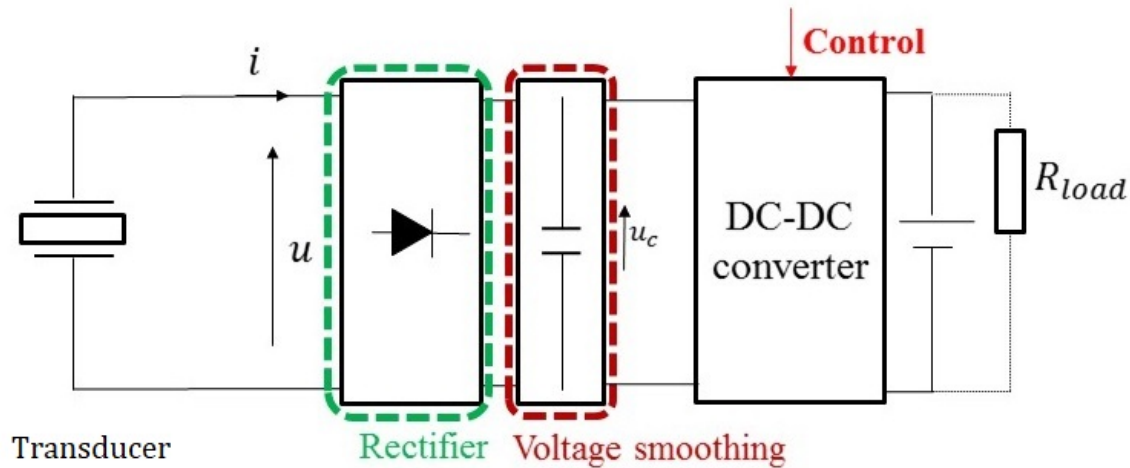


Figure III-9: Topology of 3 stage SEH circuit

valid for our ME transducer, except that it is more complex due to the dependency between the parameters of the model and the output current. Appendix 1 shows a procedure to determine the expression of the optimal resistive loads. The optimal resistive load is the equivalent load (corresponding to the DC-DC converter seen by the transducer) that leads to extract the maximum of the power at a fixed actuation level and for a linear system (with constant parameters). In other words, in most ap-

plications, the equivalent load that the DC-DC converter must present to the circuit depends on the actuation frequency.

### **b Implementation proposed for the SEH circuit**

The full SEH circuit with impedance matching at the frequency corresponding to the maximum power (close but different from  $f_0$ ) has been implemented in LTSpice. The schematic is given in Fig. III-10. The circuit is a three-stage power management circuit. The first stage is the half-bridge rectifier made of two diodes D1 and D2. The second is the voltage smoothing stage using the capacitor  $C_{DC}$ . The third stage is the DC-DC buck boost converter formed of the inductor  $L_1$ , the diode  $D_3$  and the N-channel MOSFET  $M_1$ . The voltage source  $V_1$  represents the load (a battery or a supercapacitor). The impedance matching in the circuit lies in the control of the MOSFET  $M_1$  in the third stage in order to make the DC-DC converter behave as the optimal resistive load in the system (transducer, load and conditioning circuit). To guarantee this resistive matching independently of the output voltage across the voltage source  $V_1$ , the buck-boost converter should work in discontinuous current mode (DCM). Another impedance matching condition could also be found in continuous conduction mode but then the optimal load depends on the voltage across the output ( $V_1$ ) so that impedance matching becomes complex as soon as the output is connected to a storage element (like a supercapacitor). Fig. III-12 shows the voltage and current (in the coil  $L_1$ ) waveforms when the energy transfer occurs. In this case, the average current at the input of the converter is independent of the system to supply (the load connected afterwards to the supercapacitor or battery) [123] as long as the circuit remains in DCM.

The MOSFET is controlled with a pulse width modulated (PWM) signal. We define the switching frequency  $f_{switching}$  of the control circuit, the duty cycle  $d$  and the value of the inductor  $L_1$  inside the converter. The optimal impedance matching condition is detailed in Appendix 2. Fig. III-11 shows the control circuit that generates the PWM signal. It is a comparator-based relaxation oscillator. This oscillator is supplied directly by the voltage across the smoothing capacitor  $C_{DC}$ .

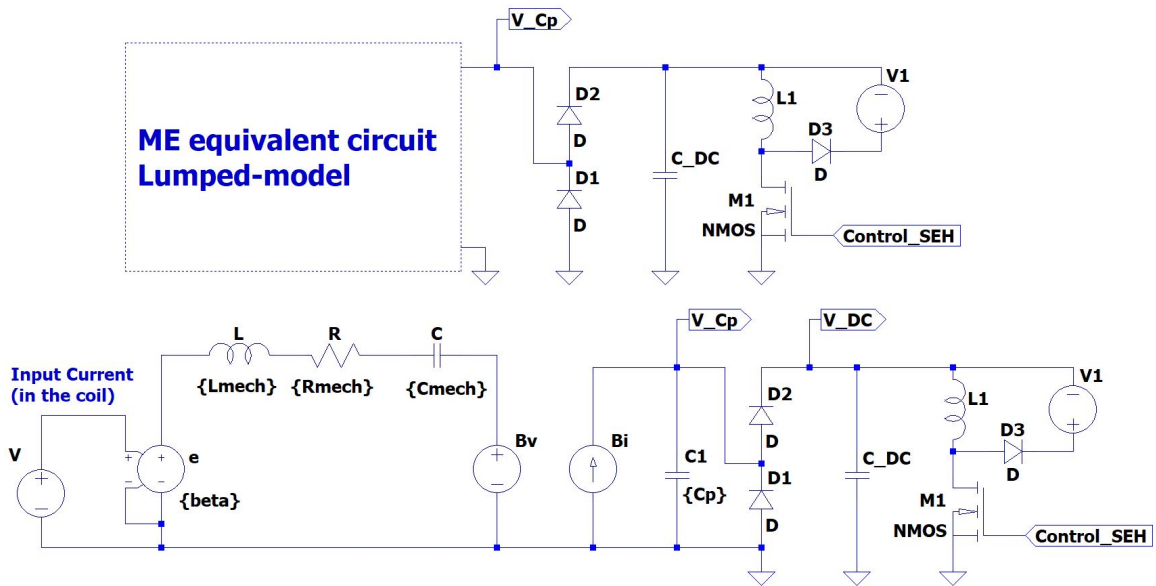


Figure III-10: SEH circuit implementation in LTspice  $L_1[3.5mH, 40\Omega]$

## Control Circuit

### Comparator-based relaxation oscillator

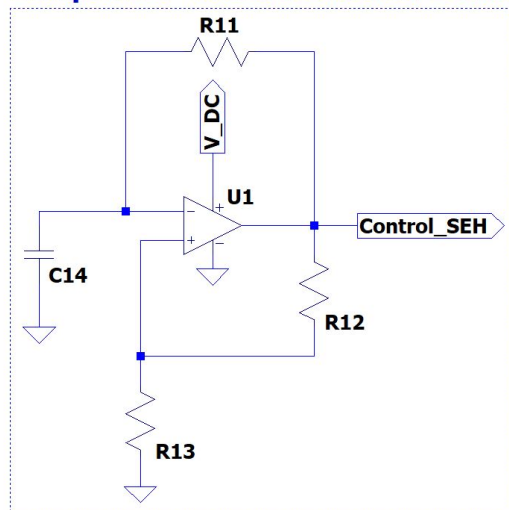


Figure III-11: A comparator-based relaxation oscillator in the control circuit of the SEH technique

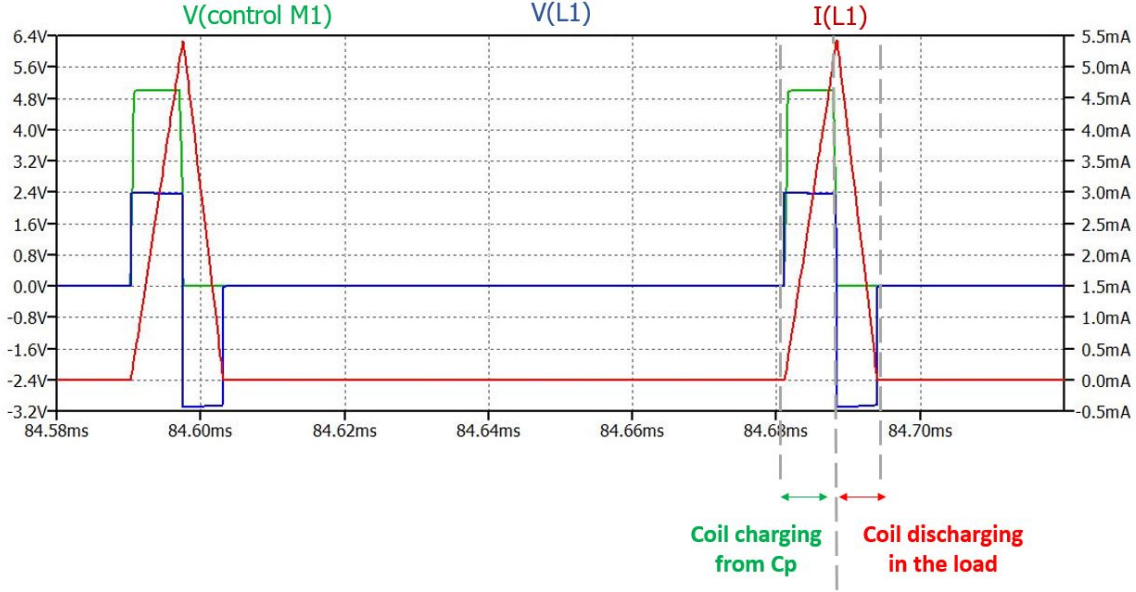


Figure III-12: The waveform of the voltage and the current of the coil  $L_1$  in discontinuous current mode. The green waveform represents the control signal of the mosfet  $M1$

#### 2.2.4.ii Unipolar synchronized electric charge extraction circuit

##### a State-of-the-art : Description of the USECE circuit topology and impedance matching condition

Fig. III-13 shows the topology of the synchronized electric charge extraction circuit (SECE) circuit. The first stage in this topology is a rectifier and the second is the charge extraction stage. With this technique, the energy transfer from the capacitance of the piezoelectric transducer to a coil in the charge extraction stage happens at the maximum amplitude of the transducer output voltage ( $V_{Cp}$ ). In SECE the first stage is a full-wave rectifier. The Unipolar synchronized electric charge extraction circuit (USECE) has the same topology of SECE. The first stage of USECE is a half wave rectifier.

Fig. III-14 shows the theoretical waveform of the voltage  $V_{Cp}$  at the terminal of the piezoelectric element and a zoom on the time interval of the energy transfer in USECE technique.

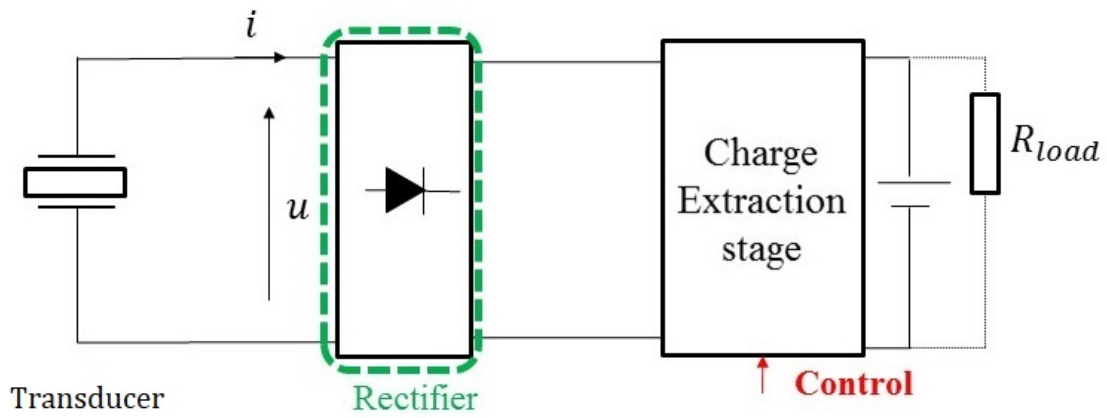


Figure III-13: Topology of the SECE technique

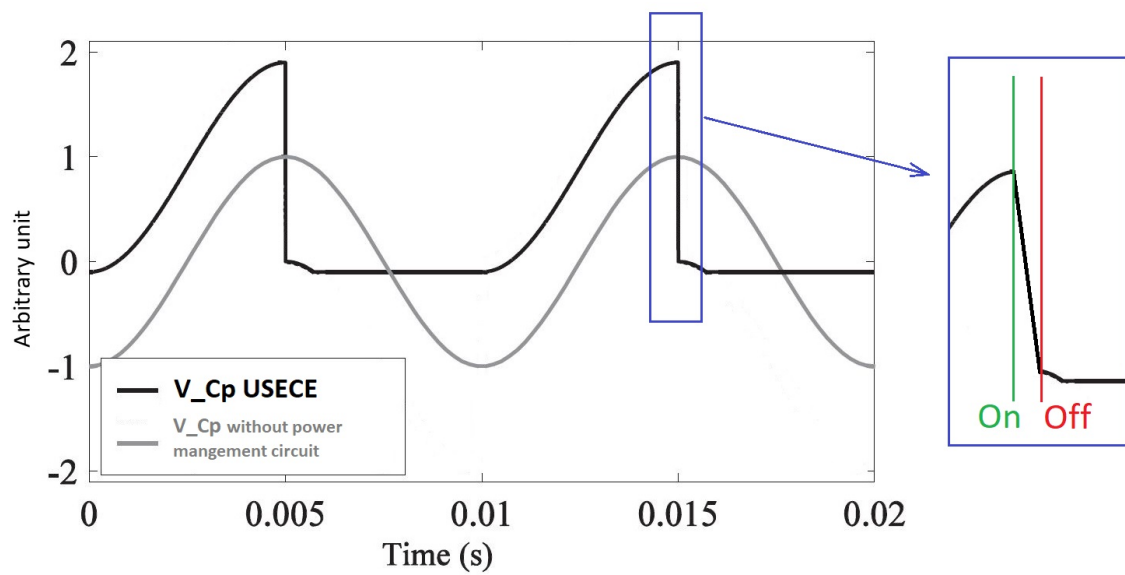


Figure III-14: Waveform of the voltage across the piezoelectric element  $V_{Cp}$  in the USECE technique.

### b USECE implementation with RS latch

Fig. III-15 shows the implementation of the USECE circuit in LTspice. There are two stages in this circuit. The first is the shunt-diode rectifier (diode  $D_1$ ). The second is the charge extraction stage: the inductor  $L_1$ , the diode  $D_2$  and the N-channel MOSFET  $M_1$ . The control circuit of the MOSFET is shown in Fig. III-16. The main purpose of this control is to store the energy temporarily in the inductor  $L_1$  and deliver it to the load in one half-cycle. This reduces the conduction time of the MOSFET and thus the conduction losses. To establish this control, the MOSFET should be turned on when the piezoelectric voltage  $V_{Cp}$  is maximum and turned off when  $V_{Cp}$  reaches zero. This is done using a RS latch. Fig. III-17 shows in a) a system representation of the RS latch, in b) a detailed implementation of an RS-latch. The RS latch has two inputs (set and reset) and two outputs ( $Q$  and  $\bar{Q}$ ). The truth table of the RS latch is given in Fig. III-18. The set and reset inputs detect the peak and the zero crossing of the voltage  $V_{Cp}$  respectively. For the set signal we connect a comparator to make the comparison between the signal  $V_{DC}$  (which represents the maximum of the piezoelectric capacitor  $C_p$  voltage) and  $V_{Cp}$  (the instantaneous piezoelectric capacitor voltage). For the reset signal, an inverter is used to detect the zero crossing moment of the voltage signal  $V_{Cp}$ . The output  $Q$  controls the MOSFET  $M_1$ . In this case, the MOSFET  $M_1$  stays on from the peak detection to the zero crossing of the signal  $V_{Cp}$ .

### 2.2.4.iii LTSpice Simulation

#### a Operating points of the simulations

The voltage source  $e$  in the ME equivalent lumped-model represents the actuation source of the transducer. Its value  $e$  is equivalent to the input current of the excitation coil and thus it represents the dynamic magnetic field. In the simulations of the circuits, we test an interval range of input current between  $10mA$  and  $200mA$ . This is equivalent to an extracted power between  $250\mu W$  and  $60mW$  and an output current  $i_1$  between  $400\mu A$  to  $7.5mA$ . The load is a DC voltage source of  $3V$ , to be charged by the harvesting circuit. A frequency sweep between  $67.5kHz$  and  $70kHz$  at different

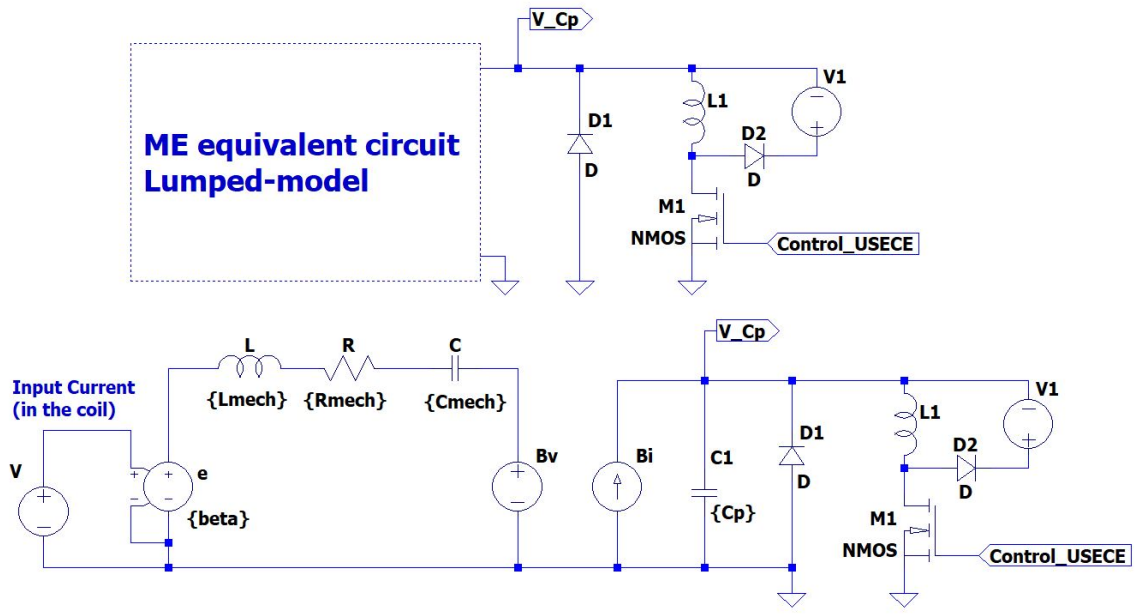


Figure III-15: USECE circuit implementation in LTspice ( $L_1[3.5mH, 40\Omega]$ )

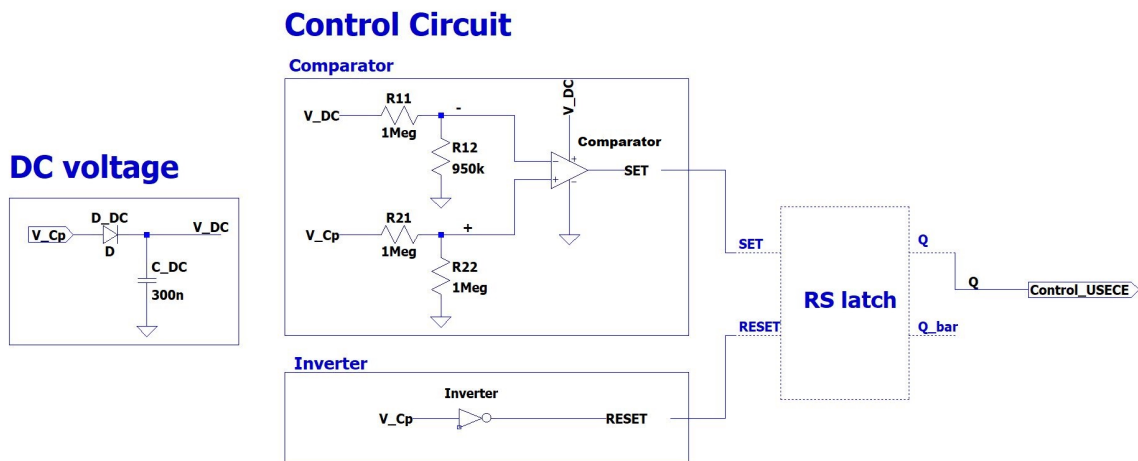
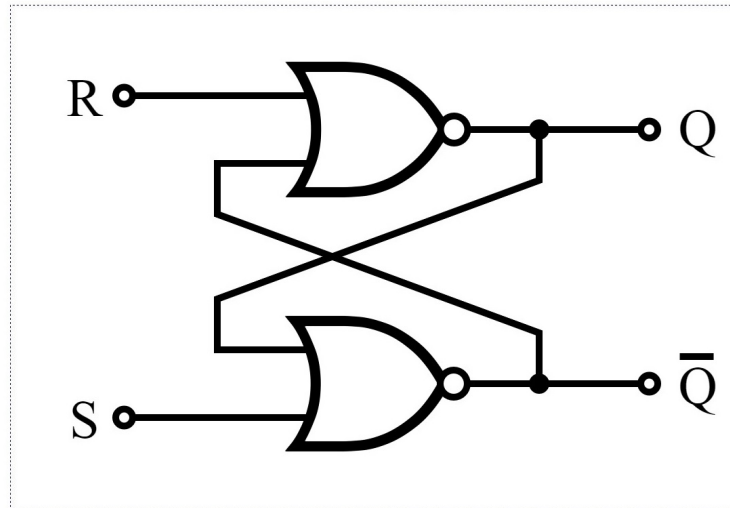


Figure III-16: Control and power supply circuits of the USECE technique.

a)



b)

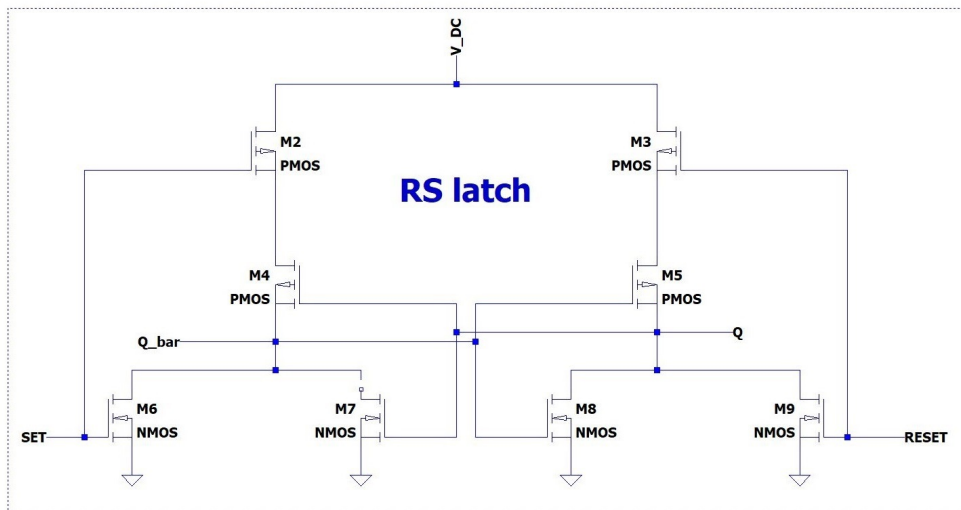


Figure III-17: Examples of RS latch circuit topologies: a) a system representation of the RS latch with two NOR , in b) a detailed implementation of an RS-latch with 4 N channel mosfet and 4 P-channel mosfet.

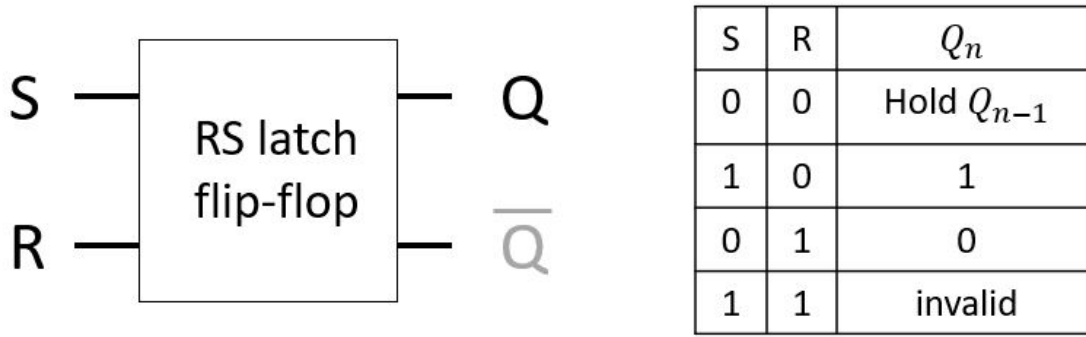


Figure III-18: Truth table of the RS latch .  $Q_n$  and  $Q_{n-1}$  are the current and previous state of the output  $Q$

actuation level showed that the resonant frequency of the overall system for all the considered circuits is about  $68.5kHz \pm 0.2kHz$ . Thus, the operating frequency is set at  $68.5kHz$  in all simulations .

### b Extracted power with respect to the power limit

By definition, the power limit is the maximum power that a ME transducer can transfer to a circuit connected to its electrical terminals (as already stated in section 2.1.4). Therefore the ratio between the extracted power ( $P_{ext}$ ) and the power limit ( $P_{lim}$ ) is an important criterion to compare the performance of both management circuits USECE and SEH. The simulation results showed that, for an extracted power up to  $60mW$ , this ratio is between 92% and 99% with the USECE technique. This ratio is also high with the SEH technique but it is lower than 90% for the same range of extracted power. It goes down to 79% at the higher bound of power interval ( $60mW$ ). The results are shown in Fig. III-20. In Fig. III-21, we showed the obtained power ratio  $P_{ext}/P_{lim}$  for our model of transducer.

### c Efficiency of the circuit

The power conversion efficiency is the harvested power divided by the extracted power as defined in section 2.2.2 (denoted efficiency in Fig. III-5). We assume that for both USECE and SEH circuits, the resistance of the coil  $L_1$  is equal to  $40\Omega$  (based on impedance analyzer measurements of a  $4mH$  coil near to  $70kHz$ ) and the forward

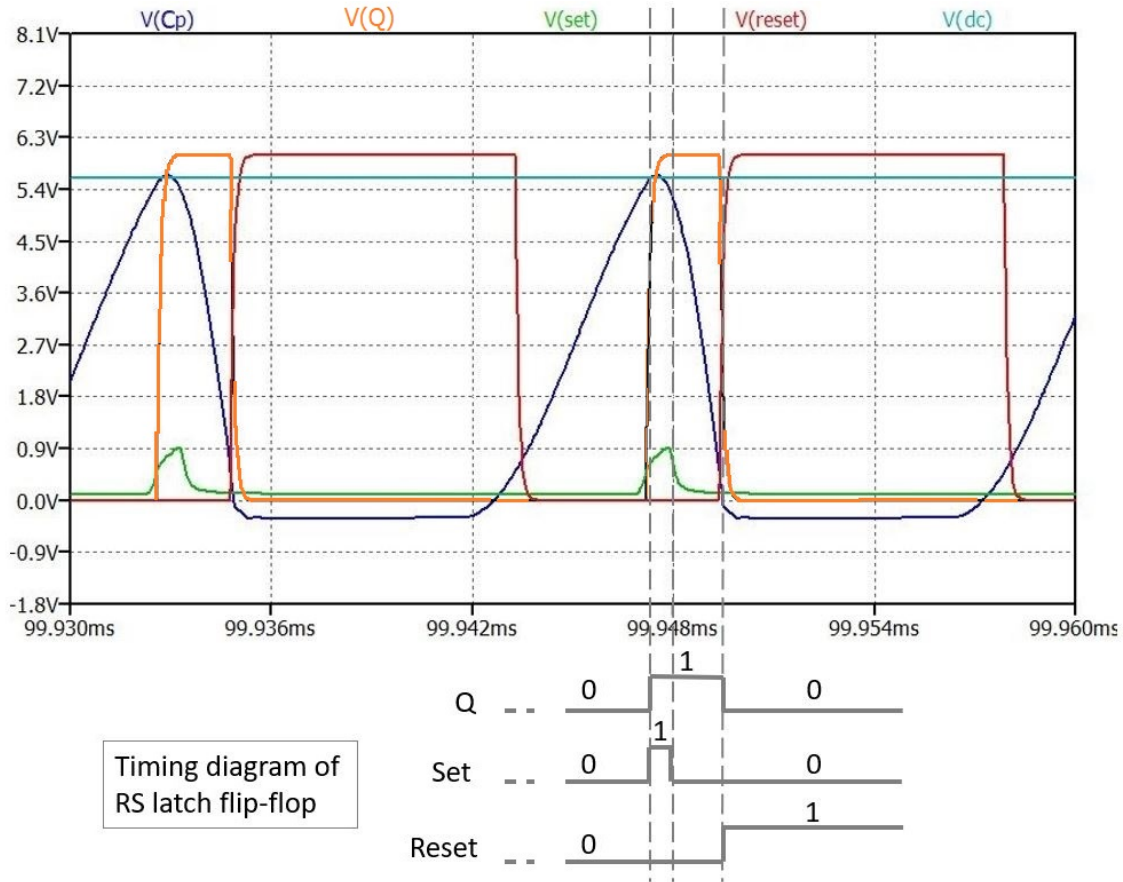


Figure III-19: Top: Voltage waveforms of the USECE circuit:  $V(set)$ ,  $V(reset)$ ,  $V(Q)$  of the RS latch flip-flop, voltage  $V(C_p)$  of the piezoelectric capacitance  $C_p$  and signal  $V(dc)$  which represents the maximum of  $V(C_p)$ . Down: Timing diagram of the RS signals Q, set and reset.

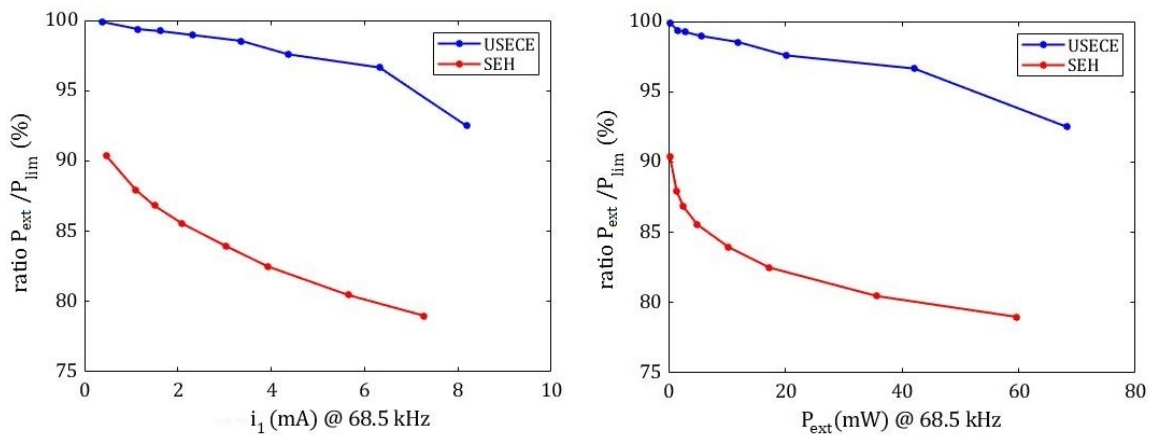


Figure III-20: Ratio between the extracted power ( $P_{ext}$ ) and the power limit ( $P_{lim}$ ) as a function of: the level of output current  $i_1$  (left) and the extracted power (right) of both USECE and SEH circuits

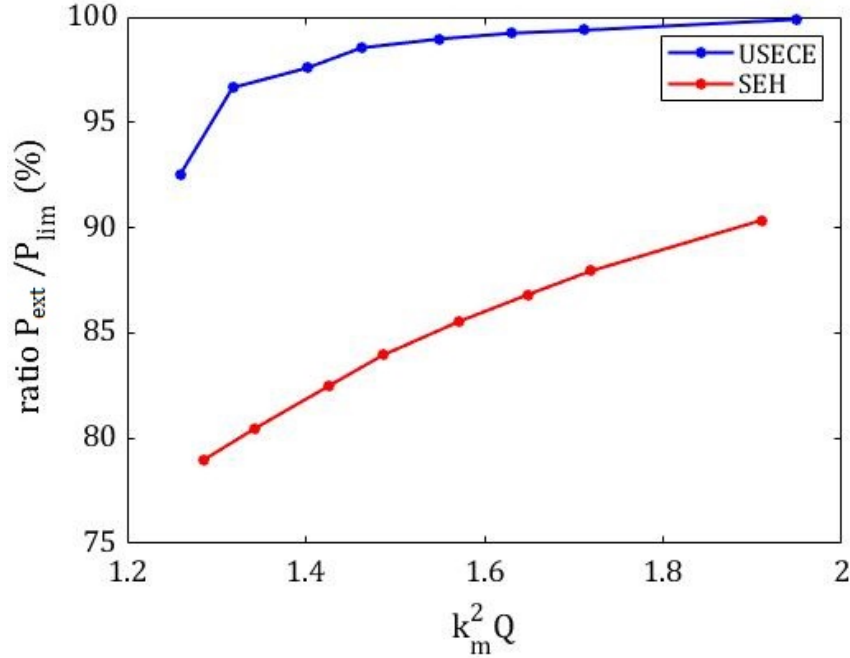


Figure III-21: Ratio between the extracted power ( $P_{ext}$ ) and the power limit ( $P_{lim}$ ) for different values of figure-of-merit  $k_m^2 Q$  of both USECE and SEH techniques

voltage of each diode is  $0.3V$ . The consumption of other components are not considered in the simulation and thus in the efficiency computation. We give in Fig. III-22 the value of the efficiency with respect to the input current  $i_{in}$ . The results shows that the USECE circuit efficiency is slightly higher than SEH circuit.

#### d Autonomous circuit for implants

To charge wirelessly an implant installed in the body, it should have a reasonable efficiency in order to charge the battery. Here we will assume that the reasonable efficiency is higher than 50%. In this case the available power at the different actuation level for both circuits (SEH and USECE) will be as shown in Fig. III-25.

- SEH circuit: In the SEH circuit, the consumption of the oscillator shown in Fig. III-12 is about  $225\mu W$ . This means that the circuit can work in autonomous mode when the input current of the excitation coil is higher than  $30mA$ .
- USECE circuit: In this circuit, many non-idealities were not taken into consideration when we computed the efficiency. For example, the consumption of the

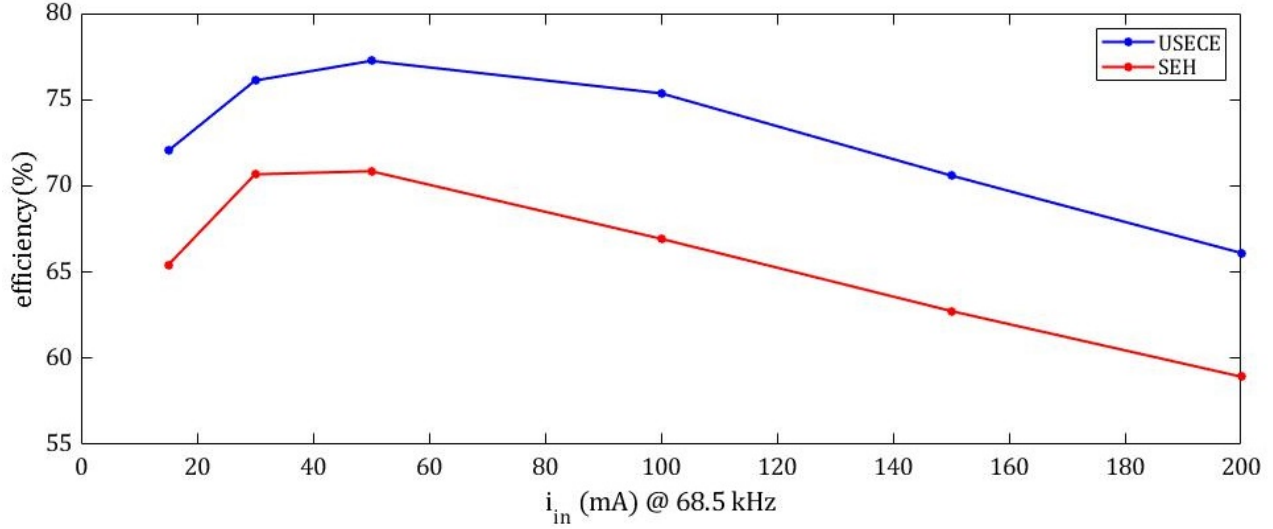


Figure III-22: The efficiency (%) of the USECE and SEH circuit

comparator that detects the maximum of the voltage  $V_{Cp}$  is neglected. So is the consumption of the inverter to detect the zero crossing moment and the RS latch to control the MOSFET. These components may actually consume more than the available power especially when operating at a frequency near  $70kHz$ . For this reason, we propose in the next paragraph a simpler circuit involving only 2 transistors instead of complex integrated circuits.

- Proposition of a simplified USECE circuit

Fig. III-23 shows an implementation of the USECE technique without active components. This circuit takes advantage of a PNP transistor to detect the peak of the piezoelectric voltage and a combination with a NPN transistor so that charge extraction stops when the piezoelectric voltage cancels out. The diodes in this circuit are schottky diode ( $v_{fwd} = 0.3V$ )

The main challenge in this technique is to find bipolar transistors that operate at  $70kHz$  and have a sufficient gain and a rise and fall time make it able to switch fast to ensure the power transfer between the capacitance  $C_p$  and the coil in the power extraction stage, while having an internal resistance as low as possible to optimize the power conversion efficiency. From Fig. III-26 (b), we

can notice that the power ratio between the extracted power and the power limit drops at a low actuation level. This means that this implementation of USECE actually underperforms the ideal performance of USECE (as in our previous implementation proposal). This can be explained by comparing the waveforms at high and low input currents. Indeed, Fig. III-24 shows that there is a delay between the moment at which the voltage peak occurs and its detection to turn on the charge extraction. This delay increases as the amplitude of the actuation decreases. We illustrate this on two examples, one for an input current of  $30mA$ , and one for an input current of  $200mA$ . This delay causes a decrease of the power extracted from the piezoelectric element from 90% of  $P_{lim}$  at  $200mA$  to 68% of  $P_{lim}$  at  $15mA$  (independently of the power conversion efficiency of the circuit).

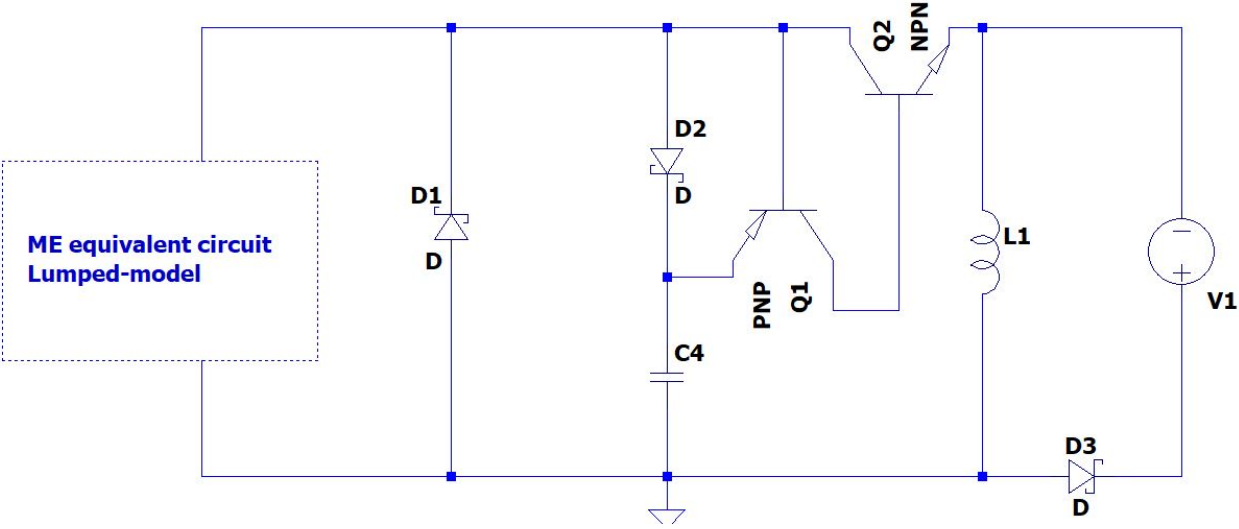


Figure III-23:  $USECE_{BJT}$  bipolar transistor circuit:  $Q_1$  and  $Q_2$  are ideal bipolar transistors in LTspice,  $D_s$  are schottky diodes ( $V_{threshold} = 0.3V$ ),  $V_1$  represents a load as a battery with constant voltage  $3V$ ,  $L_1 = 0.1mH$  and  $C_4 = 100pF$

As shown in Fig. III-26 the efficiency of this circuit drops at low actuation level. Although the  $USECE_{BJT}$  circuit degrades the extracted power compared to an ideal USECE because of the delay between peak voltage and charge extraction (especially at low levels), this circuit could be a good candidate because of its relatively good power efficiency due to the minimization of components it

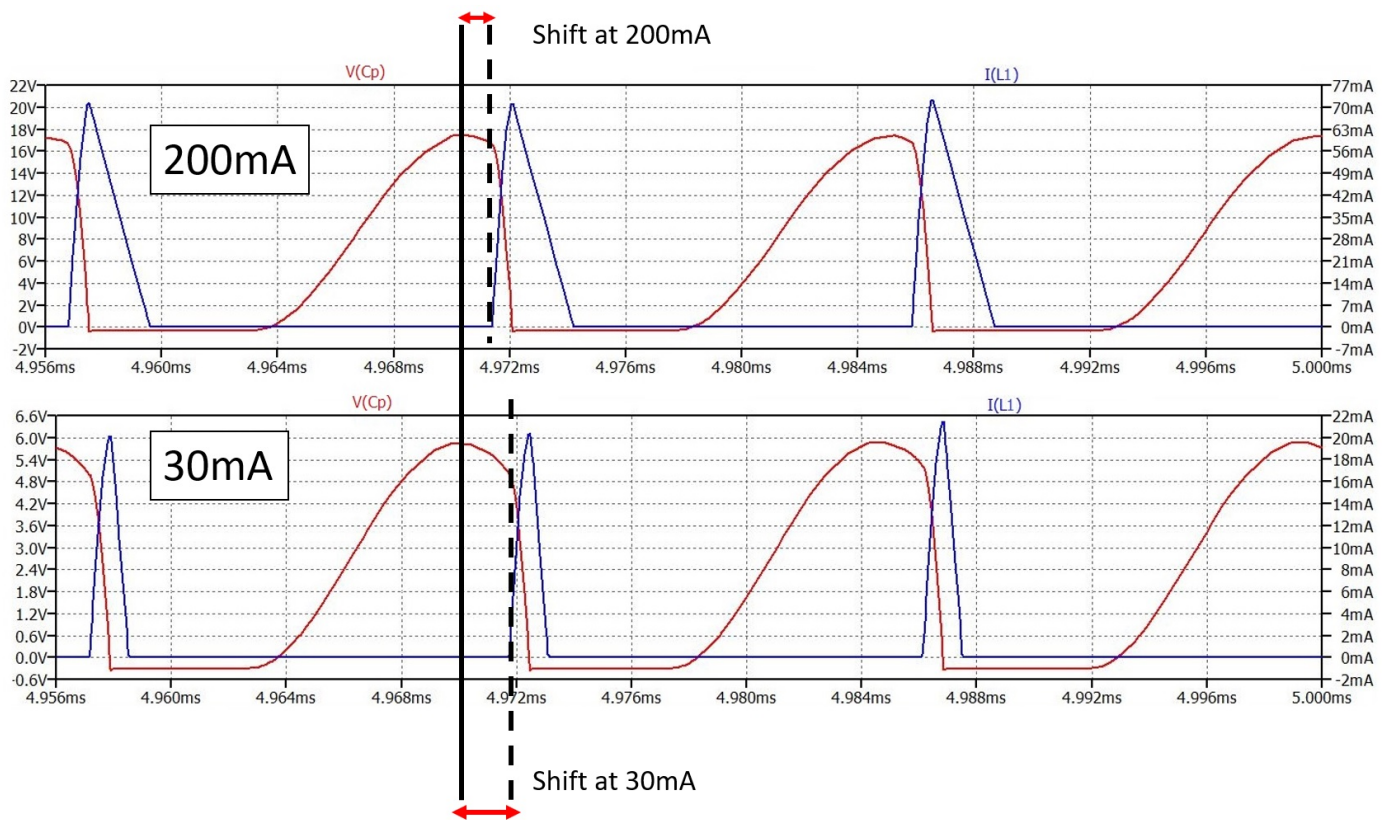


Figure III-24: Waveform of the voltage  $V_{Cp}$  and current in the coil  $L_1$  in the circuit  $USECE_{BJT}$

allows. It would also be very easy to integrate in very low volumes, which is another advantage for implants.

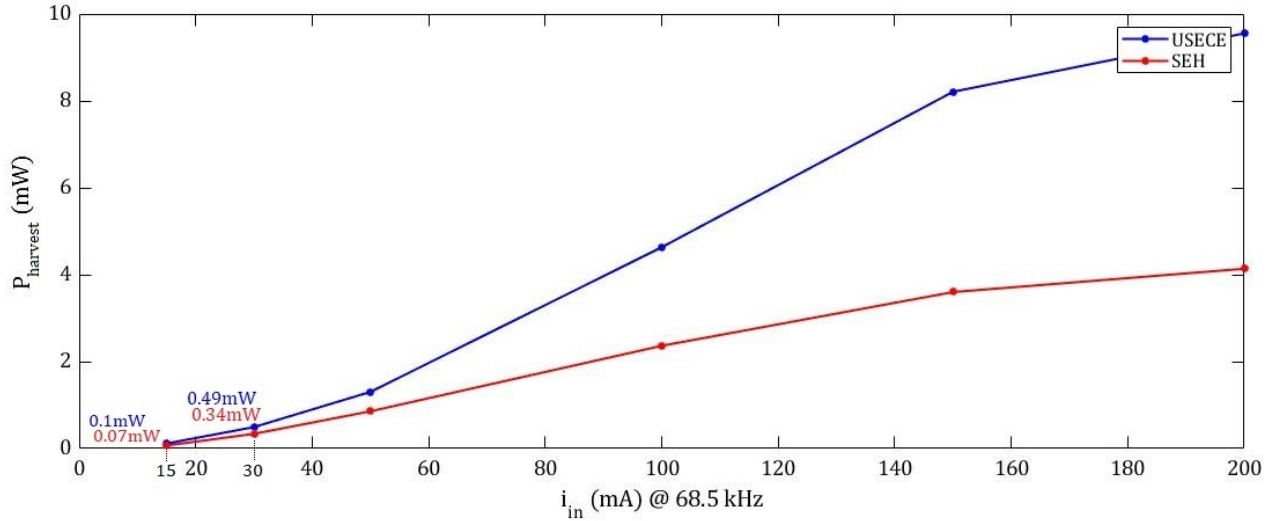


Figure III-25: The harvested power at 50% efficiency

#### 2.2.4.iv Conclusion

Our implementation of USECE technique showed higher performance in term of power conversion efficiency and power ratio (extracted power over  $P_{lim}$ ) compared to SEH circuit. However, this topology implies the use of components as the RS latch, opamps, inverter gate which may consume a large part of the extracted power and thus reduce the efficiency significantly. Therefore, we simulated another USECE implementation which uses only two bipolar transistors (BJT). This circuit showed a good performance in comparison with the other two implementations at high actuation level. The performances of this circuit drops at low actuation level because of the phase shift in the control of the power extraction time. The challenge with this new circuit is to find a BJT transistors that operate at  $70kHz$  and have good rise and fall time, gain and internal resistance to detect correctly the maximum and the zero events.

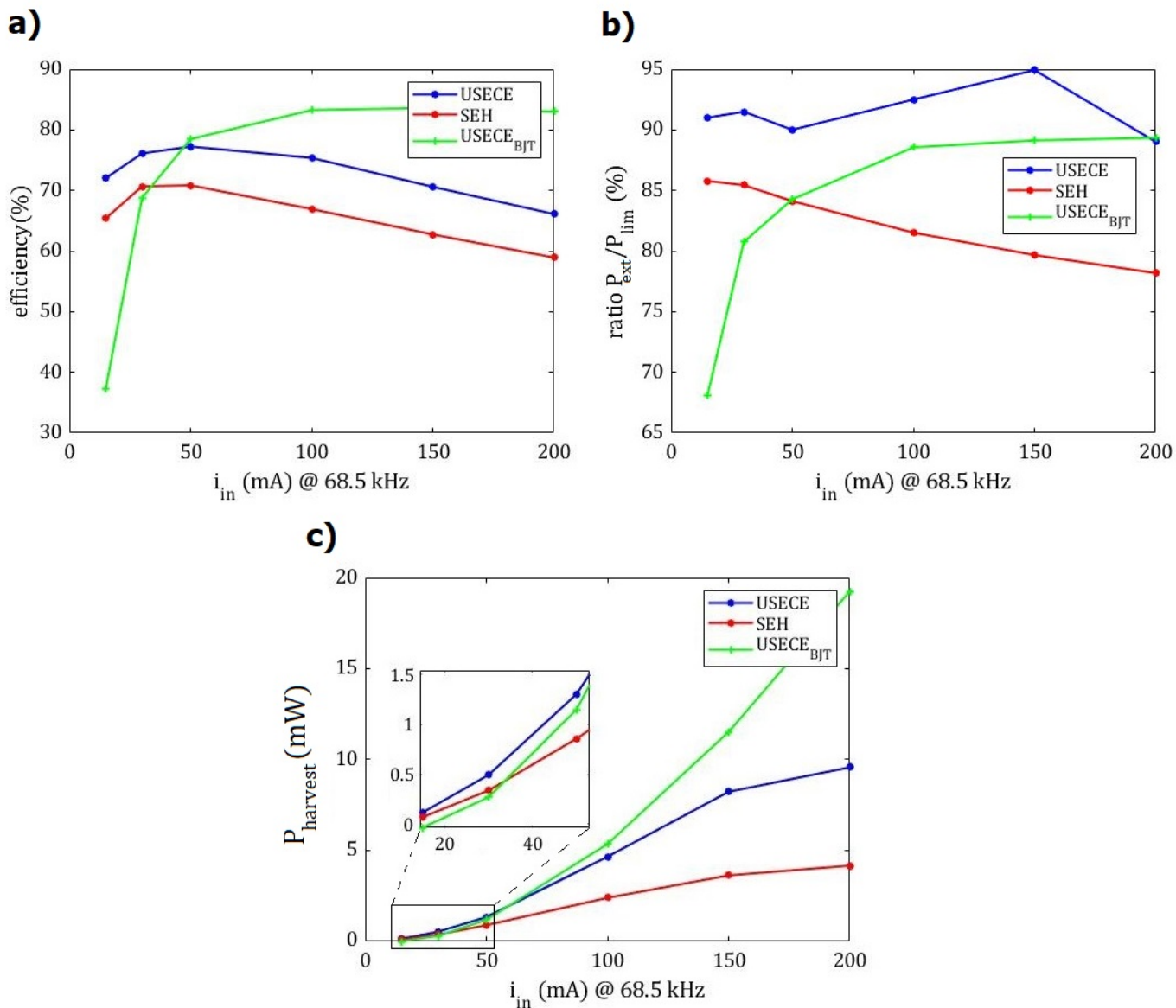


Figure III-26: (a)  $USECE_{BJT}$  efficiency (b) Ratio between the extracted power ( $P_{ext}$ ) and the power limit ( $P_{lim}$ ) (c) harvested power with 50% efficiency for  $USECE$ ,  $SEH$  and  $USECE_{BJT}$

### 3 Conclusion

The study of the power management strategies applied to magnetoelectric transducer have been introduced in this chapter. This study required an equivalent electric circuit that models the physical behaviors of the transducer. The electric model is a series RLC circuit connected to the capacitance  $C_p$  of the piezoelectric element of the ME transducer. The values of the RLC components are not constant. They change with the parameter variation of the magneto-electromechanical model which are governed by the behavioral law presented in chapter II. With this equivalent circuit the impedance matching theory was applied to find the optimal operating point of the system (transducer connected to the load). Thus, the condition to reach the power limit ( $P_{lim}$ ) of the ME transducer was determined and the expression of  $P_{lim}$  and the figure of merit (FoM) was computed. Measurement at low actuation level has shown that the value of  $P_{lim}$  can be reached with an optimal resistive load due to the specific FoM value of our ME sample ( $\approx 2$ ). In fact, the load is not a constant resistance. Thus, as for the piezoelectric transducers, a conditioning circuit between the transducer and the load is required to reach the power limit  $P_{lim}$ . In this purpose, two power management techniques of PE transducer were chosen to be tested with the ME transducer in LTspice. These techniques are the standard energy harvesting (SEH) circuit and the Unipolar Synchronous Electric Charge Extraction (USECE) circuit. The choice of USECE was based on the specific FoM value of our ME sample. The SEH is a standard power management circuits. It is a circuit used to be a reference in comparing the power managements techniques. The first comparison criteria between SEH and USECE was the capacity of the circuit to reach the power limit  $P_{lim}$ . Thus, we computed the ratio between the extracted power and the power limit for different for current value of the excitation coil (between  $15mA$  and  $200mA$ ). The results showed that the ratio for USECE is between 92% and 98%. This ratio is lower for SEH between 79% and 90%. The second criteria was the efficiency of both circuits. To compute the efficiency, we only considered the losses in the coil and in the diodes in the main circuit for both technique. The control circuit was

powered by an external source. With this assumptions, the USECE has shown a better efficiency than the SEH circuit. Despite this advantage of USECE technique over SEH, the main drawback of USECE is that it requires lots of active components (comparator, opamp, RS latch ) which consume a large part of the extracted power or make the implementation of the circuit infeasible. On the other hand, the SEH technique required less number of active components (one opamp or one oscillator). This is the main advantage of SEH technique on the USECE circuit. To overcome the implementation difficulties of the USECE circuit, a simplified version of this technique have been simulated. This simplified USECE circuit (denoted by USECE<sub>BJT</sub>) requires less components. The main components that may consume a lot are the two bipolar transistors that detect the pic and the zero crossing event of the  $C_p$  voltage. At high level of excitation coil current, the USECE<sub>BJT</sub> circuit has shown a better performances in term of efficiency, power ratio and harvested power than the previous circuit (USECE and SEH). At low current level, the efficiency of the circuit has dropped sharply. The reason of this drop is the phase shift in detecting the maximum voltage of the capacitance  $C_p$ . This is one the main drawback of this circuit. However, the high performance of this circuit and the simplicity in its design make it a good candidate.



# Conclusion

In the first chapter, a state of the art on wireless power transfer (WPT) applied to implantable medical devices was presented. The WPT applications were classified based on the energy source. We focused on three types of sources: electromagnetic (EM), acoustic and light sources. Two categories of evaluation criteria have been presented: performance-related criteria and regulation-related criteria. Among the first category, we discussed about the power transfer efficiency and the distance between the emitter and the receiver. Among the second category, we insisted on the regulation on EM field and on the dimension of implants. A comparison between existing techniques was made based on the dimensions of the solution, the operating frequency and the power range. This comparison showed that electromagnetic-based applications are good candidates in terms of power and towards the possible miniaturization of the receiver. However, their main drawback is their relatively high operating frequency especially with respect to existing (and possibly future) regulations. On the other hand, acoustic-based alternatives exist but they operate at significantly lower power levels (unless their dimensions are drastically increased). For light-based applications, the dimensions of the receiver can be very small which is convenient for some specific implants. Besides, there is no frequency restriction for these applications. However, this solution is limited in terms of extracted power in comparison to alternative solutions. For all these reasons, this thesis focussed on a hybrid acousto-electro-mechanical solution using a magnetoelectric (ME) transducer to strike a balance between the specific requirements of implantable medical devices.

The second chapter built an experimentally-validated model of ME transducers.

The model is a system-level model that describes the exact behavior of ME transducer. Such model is simple to use and involves less parameters compared to finite element models. To validate our model, an experimental study was carried out. In this study, two characterizations of our ME samples were realized. Our ME samples are made of a piezoelectric (PE) plate glued to one or two magnetostrictive (MS) plate(s). The first characterization was realized in absence of AC magnetic fields. The parameter identification of a system level piezoelectric model showed that our ME transducer does not behave as a piezoelectric transducer in this condition. In fact, the impedance response of our ME transducer changes when we modify the actuation level changes (voltage level). This involved a variation in the piezoelectric models parameter. In particular, the quality factor of the composite decreases sharply with the voltage level (more than 50% between 0.1V and 1V) which has a strong consequence of the figure-of-merit. This is not expected to happen with PE transducers. The second characterization was realized in presence of AC magnetic field. In this characterization, measurements have been performed first at controlled voltage of the excitation coil. The parameter identification was based on open-circuit measurements combined with measurements on an optimal resistive load. We observed that in presence of a load the quality factor is significantly lower than in open circuit ( $-50\%$ ). As a result, the power predictions based on open-circuit measurements overestimated the extracted power at the resonance (70 times more than the real power). This observation led to conclude that the load should be taken into account when we estimated the parameters. Then, measurement have been performed at regulated output current. It was noticed that, for the current levels achieved in our setup, the most consistent result is obtained when regulating the output current. This is explained by the dependency between the parameters of interest and the mechanical motion. In particular, the evolution of the quality factor proves that the main origin of energy losses in our device lies in a phenomenon that is dependent on the mechanical vibration amplitude.

In the third chapter, we studied power management strategies applied to magnetolectric transducers. Based on the model of the ME transducers, we derived the

expression of the maximum achievable power and the conditions to reach impedance matching. We demonstrated how to adapt the classical system-level figure of merit (FoM) of PE transducers in the context of ME transducers. Under certain circumstances, the extracted power can reach the power limit with an (optimally-chosen) resistive load. However, in practice, autonomous implants require a conditioning circuit which does not actually behave as a resistor. This brought up the study of conditioning circuits that ensure the impedance matching. To this purpose, two power management techniques were chosen to be tested on the ME transducer model. The first is the Unipolar Synchronous Electric Charge Extraction (USECE) technique. The second is the standard energy harvesting (SEH) technique as a point of comparison. Applied to our specific ME transducer, the simulation results showed that the extracted power is closer to optimum with USECE than with SEH. We managed to propose a promising implementation of USECE (called USECE<sub>BJT</sub>) which showed, not only a good level of power extracted at the output of the transducer, but also a better efficiency compared to the SEH circuit, even in an optimal situation where the consumption of the SEH control circuit is partially neglected. We also proposed another implementation of USECE which, ideally, could extract more power from the transducer than the USECE<sub>BJT</sub> circuit. Unfortunately, to achieve this goal, it requires several active components which may consume a large part of the available power and significantly degrade the power conversion efficiency of the circuit.

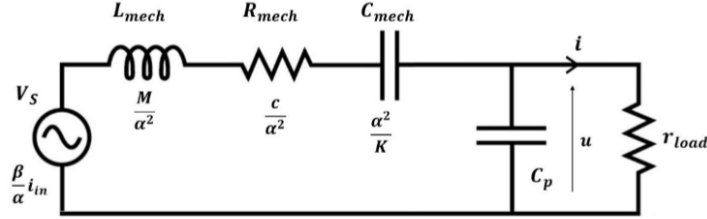
All in all, this thesis detailed and applied a methodology to characterize, design and optimize ME-based power transfer. Our USECE<sub>BJT</sub> circuit has shown promising performances in terms of efficiency, harvested power and simplicity, making it a good candidate to power implants. Future works should focus on the implementation of an application-specific integrated circuit and on the packaging of the whole system, to ensure biocompatibility before it can be experimented on animals and/or humans.

# Appendices

## Appendix 1

### Objective

Here we determine the condition to reach impedance matching in case of resistive load and we compute the expression of the optimal load



### Notations

- For sake of readability, we denote  $L = L_{mech} = \frac{M}{\alpha^2}$ ,  $C = C_{mech} = \frac{\alpha^2}{K}$ ;  $R = R_{mech} = \frac{c}{\alpha^2}$ ;
- $V_S = \frac{\beta}{\alpha} i_{in}$  is a voltage source, the current that passes through  $V_S$  is  $i_{mech}$  and the current in  $C_p$  is  $i_1$
- The output voltage and current are respectively  $u$  and  $i$
- $r_{load}$  is the resistive load
- $Z_{C_p} = \frac{1}{j\omega C_p}$ ,  $Z_L = j\omega L$ ,  $Z_C = \frac{1}{j\omega C}$ ,  $Z_R = R$

### Computation steps

The equation system of this circuit is

$$V_S = V_L + V_R + V_C + V_{rload}$$

$$i_{mech} = i_1 + i$$

We aim to determine the optimal value of the load  $r_{load}$

$$i_{mech} = \frac{V_{rload}}{Z_{C_p}} + \frac{V_{rload}}{r_{load}}$$

$$\frac{i_{mech}}{\frac{1}{Z_{C_p}} + \frac{1}{r_{load}}} = V_{rload}$$

$$\frac{r_{load} Z_{C_p}}{r_{load} + Z_{C_p}} i_{mech} = V_{rload}$$

$$\frac{V_S}{i_{mech}} = Z_L + Z_R + Z_C + \frac{r_{load} Z_{C_p}}{r_{load} + Z_{C_p}}$$

$$\frac{V_S}{i_{mech}} = Z_L + Z_R + Z_C + \frac{r_{load} Z_{C_p} (r_{load} - Z_{C_p})}{(r_{load} + Z_{C_p})(r_{load} - Z_{C_p})}$$

$$\frac{V_S}{i_{mech}} = j\omega L + R + \frac{1}{j\omega C} + \frac{\frac{r_{load}}{j\omega C_p} (r_{load} - \frac{1}{j\omega C_p})}{(r_{load} + \frac{1}{j\omega C_p})(r_{load} - \frac{1}{j\omega C_p})}$$

$$\frac{V_S}{i_{mech}} = j\omega L + R + \frac{1}{j\omega C} + \frac{\frac{r_{load}}{j\omega C_p} (r_{load} + \frac{j}{\omega C_p})}{r_{load}^2 + \frac{1}{\omega^2 C_p^2}}$$

$$\frac{V_S}{i_{mech}} = j\omega L + R + \frac{1}{j\omega C} + \frac{\frac{r_{load}^2}{j\omega C_p} + \frac{r_{load}}{\omega^2 C_p^2}}{r_{load}^2 + \frac{1}{\omega^2 C_p^2}}$$

$$\frac{V_S}{i_{mech}} = (\omega L - \frac{1}{\omega C} - \frac{\frac{r_{load}^2}{\omega C_p}}{r_{load}^2 + \frac{1}{\omega^2 C_p^2}})j + \frac{\frac{r_{load}}{\omega^2 C_p^2}}{r_{load}^2 + \frac{1}{\omega^2 C_p^2}} + R$$

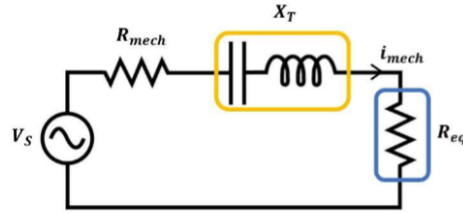
$$\frac{V_S}{i_{mech}} = (\omega L - \frac{1}{\omega C} - \frac{r_{load}^2 \omega C_p}{\omega^2 C_p^2 r_{load}^2 + 1})j + \frac{r_{load}}{\omega^2 C_p^2 r_{load}^2 + 1} + R$$

We denote  $Z_T = \frac{V_S}{i_{mech}}$  the total impedance

$$X_T = \left( \omega L - \frac{1}{\omega C} - \frac{r_{load}^2 \omega C_p}{\omega^2 C_p^2 r_{load}^2 + 1} \right) j$$

$$R_{eq} = \frac{r_{load}}{\omega^2 C_p^2 r_{load}^2 + 1}$$

The equivalent circuit become as follow



The first condition to reach impedance matching is when the real part  $R_{eq}$  that represents the load is equal to the resistance  $R_{mech}$  that represent the damping in the system

$$\frac{r_{load}}{r_{load}^2 \omega^2 C_p^2 + 1} = R$$

The second condition is when the imaginary part in  $Z_T$  be equal to zero

$$\omega L - \frac{1}{\omega C} - \frac{r_{load}^2 \omega C_p}{\omega^2 C_p^2 r_{load}^2 + 1} = 0$$

We recall the expressions of the terms that constitute the figure of merit of the ME transducer:

$$k_m^2 = \frac{\alpha^2}{K C_p} \text{ (the expedient coupling coefficient)}$$

$$Q = \frac{M \omega_0}{c} \text{ (the quality factor)}$$

We can deduce that  $Q = \frac{L}{R} \omega_0$

$$\omega_0 = \sqrt{\frac{K}{M}}$$

$$L = L_{mech} = \frac{M}{\alpha^2}, C = C_{mech} = \frac{\alpha^2}{K}; R = R_{mech} = \frac{c}{\alpha^2};$$

We introduce  $k_m^2$  and Q in the equation system

$$\begin{aligned} \omega L - \frac{1}{\omega k_m^2 C_p} - \frac{r_{load}^2 \omega C_p}{\omega^2 C_p^2 r_{load}^2 + 1} &= 0 \\ \omega \left( \frac{QR}{\omega_0} \right) - \frac{1}{\omega k_m^2 C_p} - \frac{r_{load}^2 \omega C_p}{\omega^2 C_p^2 r_{load}^2 + 1} &= 0 \\ \frac{QR\omega}{\omega_0} - \frac{1}{\omega k_m^2 C_p} - \frac{r_{load}^2 \omega C_p}{\omega^2 C_p^2 r_{load}^2 + 1} &= 0 \\ \frac{Q\omega}{\omega_0} \left( \frac{r_{load}}{r_{load}^2 \omega^2 C_p^2 + 1} \right) - \frac{1}{\omega k_m^2 C_p} - \frac{r_{load}^2 \omega C_p}{\omega^2 C_p^2 r_{load}^2 + 1} &= 0 \\ \frac{Q\omega}{\omega_0} r_{load} - \frac{\omega^2 C_p^2 r_{load}^2 + 1}{\omega k_m^2 C_p} - r_{load}^2 \omega C_p &= 0 \\ \frac{Q\omega}{\omega_0} r_{load} - \frac{\omega^2 C_p^2 r_{load}^2}{\omega k_m^2 C_p} - \frac{1}{\omega k_m^2 C_p} - r_{load}^2 \omega C_p &= 0 \\ \frac{Q\omega^2}{\omega_0} r_{load} k_m^2 C_p - \omega^2 C_p^2 r_{load}^2 - 1 - r_{load}^2 \omega^2 C_p^2 k_m^2 &= 0 \\ r_{load}^2 \omega^2 C_p^2 (1 + k_m^2) - r_{load} k_m^2 Q C_p \frac{\omega^2}{\omega_0} + 1 &= 0 \\ \omega^2 \left( r_{load}^2 C_p^2 (1 + k_m^2) - r_{load} k_m^2 Q C_p \frac{1}{\omega_0} \right) + 1 &= 0 \\ \frac{\omega^2}{\omega_0^2} = \frac{1}{r_{load} k_m^2 Q C_p - \omega_0 r_{load}^2 C_p^2 (1 + k_m^2)} \end{aligned}$$

$$\frac{1}{\omega_0 C_p k_m^2 Q} = \frac{c}{\alpha^2} = R$$

$$\frac{r_{load}}{r_{load}^2 \omega^2 C_p^2 + 1} = R$$

$$r_{load} \omega_0 C_p k_m^2 Q = r_{load}^2 \omega^2 C_p^2 + 1$$

$$r_{load}^2 \omega^2 C_p^2 - r_{load} \omega_0 C_p k_m^2 Q + 1 = 0$$

$$\Delta = \omega_0^2 C_p^2 k_m^4 Q^2 - 4\omega^2 C_p^2$$

$$\Delta = C_p^2(k_m^4 Q^2 \omega_0^2 - 4\omega^2)$$

$$r_{load_1} = \frac{-b - \sqrt{\Delta}}{2a}$$

$$r_{load_2} = \frac{-b + \sqrt{\Delta}}{2a}$$

$$r_{load_1} = \frac{\omega_0 C_p k_m^2 Q - \sqrt{C_p^2(k_m^4 Q^2 \omega_0^2 - 4\omega^2)}}{2\omega^2 C_p^2}$$

$$r_{load_1} = \frac{\omega_0 k_m^2 Q - \sqrt{k_m^4 Q^2 \omega_0^2 - 4\omega^2}}{2\omega^2 C_p}$$

$$r_{load_2} = \frac{\omega_0 k_m^2 Q + \sqrt{k_m^4 Q^2 \omega_0^2 - 4\omega^2}}{2\omega^2 C_p}$$

$$\frac{\omega^2}{\omega_0^2} = \frac{1}{r_{load} k_m^2 Q C_p - \omega_0 r_{load}^2 C_p^2 (1 + k_m^2)}$$

$$\frac{\omega^2}{\omega_0^2} = \frac{1}{\left( \frac{\omega_0 k_m^2 Q + \sqrt{k_m^4 Q^2 \omega_0^2 - 4\omega^2}}{2\omega^2 C_p} \right) k_m^2 Q C_p - \omega_0 \left( \frac{\omega_0 k_m^2 Q + \sqrt{k_m^4 Q^2 \omega_0^2 - 4\omega^2}}{2\omega^2 C_p} \right)^2 C_p^2 (1 + k_m^2)}$$

$$\Omega^2 = \frac{1}{\left( \frac{\omega_0 k_m^2 Q + \sqrt{k_m^4 Q^2 \omega_0^2 - 4\omega^2}}{2\omega^2} \right) k_m^2 Q - \omega_0 \left( \frac{\omega_0 k_m^2 Q + \sqrt{k_m^4 Q^2 \omega_0^2 - 4\omega^2}}{2\omega^2} \right)^2 (1 + k_m^2)}$$

$$\Omega^2 = \frac{1}{\left( \frac{\omega_0 k_m^2 Q + \sqrt{k_m^4 Q^2 \omega_0^2 - 4\omega^2}}{\frac{\omega_0^2}{2 \left( \frac{\omega}{\omega_0} \right)^2}} \right) k_m^2 Q - \omega_0 \left( \frac{\omega_0 k_m^2 Q + \sqrt{k_m^4 Q^2 \omega_0^2 - 4\omega^2}}{\frac{\omega_0^2}{2 \left( \frac{\omega}{\omega_0} \right)^2}} \right)^2 (1 + k_m^2)}$$

$$\Omega^2 = \frac{1}{\left( \frac{\omega_0 k_m^2 Q + \sqrt{k_m^4 Q^2 \omega_0^2 - 4\omega^2}}{\frac{\omega_0^2}{2 \left( \frac{\omega}{\omega_0} \right)^2}} \right) k_m^2 Q - \frac{\omega_0 \left( \frac{\omega_0 k_m^2 Q + \sqrt{k_m^4 Q^2 \omega_0^2 - 4\omega^2}}{\frac{\omega_0^2}{2 \left( \frac{\omega}{\omega_0} \right)^2}} \right)^2}{2 \left( \frac{\omega}{\omega_0} \right)^2 2 \left( \frac{\omega}{\omega_0} \right)^2} (1 + k_m^2)}$$

$$1 = \frac{2\omega_0^2}{\left(\omega_0 k_m^2 Q + \sqrt{k_m^4 Q^2 \omega_0^2 - 4\omega^2}\right) k_m^2 Q - \frac{\omega_0 \left(\omega_0 k_m^2 Q + \sqrt{k_m^4 Q^2 \omega_0^2 - 4\omega^2}\right)^2}{2\omega^2} (1 + k_m^2)}$$

$$1 = \frac{2\omega_0^2}{\left(\omega_0 k_m^2 Q + \sqrt{k_m^4 Q^2 \omega_0^2 - 4\omega^2}\right) k_m^2 Q - \frac{\omega_0 \left(\omega_0 k_m^2 Q + \sqrt{k_m^4 Q^2 \omega_0^2 - 4\omega^2}\right)^2}{2\omega^2} (1 + k_m^2)}$$

$$1 = \frac{2\omega_0^2}{\left(\omega_0 k_m^2 Q + \omega_0 \sqrt{k_m^4 Q^2 - 4\Omega^2}\right) k_m^2 Q - \frac{\omega_0 \left(\omega_0 k_m^2 Q + \omega_0 \sqrt{k_m^4 Q^2 - 4\Omega^2}\right)^2}{2\omega^2} (1 + k_m^2)}$$

$$1 = \frac{2\omega_0^2}{\left(\omega_0 k_m^2 Q + \omega_0 \sqrt{k_m^4 Q^2 - 4\Omega^2}\right) k_m^2 Q - \frac{\left(k_m^2 Q + \sqrt{k_m^4 Q^2 - 4\Omega^2}\right)^2}{2\Omega^2} (1 + k_m^2)}$$

$$1 = \frac{2\omega_0^2}{2\Omega^2 \left(\omega_0 k_m^2 Q + \omega_0 \sqrt{k_m^4 Q^2 - 4\Omega^2}\right) k_m^2 Q - \left(k_m^2 Q + \sqrt{k_m^4 Q^2 - 4\Omega^2}\right)^2 (1 + k_m^2)}$$

The solution of the following equation gives the optimal frequencies in term of the model's parameters

$$2\Omega^2 \left(\omega_0 k_m^2 Q + \omega_0 \sqrt{k_m^4 Q^2 - 4\Omega^2}\right) k_m^2 Q - \left(k_m^2 Q + \sqrt{k_m^4 Q^2 - 4\Omega^2}\right)^2 (1 + k_m^2) = 2\omega_0^2$$

Then we resolve the following equation to obtain the optimal values of the resistive loads

$$r_{load}^2 \omega^2 C_p^2 (1 + k_m^2) - r_{load} k_m^2 Q C_p \omega_0 + 1 = 0$$

To find the solution we compute the discriminant

$$\Delta = b^2 - 4ac = k_m^4 Q^2 C_p^2 \omega_0^2 - 4(\omega^2 C_p^2 (1 + k_m^2))$$

$$\Delta = b^2 - 4ac = k_m^4 Q^2 C_p^2 \omega_0^2 - 4\omega^2 C_p^2 (1 + k_m^2)$$

$$\Delta = b^2 - 4ac = C_p^2 (\omega_0^2 k_m^4 Q^2 - 4\omega^2 (1 + k_m^2))$$

In general,  $k_m^2 \ll 1$  so  $\Delta = b^2 - 4ac = k_m^4 Q^2 C_p^2 \omega_0^2 - 4\omega^2 C_p^2 = C_p^2 (k_m^4 Q^2 \omega_0^2 - 4\omega^2)$

### Results

When  $\omega$  and  $\omega_0$  are close we have a solution when  $\Delta \geq 0$ , in this case we have a condition on the figure of merit  $k_m^2 Q \geq 2$

When this condition is fulfilled, two value of optimal loads exist the expressions of the

$$r_{load1} = \frac{-b - \sqrt{\Delta}}{2a} = \frac{k_m^2 Q C_p \omega_0 - \sqrt{C_p^2 \omega_0^2 (k_m^4 Q^2 - 4(1 + k_m^2))}}{2\omega_0^2 C_p^2 (1 + k_m^2)}$$

$$r_{load2} = \frac{-b + \sqrt{\Delta}}{2a} = \frac{k_m^2 Q C_p \omega_0 + \sqrt{C_p^2 \omega_0^2 (k_m^4 Q^2 - 4(1 + k_m^2))}}{2\omega_0^2 C_p^2 (1 + k_m^2)}$$

$$r_{load_1} = \frac{-b - \sqrt{\Delta}}{2a} = \frac{k_m^2 Q - \sqrt{(k_m^4 Q^2 - 4(1 + k_m^2))}}{2C_p \omega_0 (1 + k_m^2)}$$

$$r_{load_1} = \frac{-b - \sqrt{\Delta}}{2a} = \frac{k_m^2 Q + \sqrt{(k_m^4 Q^2 - 4(1 + k_m^2))}}{2C_p \omega_0 (1 + k_m^2)}$$

## Appendix 2

### Objective

Here we determine the value of the components used in the standard energy harvesting circuit (SEH).

### Notation

$r_{optimal}$  : is the value of the optimal resistive load

$f_{op}$  : is the operating point frequency near to the system resonant frequency

$C_p$ : is the piezoelectric layer capacitance

$L$ : is the inductor coil of the DC-DC buck boost converter

### Computation steps

Here are the steps required to determine the components for the SEH circuit

- In this circuit we need an oscillator to generate a pulse width modulation signal to control the N-channel Mosfet of the DC-DC buck boost converter. The switching frequency and the duty cycle of the oscillator are chosen in a way to ensure that the converter works in a discontinuous current mode (DCM). In the simulation, the switching frequency  $f_{switching} = 21.86 \text{ kHz}$  and the duty cycle  $d = 0.1467$  were chosen for this purpose.
- The optimal load for the specific operating point tested in the simulation can be computed as follow:  $R_{optimal} = \frac{6.087}{2\pi f_{op} \times C_p} = 7k\Omega$
- From the optimal resistance, the switching frequency and the duty cycle we deduce the inductance value using the following formula:  $L = \frac{R_{optimal} \times d^2}{2f_{switching}} = 3.5mH$

# List of Figures

-1	Deux échantillons de transducteurs magnétoélectriques étudiés dans cette thèse (Vert clair : partie piezoélectrique - foncé: partie magnétostrictive) .	9
-2	Modèles du niveau "système" (haut: transducteur piézoélectrique , bas: transducteur magnétoélectrique) . . . . .	10
-3	Caractérisation en absence du champ magnétique. Haut: mesures d'impédance de l'élément piézoélectrique (PZT) et du transducteur ME (PZT/TerfD). Bas: résultat de l'identification des paramètres de l'élément piézoélectrique et du transducteur ME en utilisant le modèle classique) . . . . .	11
-4	Caractérisation en présence du champs magnétique (haut: banc expérimentale , bas: courbe de la fonctionde transfert à un niveau d'actionement fixe avec plusieurs résistances . . . . .	13
-5	Circuit électrique équivalent du transducteur magnétoélectrique . . . . .	14
-6	Haut: schéma du circuit SEH, bas: schéma du circuit USECE . . . . .	15
I-1	Examples of wireless power transfer methods. (A) WPT with radio-frequency waves, (B) solar radiation in optical WPT, (C) WPT using ultrasonic waves, (D) capacitive power transfer, (E) tightly coupled inductive power transfer, and (F) loosely coupled resonant inductive power transfer [2] . . . . .	22
I-2	Left: Reference levels for exposure to time varying (a) magnetic fields (b) electric fields from 1Hz to 100kHz [5]. Right: Reference levels for time averaged exposures of 6 min, to electromagnetic fields from 100 kHz to 300 GHz for the two categories, (c) general public (d) occupational [3] . . . . .	25
I-3	Impact of the distance d on the power transimission efficiency of 2-coils (blue) and 4-coils (red) IPT systems (r is the coil radius) [16] . . . . .	28

I-4	The 4-coil WPT system. (a) Physical structure. (b) Lumped circuit model [17] . . . . .	29
I-5	Photograph of the proposed prototype including the energy transmission coils. [21] . . . . .	31
I-6	(a) Schematic illustrations of a Mg coil as the receiver and a rotating magnet as a transmitter for wireless power transfer. b) Schematic diagram of the working principles. [24] . . . . .	32
I-7	Typical structure of a capacitive power transfer (CPT) system [28] . . . . .	33
I-8	Experimental components used for the capacitive power transfer setup a) The transmitting plate b) the receiver: two 40 mm long stents [30] . . . . .	34
I-9	Explanation of the thin tube-shape implant concept. When the tube is exposed to an electric field generated by a pair of external electrodes, the power will draw to the implant by the internal electrodes located at its opposite ends. [32] . . . . .	35
I-10	Single diode equivalent circuit [38] . . . . .	36
I-11	Concept of photovoltaic retinal implant based on NIR-sensitive OPDs. The image captured by a head-mounted camera is processed by a portable computer and projected onto the subretinal implant via a near-to-eye projection system using pulsed NIR light. The OPD array converts incoming light into pulsed photocurrent that is delivered to nearby nerve cells by stimulating microelectrodes [40] . . . . .	37
I-12	Layers of human skin [41] . . . . .	37
I-13	Schematic representation of the longitudinal direct (a) converse (b) piezoelectric effect [53]. . . . .	39
I-14	Perovskite PZT unit cell. (a) PZT unit cell in the symmetric cubic state above the Curie temperature. (b) Tetragonally distorted unit cell below the Curie temperature [54]. . . . .	40
I-15	Piezoelectric domains in piezoelectric materials. (a) Randomly oriented domains, Domains during (b) and after (c) the poling process. [54] . . . . .	40

I-16	Schematic diagram of ferroelectric hysteresis graph. Here the definitions are as follows; $E_c$ : coercive field; $P_s$ : saturation polarization; $P_r$ : remanent polarization. The arrows indicate direction of polarization for dipoles in a domain. [55] . . . . .	41
I-17	Circuit representation of the piezoelectric generator. (Note that node 1 is used in the derivation of equation [56]). . . . .	42
I-18	Schematic of acoustic power transfer technology based on piezoelectric transducers [47]. . . . .	42
I-19	(a) Transmitting transducer equivalent circuit. (b) Pickup transducer equivalent circuit. [57] . . . . .	43
I-20	Representation of near-field and far-field regions of an acoustic wave generated by TX and incident on RX [1]. . . . .	44
I-21	Summary of the review on APT applications [47]. . . . .	44
I-22	Graphical comparison between different application for 4 wireless power techniques based on the power level and the surface of the receiver used in the application . . . . .	46
I-23	Wireless power transfer used in a nerve stimulator [70] . . . . .	48
I-24	Range of power requirements of example implantable medical devices [71] .	49
I-25	Various applications of Magnetolectric composite [74] . . . . .	50
I-26	Schematic of (a) 0-3, (b) 2-2, and (c) 1-3 composite nanostructures [74] . .	50
I-27	Change of shape for positive or negative . . . . .	51
I-28	(a) Magnetisation of magnetostrictive material with magnetic field $H$ approximately proportional to the current $i$ that passes through a solenoid (b) the rotation of the domains that change the sample's length (c) $\Delta L/L$ at different level of magnetic field $H$ [75] . . . . .	52
I-29	Magnetic field limitation when using wireless power transfer solutions : RFID (125kHz-134kHz) , RFID(13.56MHz) and our ME transducer (65 – 75kHz). Data taken from the guidelines of the International Commission on Non-Ionizing Radiation Protection (2014) . . . . .	53

II-1	Main polarization and magnetization configurations of magnetoelectric transducer [97] . . . . .	60
II-2	"P51/2×TerfD" sample: magnetoelectric composite transducer (light green : piezoelectric layer - dark: magnetostrictive layer) . . . . .	60
II-3	Magnetoelectric sample: a piezoelectric layer (light green) in the middle and two magnetostrictive layers (Dark) each one is glued at one side of the piezoelectric plate. . . . .	61
II-4	Electromechanical model of a linear electromechanical resonator (where x is the displacement) . . . . .	62
II-5	The sample holder ((a): picture, (b): schematic) "M" denotes a mechanical contact and "E" an electrical contact. "PE" plate in green and "MS" plate in black . . . . .	63
II-6	Measurements (cross +) performed in the absence of a AC magnetic field and corresponding fits (solid lines). Admittance of the "P sample" (left) and "P-T sample"(right) for several voltage levels. In the case of P sample all the curves at different actuation levels are superposed. Thus we show only one curve. . . . .	64
II-7	Parameters estimated from the electromechanical model . . . . .	66
II-8	Evolution of the FOM. . . . .	66
II-9	Experimental setup test bench consisting of: an excitation coil (100 turns, 18mm of diameter, 0.1mm∅wire), a sliding rail to adjust the permanent magnet position and to reach the optimal static magnetic fields $40 \times 10^3 (A/m)$ . The ME transducer is inside the sample holder surrounded by the coil. . .	68
II-10	Schematic of the experimental setup. . . . .	68
II-11	Magneto-electromechanical model of the ME transducer connected to a resistive load [103] . . . . .	70
II-12	The fitting results of $u/u_{in}$ (input voltage level $3V_{rms}$ open circuit case) .	72
II-13	Estimated parameters of the ME model for open-circuit (OC) and with $1.2k\Omega$ resistive load (LD) case (left: quality factor $Q$ and right: the natural frequency $f_0$ ) . . . . .	73

II-14	Measured transferred power (plus sign points + ), estimated transferred power based on open-circuit (OC) characterization (dashed line - - ), theoretical fit of the transferred power based on with load (LD) characterization (continuous line). Two input voltage levels are presented ( $0.5V_{rms}$ and $3V_{rms}$ ). . . . .	74
II-15	Admittance measurements ( $u_1 = 1.5V$ ). . . . .	77
II-16	Magneto-electromechanical model of the ME transducer. . . . .	78
II-17	Model identification: experimental frequency responses $u_1/i_0$ for a regulated amplitude of the output current (left: $i_1 = 0.28mA$ , middle: $i_1 = 1.41mA$ , right: $i_1 = 2.55mA$ ). Crosses: measurements. Solid lines: model. From blue to black: $r_{load} = 270\Omega$ to $r_{load} = 2200\Omega$ . . . . .	82
II-18	System parameters as a function of the output current $i_1$ for several resistive loads. Upper left: quality factor $Q$ , Upper right: natural frequency $f_0$ , lower left: expedient magnetoelectric coefficient $B_m$ (Dots : Measurements. Solid lines: Fits). . . . .	85
II-19	Model validation: experimental frequency responses $i_1$ for a regulated amplitude of the input current (left: $i_0 = 11.3mA$ , middle: $i_0 = 19.8mA$ , right: $i_0 = 35.4mA$ ). Dots: measurements. Solid lines: model. From blue to black: $r_{load} = 270\Omega$ to $r_{load} = 2200\Omega$ . . . . .	86
III-1	Equivalent electric circuit of ME transducer . . . . .	91
III-2	Lumped circuit representation of the impedance matching between the ME transducer and a resistive load ( $r_{load}$ ) using an inductor $L_p$ connected in parallel to the capacitance $C_p$ at $f = f_0$ ( $f_0$ is the short circuit frequency) .	93
III-3	Power vs. frequency responses for a regulated amplitude of the input current (left: $i_0 = 11.3mA$ , middle: $i_0 = 19.8mA$ , right: $i_0 = 35.4mA$ ). Dots : Experimental measurements. Solid lines : Responses reconstructed based on the characterization at regulated output currents. Dashed lines : Responses expected from a linear model. Dash-dot line (gray): power limit of the ME transducer. . . . .	99

III-4	Summary of the existing strategies, topologies, architectures and techniques of piezoelectric harvesting circuits [102] . . . . .	100
III-5	Power flow in the system (transducer, conditioning circuit and load). $\eta$ is the power conversion efficiency of the management circuit only. . . . .	101
III-6	Optimal values of the figure-of-merit $k_m^2 Q$ for piezoelectric harvesting techniques . . . . .	102
III-7	The dependency of $k_m^2 Q$ on the output current $i_1$ of the ME transducer sample	102
III-8	Ratio between the extracted power and the power limit for USECE and SEH circuits based on the results given in [119] and [120] . . . . .	103
III-9	Topology of 3 stage SEH circuit . . . . .	104
III-10	SEH circuit implementation in LTspice $L_1[3.5mH, 40\Omega]$ . . . . .	106
III-11A	A comparator-based relaxation oscillator in the control circuit of the SEH technique . . . . .	106
III-12	The waveform of the voltage and the current of the coil $L_1$ in discontinuous current mode. The green waveform represents the control signal of the mosfet $M1$ . . . . .	107
III-13	Topology of the SECE technique . . . . .	108
III-14	Waveform of the voltage across the piezoelectric element $V_{C_p}$ in the USECE technique. . . . .	108
III-15	USECE circuit implementation in LTspice ( $L_1[3.5mH, 40\Omega]$ ) . . . . .	110
III-16	Control and power supply circuits of the USECE technique. . . . .	110
III-17	Examples of RS latch circuit topologies: a) a system representation of the RS latch with two NOR , in b) a detailed implementation of an RS-latch with 4 N channel mosfet and 4 P-channel mosfet. . . . .	111
III-18	Truth table of the RS latch . $Q_n$ and $Q_{n-1}$ are the current and previous state of the output $Q$ . . . . .	112
III-19	Top: Voltage waveforms of the USECE circuit: $V(set)$ , $V(reset)$ , $V(Q)$ of the RS latch filp-flop, voltage $V(C_p)$ of the piezoelectric capacitance $C_p$ and signal $V(dc)$ which represents the maximum of $V(C_p)$ . Down: Timing diagram of the RS signals Q, set and reset. . . . .	113

III-20	Ratio between the extracted power ( $P_{ext}$ ) and the power limit ( $P_{lim}$ ) as a function of: the level of output current $i_1$ (left) and the extracted power (right) of both USECE and SEH circuits . . . . .	113
III-21	Ratio between the extracted power ( $P_{ext}$ ) and the power limit ( $P_{lim}$ ) for different values of figure-of-merit $k_m^2 Q$ of both USECE and SEH techniques	114
III-22	The efficiency (%) of the USECE and SEH circuit . . . . .	115
III-23	$USECE_{BJT}$ bipolar transistor circuit: $Q_1$ and $Q_2$ are ideal bipolar transistors in LTspice, $D_s$ are schottky diodes ( $V_{threshold} = 0.3V$ ), $V_1$ represents a load as a battery with constant voltage $3V$ , $L_1 = 0.1mH$ and $C_4 = 100pF$ .	116
III-24	Waveform of the voltage $V_{Cp}$ and current in the coil $L_1$ in the circuit $USECE_{BJT}$ . . . . .	117
III-25	The harvested power at 50% efficiency . . . . .	118
III-26	(a) $USECE_{BJT}$ efficiency (b) Ratio between the extracted power ( $P_{ext}$ ) and the power limit ( $P_{lim}$ ) (c) harvested power with 50% efficiency for $USECE$ , $SEH$ and $USECE_{BJT}$ . . . . .	119

# List of Tables

I.1	Examples on the inductive power transfer application . . . . .	31
I.2	Examples of capacitive power transfer . . . . .	35
I.3	Examples on photovoltaic power transfer . . . . .	38
I.4	Examples of acoustic power transfer . . . . .	45
I.5	Pacemaker specification . . . . .	49
II.1	Normalized variables of the piezoelectric model . . . . .	64
II.2	Notations . . . . .	71
II.3	System-level parameters . . . . .	71
II.4	Notations . . . . .	80
II.5	Empirical law of $Q$ . . . . .	83
II.6	Empirical law of $f_0^2$ . . . . .	83
II.7	Empirical law of $B_m$ . . . . .	84



# Bibliography

- [1] Sadeque Reza Khan et al. “Wireless power transfer techniques for implantable medical devices: A review”. In: *Sensors* 20.12 (2020), p. 3487.
- [2] Mohammad Etemadrezaei. “Wireless Power Transfer”. In: *Power Electronics Handbook*. Elsevier, 2018, pp. 711–722.
- [3] International Commission on Non-Ionizing Radiation Protection et al. “Guidelines for limiting exposure to electromagnetic fields (100 kHz to 300 GHz)”. In: *Health physics* 118.5 (2020), pp. 483–524.
- [4] International Commission on Non-Ionizing Radiation Protection et al. “Gaps in knowledge relevant to the “Guidelines for limiting exposure to time-varying electric and magnetic fields (1 Hz–100 kHz)””. In: *Health physics* 118.5 (2020), pp. 533–542.
- [5] International Commission on Non-Ionizing Radiation Protection et al. “Guidelines for limiting exposure to time-varying electric and magnetic fields (1 Hz to 100 kHz)”. In: *Health physics* 99.6 (2010), pp. 818–836.
- [6] Jinwook Kim et al. “Optimal design of a wireless power transfer system with multiple self-resonators for an LED TV”. In: *IEEE Transactions on Consumer Electronics* 58.3 (2012), pp. 775–780.
- [7] Reid R Harrison. “Designing efficient inductive power links for implantable devices”. In: *2007 IEEE International Symposium on Circuits and Systems*. IEEE. 2007, pp. 2080–2083.
- [8] Minseok Han, Ji-Min Kim, and Hoon Sohn. “Dual-mode wireless power transfer module for smartphone application”. In: *2015 IEEE International Symposium on Antennas and Propagation & USNC/URSI National Radio Science Meeting*. IEEE. 2015, pp. 111–112.
- [9] Grant A Covic and John T Boys. “Inductive power transfer”. In: *Proceedings of the IEEE* 101.6 (2013), pp. 1276–1289.
- [10] Fawwaz T Ulaby, Eric Michielssen, and Umberto Ravaioli. *Fundamentals of applied electromagnetics 6e*. Prentice Hall, 2001.
- [11] Jiejian Dai and Daniel C Ludois. “A survey of wireless power transfer and a critical comparison of inductive and capacitive coupling for small gap applications”. In: *IEEE Transactions on Power Electronics* 30.11 (2015), pp. 6017–6029.
- [12] Siqi Li and Chunting Chris Mi. “Wireless power transfer for electric vehicle applications”. In: *IEEE journal of emerging and selected topics in power electronics* 3.1 (2014), pp. 4–17.
- [13] Trong-Duy Nguyen et al. “Feasibility study on bipolar pads for efficient wireless power chargers”. In: *2014 IEEE Applied Power Electronics Conference and Exposition-APEC 2014*. IEEE. 2014, pp. 1676–1682.
- [14] Alicia Triviño, José M González-González, and José A Aguado. “Wireless Power Transfer Technologies Applied to Electric Vehicles: A Review”. In: *Energies* 14.6 (2021), p. 1547.

- [15] Andre Kurs et al. “Wireless power transfer via strongly coupled magnetic resonances”. In: *science* 317.5834 (2007), pp. 83–86.
- [16] Zhen Zhang et al. “Wireless power transfer—An overview”. In: *IEEE Transactions on Industrial Electronics* 66.2 (2018), pp. 1044–1058.
- [17] Shuo Wang and Dawei Gao. “Power transfer efficiency analysis of the 4-coil wireless power transfer system based on circuit theory and coupled-mode theory”. In: *2016 IEEE 11th Conference on Industrial Electronics and Applications (ICIEA)*. IEEE. 2016, pp. 1230–1234.
- [18] Zhen Ning Low et al. “Design and test of a high-power high-efficiency loosely coupled planar wireless power transfer system”. In: *IEEE transactions on industrial electronics* 56.5 (2008), pp. 1801–1812.
- [19] Jahyun Koo et al. “Wireless bioresorbable electronic system enables sustained nonpharmacological neuroregenerative therapy”. In: *Nature medicine* 24.12 (2018), pp. 1830–1836.
- [20] Meysam Zargham and P Glenn Gulak. “Fully Integrated On-Chip Coil in 0.13  $\mu$  CMOS for Wireless Power Transfer Through Biological Media”. In: *IEEE transactions on biomedical circuits and systems* 9.2 (2014), pp. 259–271.
- [21] Oliver Knecht, Roman Bosshard, and Johann W Kolar. “High-efficiency transcutaneous energy transfer for implantable mechanical heart support systems”. In: *IEEE Transactions on Power Electronics* 30.11 (2015), pp. 6221–6236.
- [22] Amir Javan-Khoshkholgh, Joseph C Sassoon, and Aydin Farajidavar. “A Wireless Rechargeable Implantable System for Monitoring and Pacing the Gut in Small Animals”. In: *2019 IEEE Biomedical Circuits and Systems Conference (BioCAS)*. IEEE. 2019, pp. 1–4.
- [23] Hamed Rahmani and Aydin Babakhani. “A dual-mode RF power harvesting system with an on-chip coil in 180-nm SOI CMOS for millimeter-sized biomedical implants”. In: *IEEE Transactions on Microwave Theory and Techniques* 67.1 (2018), pp. 414–428.
- [24] Qinglei Guo et al. “A Bioresorbable Magnetically Coupled System for Low-Frequency Wireless Power Transfer”. In: *Advanced Functional Materials* 29.46 (2019), p. 1905451.
- [25] Hao Jiang et al. “A low-frequency versatile wireless power transfer technology for biomedical implants”. In: *IEEE transactions on biomedical circuits and systems* 7.4 (2012), pp. 526–535.
- [26] Loulin Huang and Aiguo Patrick Hu. “Defining the mutual coupling of capacitive power transfer for wireless power transfer”. In: *Electronics Letters* 51.22 (2015), pp. 1806–1807.
- [27] JT Boys, GA Covic, and GAJ Elliott. “Pick-up transformer for ICPT applications”. In: *Electronics Letters* 38.21 (2002), pp. 1276–1278.
- [28] Fei Lu, Hua Zhang, and Chris Mi. “A review on the recent development of capacitive wireless power transfer technology”. In: *Energies* 10.11 (2017), p. 1752.
- [29] Rangarajan Jegadeesan et al. “Wireless power delivery to flexible subcutaneous implants using capacitive coupling”. In: *IEEE Transactions on Microwave Theory and Techniques* 65.1 (2016), pp. 280–292.
- [30] Ammar Aldaoud et al. “Near-field wireless power transfer to stent-based biomedical implants”. In: *IEEE Journal of Electromagnetics, RF and Microwaves in Medicine and Biology* 2.3 (2018), pp. 193–200.
- [31] Antoni Ivorra, Laura Becerra-Fajardo, and Quim Castellvié. “In vivo demonstration of injectable microstimulators based on charge-balanced rectification of epidermically applied currents”. In: *Journal of neural engineering* 12.6 (2015), p. 066010.

- [32] Marc Tudela-Pi et al. “Power transfer by volume conduction: In vitro validated analytical models predict DC powers above 1 mW in injectable implants”. In: *IEEE Access* 8 (2020), pp. 37808–37820.
- [33] Reza Sedehi et al. “A wireless power method for deeply implanted biomedical devices via capacitively coupled conductive power transfer”. In: *IEEE Transactions on Power Electronics* 36.2 (2020), pp. 1870–1882.
- [34] Adolf Goetzberger, Christopher Hebling, and Hans-Werner Schock. “Photovoltaic materials, history, status and outlook”. In: *Materials Science and Engineering: R: Reports* 40.1 (2003), pp. 1–46.
- [35] Alan Fahrenbruch and Richard Bube. *Fundamentals of solar cells: photovoltaic solar energy conversion*. Elsevier, 2012.
- [36] Nominoe Lorrière et al. “Photovoltaic solar cells for outdoor LiFi communications”. In: *Journal of Lightwave Technology* 38.15 (2020), pp. 3822–3831.
- [37] Jinwei Zhao et al. “Self-Powered Implantable Medical Devices: Photovoltaic Energy Harvesting Review”. In: *Advanced healthcare materials* 9.17 (2020), p. 2000779.
- [38] Nicola Pearsall. *The performance of photovoltaic (PV) systems: modelling, measurement and assessment*. Woodhead Publishing, 2016.
- [39] Antonio Luque and Steven Hegedus. *Handbook of photovoltaic science and engineering*. John Wiley & Sons, 2011.
- [40] Giulio Simone et al. “Near-infrared tandem organic photodiodes for future application in artificial retinal implants”. In: *Advanced Materials* 30.51 (2018), p. 1804678.
- [41] Letizia Ventrelli, Lucanos Marsilio Strambini, and Giuseppe Barillaro. “Microneedles for transdermal biosensing: current picture and future direction”. In: *Advanced healthcare materials* 4.17 (2015), pp. 2606–2640.
- [42] Kwangsun Song et al. “Subdermal flexible solar cell arrays for powering medical electronic implants”. In: *Advanced healthcare materials* 5.13 (2016), pp. 1572–1580.
- [43] Jinwei Zhao et al. “Photovoltaic power harvesting technologies in biomedical implantable devices considering the optimal location”. In: *IEEE Journal of Electromagnetics, RF and Microwaves in Medicine and Biology* 4.2 (2019), pp. 148–155.
- [44] Luyao Lu et al. “Biodegradable monocrystalline silicon photovoltaic microcells as power supplies for transient biomedical implants”. In: *Advanced Energy Materials* 8.16 (2018), p. 1703035.
- [45] Juho Kim et al. “Active photonic wireless power transfer into live tissues”. In: *Proceedings of the National Academy of Sciences* 117.29 (2020), pp. 16856–16863.
- [46] Kenji Uchino. *Advanced piezoelectric materials: Science and technology*. Woodhead Publishing, 2017.
- [47] Md Rabiul Awal et al. “State-of-the-art developments of acoustic energy transfer”. In: *International Journal of Antennas and Propagation* 2016 (2016).
- [48] Alper Erturk and Daniel J Inman. *Piezoelectric energy harvesting*. John Wiley & Sons, 2011.
- [49] Claudia Steinem and Andreas Janshoff. *Piezoelectric sensors*. Vol. 5. Springer Science & Business Media, 2007.
- [50] Kenji Uchino. *Piezoelectric actuators and ultrasonic motors*. Vol. 1. Springer Science & Business Media, 1996.
- [51] Shunta Iguchi, Takayasu Sakurai, and Makoto Takamiya. “A low-power CMOS crystal oscillator using a stacked-amplifier architecture”. In: *IEEE Journal of Solid-State Circuits* 52.11 (2017), pp. 3006–3017.

- [52] Ahmad Safari and E Koray Akdogan. *Piezoelectric and acoustic materials for transducer applications*. Springer Science & Business Media, 2008.
- [53] Linsheng Huo et al. “Smart washer—A piezoceramic-based transducer to monitor looseness of bolted connection”. In: *Smart Materials and Structures* 26.2 (2017), p. 025033.
- [54] Shashank Priya et al. “A review on piezoelectric energy harvesting: materials, methods, and circuits”. In: *Energy Harvesting and Systems* 4.1 (2017), pp. 3–39.
- [55] Anderson D Prewitt and Jacob L Jones. “Effects of the poling process on piezoelectric properties in lead zirconate titanate ceramics”. In: *Ferroelectrics* 419.1 (2011), pp. 39–45.
- [56] Shad Roundy and Paul K Wright. “A piezoelectric vibration based generator for wireless electronics”. In: *Smart Materials and structures* 13.5 (2004), p. 1131.
- [57] Ho Fai Leung, Brett J Willis, and Aiguo Patrick Hu. “Wireless electric power transfer based on Acoustic Energy through conductive media”. In: *2014 9th IEEE Conference on Industrial Electronics and Applications*. IEEE, 2014, pp. 1555–1560.
- [58] Hamid Basaeri, David B Christensen, and Shad Roundy. “A review of acoustic power transfer for bio-medical implants”. In: *Smart Materials and Structures* 25.12 (2016), p. 123001.
- [59] Ayodele Sanni, Antonio Vilches, and Christofer Toumazou. “Inductive and ultrasonic multi-tier interface for low-power, deeply implantable medical devices”. In: *IEEE transactions on biomedical circuits and systems* 6.4 (2012), pp. 297–308.
- [60] Francesco Mazzilli, Cyril Lafon, and Catherine Dehollain. “A 10.5 cm ultrasound link for deep implanted medical devices”. In: *IEEE transactions on biomedical circuits and systems* 8.5 (2014), pp. 738–750.
- [61] Miao Meng and Mehdi Kiani. “Design and optimization of ultrasonic wireless power transmission links for millimeter-sized biomedical implants”. In: *IEEE transactions on biomedical circuits and systems* 11.1 (2016), pp. 98–107.
- [62] Hamid Basaeri et al. “Acoustic power transfer for biomedical implants using piezoelectric receivers: effects of misalignment and misorientation”. In: *Journal of Micromechanics and Microengineering* 29.8 (2019), p. 084004.
- [63] Shaul Ozeri et al. “Ultrasonic transcutaneous energy transfer using a continuous wave 650 kHz Gaussian shaded transmitter”. In: *Ultrasonics* 50.7 (2010), pp. 666–674.
- [64] Kyungmin Kim et al. “Acoustic Power Transfer using Self-focused Transducers for Miniaturized Implantable Neu-rostimulators”. In: *IEEE Access* (2021).
- [65] David B Christensen and Shad Roundy. “Non-dimensional analysis of depth, orientation, and alignment in acoustic power transfer systems”. In: *Smart Materials and Structures* 27.12 (2018), p. 125013.
- [66] Achraf Ben Amar, Ammar B Kouki, and Hung Cao. “Power approaches for implantable medical devices”. In: *sensors* 15.11 (2015), pp. 28889–28914.
- [67] Hung-Wei Chiu et al. “Pain control on demand based on pulsed radio-frequency stimulation of the dorsal root ganglion using a batteryless implantable CMOS SoC”. In: *IEEE transactions on biomedical circuits and systems* 4.6 (2010), pp. 350–359.
- [68] Andreas Haeblerlin et al. “Successful pacing using a batteryless sunlight-powered pacemaker”. In: *Europace* 16.10 (2014), pp. 1534–1539.

- [69] Robert F Padera Jr and Frederick J Schoen. “Other Cardiovascular Devices”. In: *Biomaterials Science*. Elsevier, 2013, pp. 784–798.
- [70] Tianjia Sun, Xiang Xie, and Zhihua Wang. *Wireless power transfer for medical microsystems*. Springer, 2013.
- [71] Mohammad Haerinia and Reem Shadid. “Wireless power transfer approaches for medical implants: A Review”. In: *Signals* 1.2 (2020), pp. 209–229.
- [72] Aurélie Laurent et al. “Echographic measurement of skin thickness in adults by high frequency ultrasound to assess the appropriate microneedle length for intradermal delivery of vaccines”. In: *Vaccine* 25.34 (2007), pp. 6423–6430.
- [73] Manfred Fiebig. “Revival of the magnetoelectric effect”. In: *Journal of physics D: applied physics* 38.8 (2005), R123.
- [74] Dhiren K Pradhan, Shalini Kumari, and Philip D Rack. “Magnetoelectric Composites: Applications, Coupling Mechanisms, and Future Directions”. In: *Nanomaterials* 10.10 (2020), p. 2072.
- [75] Marcelo J Dapino. “Magnetostrictive materials”. In: *Encyclopedia of Smart Materials* 2 (2002), pp. 600–620.
- [76] Evangelos Hristoforou and Aphrodite Ktena. “Magnetostriction and magnetostrictive materials for sensing applications”. In: *Journal of Magnetism and Magnetic Materials* 316.2 (2007), pp. 372–378.
- [77] Göran Engdahl and Isaak D Mayergoyz. *Handbook of giant magnetostrictive materials*. Vol. 107. Elsevier, 2000.
- [78] Abdul-Ghani Olabi and Artur Grunwald. “Design and application of magnetostrictive materials”. In: *Materials & Design* 29.2 (2008), pp. 469–483.
- [79] Mirza Bichurin and Vladimir Petrov. *Modeling of magnetoelectric effects in composites*. Vol. 201. Springer, 2014.
- [80] Yang Shi. “Modeling of nonlinear magnetoelectric coupling in layered magnetoelectric nanocomposites with surface effect”. In: *Composite Structures* 185 (2018), pp. 474–482.
- [81] Nicolas Galopin et al. “Finite element modeling of magnetoelectric sensors”. In: *IEEE transactions on Magnetics* 44.6 (2008), pp. 834–837.
- [82] MI Bichurin and VM Petrov. “Modeling of magnetoelectric interaction in magnetostrictive-piezoelectric composites”. In: *Advances in Condensed Matter Physics* 2012 (2012).
- [83] Thu Trang Nguyen et al. “Finite element modeling of magnetic field sensors based on nonlinear magnetoelectric effect”. In: *Journal of Applied Physics* 109.8 (2011), p. 084904.
- [84] Hakeim Talleb, Aurélie Gensbittel, and Zhuoxiang Ren. “Multiphysics modeling of multiferroic artificial materials by the finite element method”. In: *The European Physical Journal Applied Physics* 73.3 (2016), p. 30901.
- [85] Michael Emory Goforth. “The Development of a Novel Figure of Merit to Analyze Strain-Mediated Magnetoelectric Antennas”. PhD thesis. Virginia Tech, 2021.
- [86] James I Roscow et al. “Modified energy harvesting figures of merit for stress-and strain-driven piezoelectric systems”. In: *The European Physical Journal Special Topics* 228.7 (2019), pp. 1537–1554.
- [87] David Gibus et al. “Non-linear losses study in strongly coupled piezoelectric device for broadband energy harvesting”. In: *Mechanical Systems and Signal Processing* 165 (2022), p. 108370.

- [88] Leixiang Bian et al. “Magnetolectric transducer with high quality factor for wireless power receiving”. In: *Sensors and Actuators A: Physical* 150.2 (2009), pp. 207–211.
- [89] Lei Chen et al. “Magnetolectric transducer employing piezoelectric ceramic/ferromagnetic alloy/high-permeability FeCuNbSiB composite”. In: *IEEE transactions on magnetics* 47.10 (2011), pp. 4437–4440.
- [90] F Yang et al. “Resonant magnetolectric response of magnetostrictive/piezoelectric laminate composite in consideration of losses”. In: *Sensors and Actuators A: Physical* 141.1 (2008), pp. 129–135.
- [91] ShuXiang Dong and JunYi Zhai. “Equivalent circuit method for static and dynamic analysis of magneto-electric laminated composites”. In: *Chinese Science Bulletin* 53.14 (2008), pp. 2113–2123.
- [92] Mingsen Guo and Shuxiang Dong. “A resonance-bending mode magnetolectric-coupling equivalent circuit”. In: *IEEE transactions on ultrasonics, ferroelectrics, and frequency control* 56.11 (2009), pp. 2578–2586.
- [93] Hao-Miao Zhou et al. “Equivalent circuit method research of resonant magnetolectric characteristic in magnetolectric laminate composites using nonlinear magnetostrictive constitutive model”. In: *Smart materials and structures* 20.3 (2011), p. 035001.
- [94] Stephen Leadenham and Alper Erturk. “Unified nonlinear electroelastic dynamics of a bimorph piezoelectric cantilever for energy harvesting, sensing, and actuation”. In: *Nonlinear Dynamics* 79.3 (2015), pp. 1727–1743.
- [95] Kevin Malleron. “Modélisation multiphysique, caractérisation et conception de transducteurs magnétoélectriques pour l’alimentation de capteurs biomédicaux autonomes”. PhD thesis. Sorbonne université, 2018.
- [96] Kevin Malleron et al. “Experimental study of magnetolectric transducers for power supply of small biomedical devices”. In: *Microelectronics Journal* 88 (2019), pp. 184–189.
- [97] Kevin Malleron et al. “Finite-element modeling of magnetolectric energy transducers with interdigitated electrodes”. In: *IEEE Transactions on Magnetism* 53.6 (2017), pp. 1–4.
- [98] Ali Koteiche et al. “System-level parameter estimation of magnetolectric transducers for wireless power transfer”. In: *9th National Days on Energy Harvesting and Storage*. 2019.
- [99] DA Hall. “Review nonlinearity in piezoelectric ceramics”. In: *Journal of materials science* 36.19 (2001), pp. 4575–4601.
- [100] R D’hulst et al. “Energy scavengers: Modeling and behavior with different load circuits”. In: *IECON 2007-33rd Annual Conference of the IEEE Industrial Electronics Society*. IEEE. 2007, pp. 2169–2174.
- [101] Hakeim Talleb and Zhuoxiang Ren. “Finite-Element Modeling of a Magnetolectric Energy Transducer Including the Load Effect”. en. In: *IEEE Transactions on Magnetism* 51.3 (Mar. 2015), pp. 1–5. ISSN: 0018-9464, 1941-0069. DOI: 10.1109/TMAG.2014.2357492. URL: <http://ieeexplore.ieee.org/document/7093585/> (visited on 01/29/2020).
- [102] Alexis Brenes et al. “Maximum power point of piezoelectric energy harvesters: a review of optimality condition for electrical tuning”. en. In: *Smart Materials and Structures* (Dec. 2019). ISSN: 0964-1726, 1361-665X. DOI: 10.1088/1361-665X/ab6484. URL: <https://iopscience.iop.org/article/10.1088/1361-665X/ab6484> (visited on 01/29/2020).
- [103] Ali Koteiche et al. “Maximum power point of magnetolectric transducer for wireless power transmission”. In: *Smart Materials and Structures* 30.9 (2021), p. 095007.

- [104] Stephen Leadenham and Alper Erturk. “Unified nonlinear electroelastic dynamics of a bimorph piezoelectric cantilever for energy harvesting, sensing, and actuation”. en. In: *Nonlinear Dynamics* 79.3 (Feb. 2015), pp. 1727–1743. issn: 0924-090X, 1573-269X. doi: 10.1007/s11071-014-1770-x. url: <http://link.springer.com/10.1007/s11071-014-1770-x> (visited on 01/29/2020).
- [105] Elie Lefeuvre et al. “Power and frequency bandwidth improvement of piezoelectric energy harvesting devices using phase-shifted synchronous electric charge extraction interface circuit”. en. In: *Journal of Intelligent Material Systems and Structures* 28.20 (Dec. 2017), pp. 2988–2995. issn: 1045-389X, 1530-8138. doi: 10.1177/1045389X17704914. url: <http://journals.sagepub.com/doi/10.1177/1045389X17704914> (visited on 01/29/2020).
- [106] Ali Koteiche et al. “Power-limiting Phenomena in a Magnetolectric Transducer for Wireless Power Transfer”. In: *Wireless power transfer conference* (2020).
- [107] Haruhiko Asanuma and Toshihiko Komatsuzaki. “Nonlinear piezoelectricity and damping in partially-covered piezoelectric cantilever with self-sensing synchronized switch damping on inductor circuit”. en. In: *Mechanical Systems and Signal Processing* 144 (Oct. 2020), p. 106867. issn: 08883270. doi: 10.1016/j.ymsp.2020.106867. url: <https://linkinghub.elsevier.com/retrieve/pii/S0888327020302533> (visited on 11/24/2020).
- [108] Samuel C. Stanton et al. “Nonlinear piezoelectricity in electroelastic energy harvesters: Modeling and experimental identification”. en. In: *Journal of Applied Physics* 108.7 (Oct. 2010), p. 074903. issn: 0021-8979, 1089-7550. doi: 10.1063/1.3486519. url: <http://aip.scitation.org/doi/10.1063/1.3486519> (visited on 11/24/2020).
- [109] Angela Triplett and D. Dane Quinn. “The Effect of Non-linear Piezoelectric Coupling on Vibration-based Energy Harvesting”. en. In: *Journal of Intelligent Material Systems and Structures* 20.16 (Nov. 2009), pp. 1959–1967. issn: 1045-389X, 1530-8138. doi: 10.1177/1045389X09343218. url: <http://journals.sagepub.com/doi/10.1177/1045389X09343218> (visited on 11/24/2020).
- [110] Marco Amabili. “Nonlinear damping in nonlinear vibrations of rectangular plates: Derivation from viscoelasticity and experimental validation”. en. In: *Journal of the Mechanics and Physics of Solids* 118 (Sept. 2018), pp. 275–292. issn: 00225096. doi: 10.1016/j.jmps.2018.06.004. url: <https://linkinghub.elsevier.com/retrieve/pii/S0022509618303363> (visited on 11/24/2020).
- [111] Christian Lalanne. “Non-Viscous Damping”. In: *Sinusoidal Vibration* (2014), pp. 261–289.
- [112] Elie Lefeuvre et al. “Materials, structures and power interfaces for efficient piezoelectric energy harvesting”. en. In: *Journal of Electroceramics* 22.1-3 (Feb. 2009), pp. 171–179. issn: 1385-3449, 1573-8663. doi: 10.1007/s10832-007-9361-6. url: <http://link.springer.com/10.1007/s10832-007-9361-6> (visited on 12/01/2020).
- [113] M Renaud et al. “Optimum power and efficiency of piezoelectric vibration energy harvesters with sinusoidal and random vibrations”. en. In: *Journal of Micromechanics and Microengineering* 22.10 (Oct. 2012), p. 105030. issn: 0960-1317, 1361-6439. doi: 10.1088/0960-1317/22/10/105030. url: <https://iopscience.iop.org/article/10.1088/0960-1317/22/10/105030> (visited on 12/01/2020).
- [114] Tuan Anh Do et al. “3-D finite element analysis of magnetolectric composites accounting for material nonlinearity and Eddy currents”. In: *IEEE Transactions on Magnetics* 55.10 (2019), pp. 1–8.

- [115] F. Yang et al. “Resonant magnetoelectric response of magnetostrictive/piezoelectric laminate composite in consideration of losses”. en. In: *Sensors and Actuators A: Physical* 141.1 (Jan. 2008), pp. 129–135. issn: 09244247. doi: 10.1016/j.sna.2007.08.004. url: <https://linkinghub.elsevier.com/retrieve/pii/S0924424707005857> (visited on 12/01/2020).
- [116] Kapil Venkatachalam et al. “Accurate prediction of ferrite core loss with nonsinusoidal waveforms using only Steinmetz parameters”. In: *2002 IEEE Workshop on Computers in Power Electronics, 2002. Proceedings.* IEEE. 2002, pp. 36–41.
- [117] Kenji Uchino. “Piezoelectric energy harvesting systems—Essentials to successful developments”. In: *Energy Technology* 6.5 (2018), pp. 829–848.
- [118] Ashkan Haji Hosseinloo and Konstantin Turitsyn. “Fundamental limits to nonlinear energy harvesting”. In: *Physical Review Applied* 4.6 (2015), p. 064009.
- [119] Yipeng Wu et al. “Piezoelectric vibration energy harvesting by optimized synchronous electric charge extraction”. en. In: *Journal of Intelligent Material Systems and Structures* 24.12 (Aug. 2013), pp. 1445–1458. issn: 1045-389X, 1530-8138. doi: 10.1177/1045389X12470307. url: <http://journals.sagepub.com/doi/10.1177/1045389X12470307> (visited on 12/01/2020).
- [120] Alexis Brenes et al. “Unipolar synchronized electric charge extraction for piezoelectric energy harvesting”. In: *Smart Materials and Structures* 27.7 (2018), p. 075054.
- [121] Geoffrey K Ottman et al. “Adaptive piezoelectric energy harvesting circuit for wireless remote power supply”. In: *IEEE Transactions on power electronics* 17.5 (2002), pp. 669–676.
- [122] Geoffrey K Ottman, Heath F Hofmann, and George A Lesieutre. “Optimized piezoelectric energy harvesting circuit using step-down converter in discontinuous conduction mode”. In: *IEEE Transactions on power electronics* 18.2 (2003), pp. 696–703.
- [123] Elie Lefeuvre et al. “Buck-boost converter for sensorless power optimization of piezoelectric energy harvester”. In: *IEEE Transactions on Power Electronics* 22.5 (2007), pp. 2018–2025.
- [124] NA Kong et al. “Resistive impedance matching circuit for piezoelectric energy harvesting”. In: *Journal of Intelligent Material Systems and Structures* 21.13 (2010), pp. 1293–1302.
- [125] Alexis Brenes et al. “Tunable unipolar synchronized electric charge extraction strategy for piezoelectric energy harvesting”. In: *Journal of Intelligent Material Systems and Structures* 30.11 (2019), pp. 1629–1638.
- [126] YC Shu and IC Lien. “Analysis of power output for piezoelectric energy harvesting systems”. In: *Smart materials and structures* 15.6 (2006), p. 1499.